Editorial Board

Editor-in-Chief

Gang Zhang
A-Star, Institute of High Performance Computing (IHPC)
Singapore

Associate Editors

Nuo Yang
Huazhong University of Science and
Technology
China

Yasser Mahmoudi
University of Manchester
United Kingdom

Editorial Board Members

Maziar Dehghan
Materials and Energy Research Center
Iran

Sivasankaran Sivanandam
King Abdulaziz University
Saudi Arabia

Mohamed R. Eid
Northern Border University
Saudi Arabia

Talal Yusaf
Central Queensland University
Australia

Hitesh Panchal
Gujarat Technological University
India

Mousa Marzband
Northumbria University
United Kingdom

Clemente Bretti
Università di Messina
Italy

Olga E. Glukhova
Saratov State University
Russia

Fei Zhou
Nanjing University of Aeronautics and
Astronautics
China

Zhenyu Tian
University of Chinese Academy of Sciences
China

Muneer Ismael
University of Basrah
Iraq

Xiaohu Yang
Xi'an Jiaotong University
China

Ho Seon Ahn
Incheon National University
Korea

Mona Zebarjadi
University of Virginia
United States

Ioan Mihai Pop
Babeș-Bolyai University
Romania

Efstathios E. Michaelides
Texas Christian University
United States

Nehad Ali Shah
Sejong University
Korea

Jose Ordonez-Miranda
The University of Tokyo
Japan

Davood Domiri Ganji
University of Mazandaran
Iran

Mehmet Fatih Orhan
American University of Sharjah
United Arab Emirates

Olivier Mathieu
Texas A&M University
United States

Weiwei Yang
Xi'an Jiaotong University
China

Yuanzheng Li
Huazhong University of Science and
Technology
China

Jingchun Feng
Guangdong University of Technology
China

Zhengmao Li
Nanyang Technological University
Singapore

Chin-Hsiang Cheng
National Cheng Kung University
Taiwan

Erkan Oterkus
University of Strathclyde Glasgow
United Kingdom

Leilei Dai
University of Minnesota
United States

Shail Upadhyay
Banaras Hindu University
India

Xianglei Liu
Nanjing University of Aeronautics and
Astronautics
China

Grigorios Kyriakopoulos
National Technical University of Athens
Greece

Mohammed El Ganaoui
Université Henri Poincaré
France

Anqing Zheng
Chinese Academy of Sciences
China

Muhammad Hilmy Alfaruqi
Chonnam National University
Korea

Yuanyuan Duan
Tsinghua University
China

Silvio Simani
University of Ferrara
Italy

Abolfazl Ahmadi
Iran University of Science and Technology
Iran

Yuekuan Zhou
The Hong Kong University of Science and
Technology
Hong Kong

Harry D. Kambezidis
National Observatory of Athens
Greece

Alban Kuriqi
University of Lisbon
Portugal

Mario Luigi Ferrari
Università degli Studi di Genova
Italy

Jingzheng Ren
The Hong Kong Polytechnic University
Hong Kong

Linchuan Zhao
Shanghai Jiao Tong University
China

Devraj Singh
Amity School of Engineering & Technology
India

Mohsen Sheikholeslami
Babol Noshiravni University of Technology
Iran

Nima E. Gorji
Dublin City University
Ireland

Esmail Lakzian
Shahid Beheshti University
Iran

Qingsong Wang
University of Science and Technology of
China
China

Khaled Chetehouna
Institut National des Sciences Appliquées
(INSA) Centre Val de Loire
France

Hamdy Mahmoud Youssef
Umm Al-Qura University
Saudi Arabia

Emad Mohamed El-Said
Fayoum University
Egypt

Thermal Science and Engineering

Editors-in-Chief

Prof. Gang Zhang

A-Star, Institute of High Performance Computing (IHPC)

Singapore

Thermal Science and Engineering

Contents

Articles

![EnPress logo]

Article

Modeling of performance and thermodynamic study of a gas turbine power plant

Mohamed Elwardany[1,*], A. M. Nassib[1], Hany A. Mohamed[1,2], M. R. Abdelaal[2]

[1] Department of Mechanical Power Engineering, Faculty of Engineering, Assiut University, Asyut 71516, Egypt
[2] Manufacturing Department, Modern Academy for Engineering and Technology, Cairo 11571, Egypt
* Corresponding author: Mohamed Elwardany, M.Wardany@anu.edu.eg

Abstract: The efficiencies and performance of gas turbine cycles are highly dependent on parameters such as the turbine inlet temperature (TIT), compressor inlet temperature (T1), and pressure ratio (Rc). This study analyzed the effects of these parameters on the energy efficiency, exergy efficiency, and specific fuel consumption (SFC) of a simple gas turbine cycle. The analysis found that increasing the TIT leads to higher efficiencies and lower SFC, while increasing the To or Rc results in lower efficiencies and higher SFC. For a TIT of 1400 ℃, T1 of 20 ℃, and Rc of 8, the energy and exergy efficiencies were 32.75% and 30.9%, respectively, with an SFC of 187.9 g/kWh. However, for a TIT of 900 ℃, T1 of 30 ℃, and Rc of 30, the energy and exergy efficiencies dropped to 13.18% and 12.44%, respectively, while the SFC increased to 570.3 g/kWh. The results show that there are optimal combinations of TIT, To, and Rc that maximize performance for a given application. Designers must consider trade-offs between efficiency, emissions, cost, and other factors to optimize gas turbine cycles. Overall, this study provides data and insights to improve the design and operation of simple gas turbine cycles.

Keywords: gas turbine; thermal analysis; energy; exergy; efficiency

1. Introduction

Energy consumption is a key indicator of development, with population growth, urbanization, industrialization, and technological progress driving increased energy use. However, this rapid rise has contributed to pollution and the greenhouse effect. Currently, 80% of electricity is generated from fossil fuels, while renewable sources provide 20% [1–4]. Global electricity demand is growing by approximately 6% annually [5], and fossil fuels remain a major source of CO_2 emissions [6–12]. Natural gas (NG) accounts for 22% of global energy production, and demand for NG is expected to rise by 2.7% annually. By 2040, NG is projected to produce 28% of global electricity, up from 22% in 2012 [13–17]. The term "thermal power plant analysis" encompasses the efficient use of energy resources. Before 1940, efficiency was assessed using the first law of thermodynamics [18–23], while the second law, or exergy analysis, identifies where and why energy losses occur. This method is crucial for detecting inefficiencies and optimizing power plant performance [16,24–33].

Gas turbines are widely used in power generation due to their flexibility, efficiency, and ability to provide both baseload and peak-load power. Advances in materials and cooling technologies have significantly improved their thermal efficiency, making them a preferred choice for modern power plants. One of the primary challenges in gas turbine operation is managing the high temperatures within the combustion chamber, which directly affects the turbine's performance and

longevity. Research has focused on optimizing turbine blade materials, cooling techniques, and combustion processes to enhance both the energy and exergy efficiencies of gas turbines. Combined cycle power plants (CCPPs), which integrate gas and steam turbines, have become increasingly popular for their ability to achieve higher overall efficiencies by utilizing waste heat from the gas turbine to power the steam cycle [34–37]. The thermodynamic simple gas turbine cycle employs a gas turbine to transform gas energy into mechanical work. The compressor, combustion chamber, and turbine comprise the gas turbine. Before being burned in the combustion chamber, the compressor compresses air. The turbine blades move when hot combustion gases expand across them. The turbine releases exhaust gas. Gas turbines have combustor, compressor, and power turbine units. To power an open-cycle gas turbine, centrifugal or axial flow compressors compress ambient air. Air is compressed by the compressor. Fuel and pressurized air enter the combustion chamber. Gases power the turbine. The combination ignites to generate velocity gas. When turbine blades spin, the generator's rotor shaft revolves. Energy from turning the turbine shaft may power industrial machines and create electricity [6,38,49]. Ibrahim et al. [40] conducted an analysis of a simple gas turbine model using energy and exergy assessments. Their findings indicated that the combustion chamber was responsible for the highest exergy destruction. The air compressor demonstrated energy and exergy efficiencies of 92% and 94.9%, respectively, while the combustion chamber showed efficiencies of 61.8% and 67.5%. In comparison, the gas turbine achieved energy and exergy efficiencies of 82% and 92%. Overall, the system's energy and exergy efficiencies were reported as 34.3% and 32.4%, respectively.

The impacts of several operational parameters of gas turbine power plants were studied by Kurt et al. [41]. Results demonstrated that the overall power output reaches its maximum according to the TIT at P_R = 22, TIT = 1600 K, and CIT = 288.15 K. In contrast, it reaches its maximum according to the CIT at P_R = 18 and CIT = 273.15 K, and TIT = 1423.15 K. De Sa and Al Zubaidy [42] suggested an empirical relation between the capacity of the gas turbine to produce electricity when subjected to ambient air conditions that differ from ISO conditions. With data readings exceeding 8000 for gas turbine operation around 280 days, results showed that the gas turbine lost 1.47 MW of power output and 0.1% of thermal efficiency for every degree increase in ambient temperature over ISO conditions. Abou Al-Sood et al. [43] analyzed the performance of a gas turbine cycle featuring an irreversible intercooler, regenerative system, and reheat cycle. The results indicated that the minimum temperature ranged from 302 K to 315 K, while the maximum temperature was between 1320 K and 1360 K. The optimal pressure for the cycle was found to lie between 1449 kPa and 2830 kPa to optimize all performance parameters. Salah et al. [44] examined the influence of ambient temperature, compression ratio, and relative humidity on the thermal and exergy performance of a gas power plant over a full year under real weather conditions. Using ChemCad simulations, they identified system inefficiencies and losses, with the combustion chamber causing the most significant exergy destruction, followed by the compressor and gas turbine. Their findings showed that energy efficiency peaked at 37% in November, when the ambient temperature was 19.39 °C. Additionally, specific fuel consumption (SFC) increased with higher ambient temperatures, reaching its peak at 33.27 °C.

In this study, we will evaluate the performance of a gas turbine cycle using energy and exergy analysis. The objective is to examine the effects of design parameters on gas turbine performance, with simulations assessing how environmental conditions and other key factors impact the cycle. The research aims to identify optimal design parameters for gas turbine power plants, utilizing EES software to model cycle performance based on operational data from previous studies.

2. Modelling and analysis

In this study, a thermodynamic analysis of simple gas turbine (SGT) cycles is performed using conventional energy and exergy analysis to assess cycle performance. As shown in **Figure 1**, the SGT process involves compressing air in the compressor, mixing it with fuel, and igniting it in the combustion chamber. The resulting high-temperature exhaust gases expand through the turbine, producing mechanical work, after which they are released. This energy can be harnessed for electricity generation and powering industrial equipment.
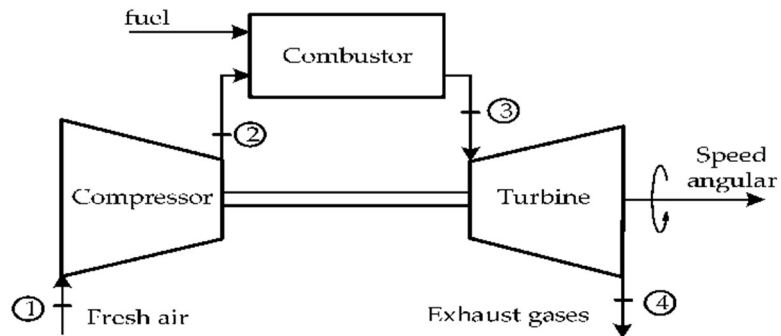
Figure 1. Simple gas turbine (SGT).

Table 1. Thermodynamic assumptions used for the (SGT) model based on [28,29].

Data	Value
Dead state conditions	$P_o = 1.01$ bar, $T_o = 293.15$ K
Turbine isentropic efficiency	87%
Compressor isentropic efficiency	85%
combustion efficiency	0.98 %
Ambient temperature	298 k
Compressor inlet pressure	94 kPa
Specific heat of air	1.005 kJ/kg K
Specific heat of gasses	1.14 kJ/kg K
Ratio of specific heat for gasses	1.33
Ratio of specific heat for air	1.4
Fuel type	NG

Energy analysis, based on the first law of thermodynamics, and exergy analysis, grounded in the second law, are employed to evaluate the cycle's efficiency. The analysis includes several assumptions, summarized in **Table 1**.

2.1. Energy analysis

The energy assessment of a gas turbine cycle is based on the Brayton cycle, involving calculations of the system's energy input and output. The key components include the air compressor, combustion chamber, and gas turbine. The following equations are used to analyze each part of the cycle [45]. Compressor:

$$T_2 = T_1\left(1 + \frac{1}{\eta_{AC}}\left(r_{AC}^{\frac{k-1}{k}} - 1\right)\right) \tag{1}$$

$$\dot{W}_{\text{AC}} = \dot{m}_a c_{\text{pa}}(T_2 - T_1) \tag{2}$$

$$c_{\text{pa}}(T) = 1.048 - \left(\frac{1.83T}{10^4}\right) + \left(\frac{9.45T^2}{10^7}\right) - \left(\frac{5.49T^3}{10^{10}}\right) + \left(\frac{7.92T^4}{10^{14}}\right) \tag{3}$$

In Equation (1), T_1 and T_2 denote the air temperatures at the compressor inlet and outlet, respectively, while k is the specific heat ratio and r is the compression ratio. The compressor's power consumption is determined using Equation (2), and Equation (3) defines the specific heat of air as a function of temperature.

Combustion chamber:

$$\dot{m}_a h_2 + \dot{m}_f \text{LHV} = \dot{m}_g h_3 + (1 - \eta_{\text{cC}})\dot{m}_f \text{LHV} \tag{4}$$

$$\dot{m}_g = \dot{m}_f + \dot{m}_a \tag{5}$$

$$f = \frac{\dot{m}_f}{\dot{m}_a} = \frac{C_{pg} \times T_3 - C_{pa}T_2}{\text{LHV} - C_{pg} \times T_3} \tag{6}$$

The lower heating value (LHV) varies depending on the fuel's properties. In this analysis, natural gas is utilized in the combustion chamber.

Gas turbine:

$$T_4 = T_3\left(1 - \eta_{\text{GT}}\left(1 - \left(\frac{P_3}{P_4}\right)^{\frac{k-1}{k}}\right)\right) \tag{7}$$

$$\dot{W}_{GT} = \dot{m}_g c_{p,g}\left(T_{A_3} - T_{A_4}\right) \tag{8}$$

$$C_{pg}(T) = 0.991 + \left(\frac{6.997T}{10^5}\right) + \left(\frac{2.712T^2}{10^7}\right) - \left(\frac{1.2244T^3}{10^{10}}\right) \tag{9}$$

In Equation (7), T_3 and T_4 denote the turbine's inlet and outlet combustion gas temperatures, respectively. The turbine's power output is determined using Equation (8), while Equation (3) calculates the air's specific heat as a function of temperature.

2.2. Exergy analysis

Exergy represents the maximum useful work a system can perform as it moves toward equilibrium with its environment. Based on the second law of thermodynamics and applying mass and energy balances, exergy analysis provides a powerful method for assessing energy system performance. Exergy consists of four parts: chemical, physical, kinetic, and potential. However, in typical analyses, only chemical and physical exergies are considered, while kinetic and potential components are often neglected. Physical exergy refers to a system's ability to perform work, while chemical exergy is tied to differences in chemical composition from equilibrium conditions [46]. The general equations for exergy analysis are presented below.

$$\dot{E}_{x,\text{heat}} + \sum_i \dot{m}_i e_{x,i} = \sum_e \dot{m}_e e_{x,e} + \dot{E}_{x,w} + \dot{I}_{\text{dest}} \tag{10}$$

$$\dot{E}_{x,W} = \dot{W} \tag{11}$$

$$\dot{E}_{x,\text{heat}} = \left(1 - \frac{T_o}{T_i}\right)\dot{Q}_i \tag{12}$$

$$\dot{E}_x = \dot{E}_{x,\text{phy}} + \dot{E}_{x,\text{che}} \tag{13}$$

By applying Equation (10), the exergy flow rate for each system component can be calculated. Equation (11) represents the system's work derived from the exergy flow. The exergy generation rate due to heat is expressed in Equation (12). Finally, Equation (13) outlines the physical and chemical exergies of the component [47].

Physical exergy:

The physical exergy arises from the system's deviation in pressure and temperature relative to its dead state [40]. The following equations can be used to compute the physical exergy of the system.

$$e_x = e_{x,\text{phy}} + e_{x,\text{che}} \tag{14}$$

$$e_{x,phy} = e_x^T + e_x^P \tag{15}$$

$$e_x^T = c_p\left((T - T_o) - T_o \ln \frac{T}{T_o}\right) \tag{16}$$

$$e_x^p = RT_o \ln \frac{P}{P_o} \tag{17}$$

The physical exergy can be calculated using Equation (15), with Equations (16) and (17) defining it in terms of temperature and pressure. In these equations, P_o and T_o represent the ambient pressure and temperature, while C_p and R denote the specific heat at constant pressure and the gas constant, respectively [47].

Chemical exergy:

Chemical exergy arises when the chemical composition of a system differs from the surrounding dead-state conditions [40]. The exergy flow of the fuel can be calculated using the following equation.

$$\xi = \frac{e_{x,\text{fuel}}}{\text{LHV}_{\text{fuel}}} \tag{19}$$

In Equation (19), ξ represents the ratio of exergy flow to the LHV of the fuel. ($LHV_{\text{fuel}} = 48,806$ KJ/kg) Usually, the value for ξ is 1.06 for NG. The following equation can be used to determine the exergy of the combustion products [40].

$$e_{x,cg} = \frac{\left[\sum_{i=1}^n x_i e_{x,\text{che},i} + RT_0 \sum_{x=i}^n x_i \ln(x_i)\right]}{\sum(x_i)} \tag{20}$$

In Equation (20), the subscript iii refers to the type of air fraction, x is the molar fraction, and $e_{x,ch}$ represents the standard chemical exergy of each component. **Table 2** provides the standard chemical exergy and molar fraction of each gas. More accurate results can be obtained using the following equations [48].

$$\lambda = \frac{0.058\dot{m}_{\text{air}}}{\dot{m}_{\text{fuel}}} \tag{21}$$

$$x_{N_2} = \frac{(7.524)\lambda}{1 + (9.6254)\lambda} \tag{22}$$

$$x_{O_2} = \frac{2(\lambda - 1)}{1 + (9.6254)\lambda} \tag{23}$$

$$x_{CO_2} = \frac{1 + (0.0028)\lambda}{1 + (9.6254)\lambda} \tag{24}$$

$$x_{H_2O} = \frac{2 + (0.0972)}{1 + (9.6254)\lambda} \tag{25}$$

Equations (21)–(25) can be used to calculate the molar fraction of each component in the combustion products, applicable specifically when natural gas (NG) is used as the fuel. In these equations, the subscript "k" denotes the fuel-air ratio [48].

Table 2. Standard exergy and molar fraction [32].

Element	$e_{x,che}$ (KJ/mol)	Molar fraction (%)
N_2	0.72	75.67
O_2	3.97	20.34
CO_2	19.87	0.03
H_2O	9.49	3.03

Exergy efficiency is a crucial metric for evaluating how well a system utilizes energy. It is defined as the ratio of useful work output to the total energy input. A higher exergy efficiency indicates reduced energy wastage and enhanced productivity. This measure is essential for assessing both the long-term sustainability and economic feasibility of energy systems. To understand exergy destruction, the exergy flow rate for each component is calculated, revealing a decrease in exergy after each process.

Exergy destruction:

Exergy destruction is assessed by calculating the exergy flow rate for each component, which shows a decrease in exergy after each process. Typically, this destruction is quantified using Equation (27) [48].

$$\dot{E}_{x,\text{in}} - \dot{E}_{x,\text{out}} = \dot{E}x_D \tag{26}$$

Air compressor:

$$\dot{E}x_{D,AC} = \dot{E}x_1 - \dot{E}x_2 + \dot{W}_{AC} \tag{27}$$

Combustion chamber:

$$\dot{E}x_{D,CC} = \dot{E}x_2 + \dot{E}x_5 - \dot{E}x_3 \dot{E}x_{D,AC} = \dot{E}x_1 - \dot{E}x_2 + \dot{W}_{AC} \tag{28}$$

Gas turbine:

$$\dot{E}x_{D,GT} = \dot{E}x_3 - \dot{E}x_4 - \dot{W}_{GT} \tag{29}$$

Systems efficiency:

Each component is evaluated for both energy and exergy to determine which has the highest and lowest efficiency. Exergy efficiency is calculated using the following equation [48].

Air compressor:

$$\eta_{x,AC} = \frac{\dot{E}x_2 - \dot{E}x_1}{\dot{W}_{AC}} \tag{30}$$

Combustion chamber:

$$\eta_{x,CC} = \frac{\dot{E}x_3}{\dot{E}x_3 - \dot{E}x_1} \tag{31}$$

Gas turbine:

$$\eta_{x,GT} = \frac{\dot{W}_{GT}}{\dot{E}x_3 - \dot{E}x_4} \tag{32}$$

Equation (30) is used to calculate the efficiency of the air compressor, considering work output and exergy destruction. Similarly, Equation (32) assesses the efficiency of the gas turbine by considering its exergy destruction and work output. For the combustion chamber, Equation (31) evaluates efficiency based on the exergy rate and exergy destruction of the fuel [48]. The overall exergy and energy efficiencies of the simple gas turbine cycle can be determined using the equations provided below [47].

$$\dot{W}_{Net} = \dot{W}_{GT} - \dot{W}_{AC} \tag{33}$$

$$\text{SFC} = 3600 \frac{\dot{m}_{\text{fuel}}}{\dot{W}_{\text{net}}} \tag{34}$$

$$\eta_{\text{I}} = \frac{\dot{W}_{\text{net}}}{\dot{m}_{\text{fuel}}\text{LHV}} \tag{35}$$

$$\eta_{\text{II}} = \frac{\dot{W}_{\text{net}}}{\dot{E}_{x,f}} \tag{36}$$

Equation (34) calculates the specific fuel consumption of the gas turbine. Equation (36) provides the overall exergy efficiency, with $\dot{E}_{x,f}$ representing the fuel exergy flow rate. Equation (35) is used to determine the overall energy efficiency of the cycle [47].

2.3. Model validation

Based on the analysis, a simulation program was created using EES software for the SGT. The results were validated against those from [40]. **Table 3** presents the operating parameters used for validation, while **Figure 2** illustrates the comparison between the reference and current models, which shows strong agreement.
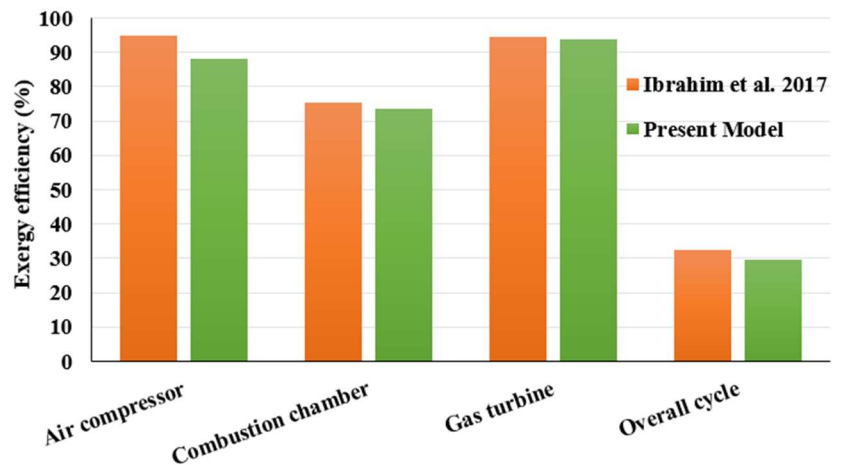
Figure 2. Comparison between the exergy efficiency for all components of simple gas cycle in the present model with [40].

Table 3. Operating parameters for validation model based on [40].

| Parameters	Value
Ambient air temperature	18.34 °C
Inlet pressure	94 kPa
Air mass flow rate	439.802 kg/s
Fuel mass flow rate	10.473 kg/s
Compression ratio	15.64
Fuel type	NG

3. Results and discussion

This section details the simulation results regarding how operating conditions influence the performance of gas turbine cycles. Using a computer model developed in EES software, we analyzed the effects of various operating parameters on specific fuel consumption (SFC), energy, and exergy efficiencies. The cycle's performance was evaluated across different operational scenarios. The findings are based on previously discussed theoretical relationships. The simulation results for the SGT cycle are presented and examined in this section.

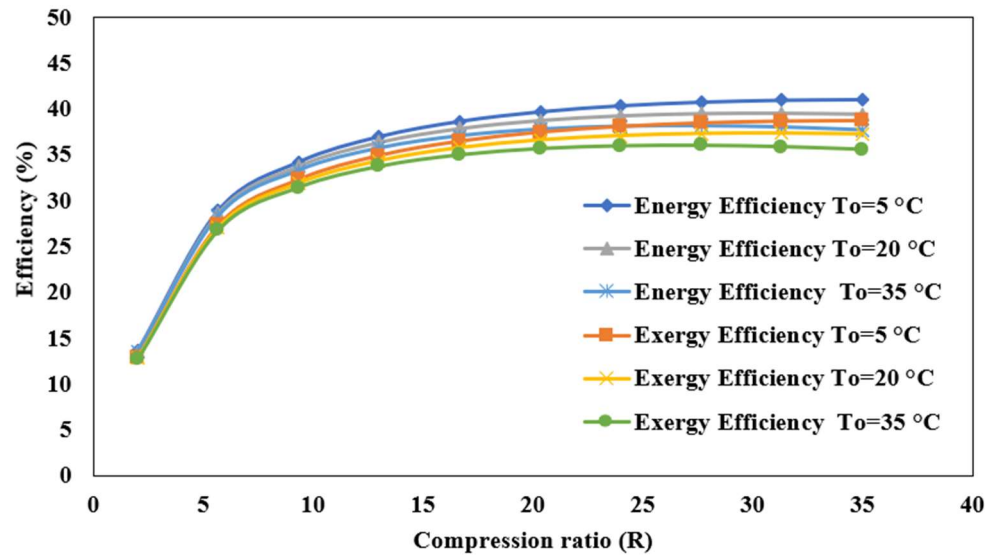### 3.1. Effect of compression ratio and turbine inlet temperature on energy and exergy efficiencies

Figure 3 provides performance data for a gas turbine under three different turbine inlet temperature (TIT) conditions (900 [c], 1200 [c], and 1400 [c]) at a constant ambient temperature of 25 [c]. The data in this table shows that increasing the TIT leads to higher gas turbine efficiencies, both in terms of energy and exergy efficiency. This suggests that higher pressure ratios can lead to more efficient energy conversion, even when the TIT is held constant. The data also shows that, for a given TIT, the exergy efficiency is lower than the energy efficiency. However, the difference between energy and exergy efficiencies decreases as the pressure ratio increases. However, it is worth noting that the rate of increase in efficiency with respect to pressure ratio is not constant across different TIT conditions, this indicates that the optimal pressure ratio for a given TIT may depend on the specific design and operating conditions of the gas turbine. Overall, this table provides additional insights into the performance of a gas turbine under different TIT and pressure ratio conditions, taking into account both idealized maximum efficiency and real-world losses and inefficiencies. However, additional factors such as the specific design and operating conditions of the gas turbine, as well as environmental and economic considerations, would need to be taken into account for a more thorough analysis.
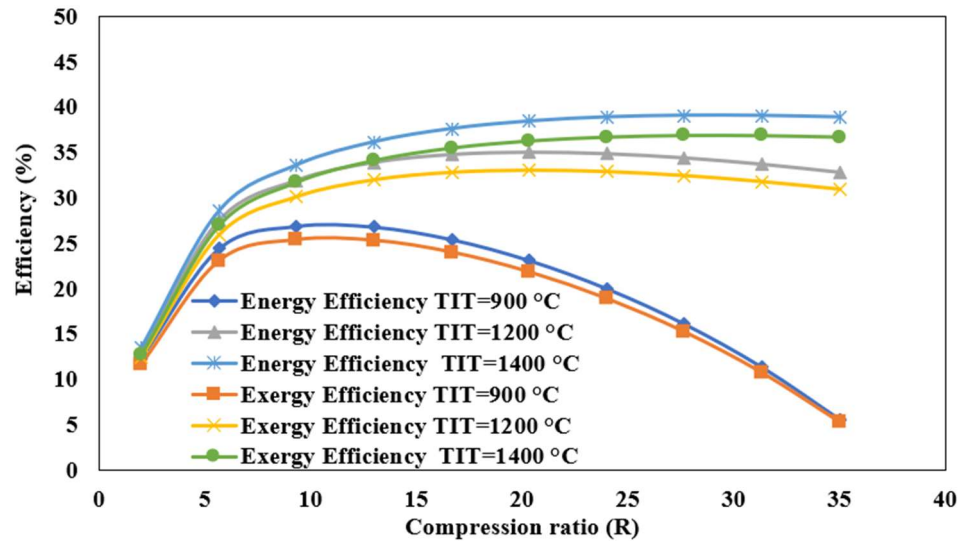
Figure 3. Illustrates how energy and exergy efficiencies vary with compression ratio and turbine inlet temperature.

3.2. Impact of ambient temperature and compression ratio on energy and exergy efficiency
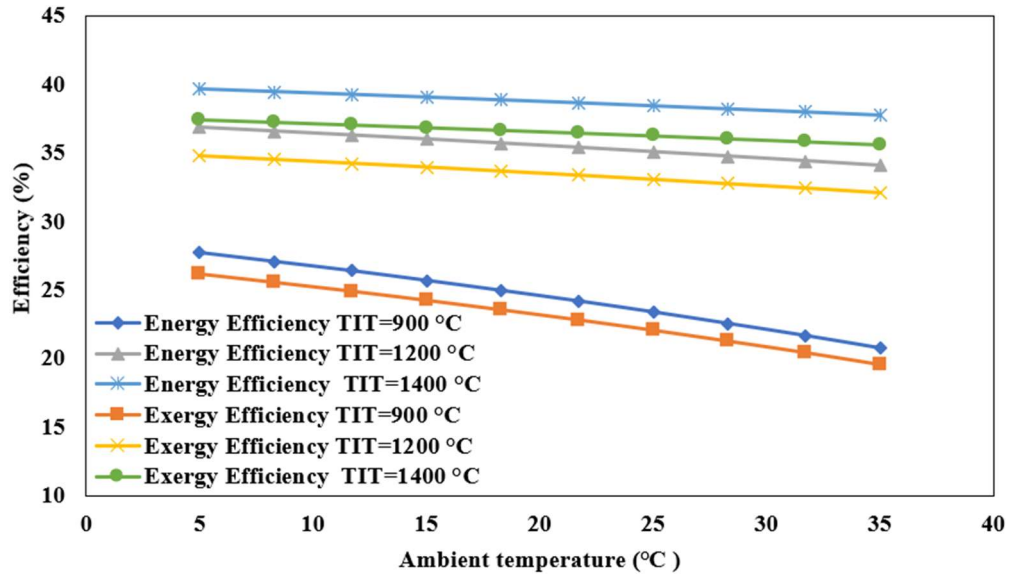
Figure 4 shows the energy and exergy efficiencies of a gas turbine at different operating conditions. The data is presented in three sets, each with a constant value for the turbine inlet temperature (TIT) of 1400 °C and different values for the ambient air temperature (*T*o) of 5 °C, 20 °C, and 35 °C. For example, at a TIT of 1400 °C and a *T*o of 5 °C, the energy efficiency of the gas turbine is 13.65% at a compression ratio of 2, and the exergy efficiency is 12.88%. As the compression ratio increases, both the energy and exergy efficiencies of the gas turbine also increase. In general, a higher compression ratio can increase the energy and exergy efficiencies of a gas turbine. However, increasing the compression ratio can also increase the risk of engine knock and other undesirable effects, so there is often a trade-off between efficiency and other factors such as engine durability and emissions. By analyzing the data in the figure, it may be possible to identify the optimal operating conditions for the gas turbine to achieve the highest energy or exergy efficiency. For example, it may be possible to identify the compression ratio and ambiant temperature that would result in the highest efficiency. Additionally, analyzing the data may also reveal areas where the design of the gas turbine could be improved to increase efficiency, such as by optimizing the combustion process or improving the design of the compressor and turbine components.

Figure 4. Illustrates how energy and exergy efficiencies vary with compression ratio and turbine ambient temperature.

3.3. Impact of turbine inlet temperature and ambient temperature on energy and exergy efficiencies

In gas turbine cycles, the turbine inlet temperature (TIT) and compressor inlet temperature ($T1$) are two of the most important parameters that influence the performance of the system. **Figure 5** shows the energy and exergy efficiencies for gas turbine cycles operating at different compressor inlet temperatures ($T1$) and a fixed pressure ratio ($R = 20$) for three different turbine inlet temperatures (TIT): 900 ℃, 1200 ℃, and 1400 ℃. Based on the data in the figure, it can be observed that increasing the TIT generally results in higher energy and exergy efficiencies for a fixed compressor inlet temperature and pressure ratio. For example, comparing the values for $T1 = 5$ ℃ and $R = 20$, the energy efficiency increases from 27.71% to 36.83% to 39.62%, as the TIT increases from 900 ℃ to 1200 ℃ to 1400 ℃, respectively. It can also be seen that, at a fixed TIT, there is an optimum value for $T1$ that maximizes the energy and exergy efficiencies. This optimal value of $T1$ decreases as the TIT increases. For example, for TIT = 900 ℃ and $R = 20$, the maximum energy efficiency is achieved at $T1 = 15$ ℃, while for TIT = 1400 ℃ and $R = 20$, the maximum energy efficiency is achieved at $T1 = 11.7$ ℃. Higher TITs generally lead to higher efficiencies, but there are practical limitations to how high the TIT can be due to material and technology constraints. Similarly, lower To values can improve efficiency, but only up to a certain point, as lower temperatures can reduce the power output of the gas turbine. Overall, higher TITs generally lead to higher efficiencies, but there are practical limitations to how high the TIT can be due to material and technology constraints. Similarly, lower To values can improve efficiency, but only up to a certain point, as lower temperatures can reduce the power output of the gas turbine. The data in the figure can be used to optimize the design and operation of gas turbine cycles by selecting the values of TIT and T [1] that maximize the energy and exergy efficiencies. The optimal values depend on the specific application and operating conditions.

Figure 5. Illustrates how energy and exergy efficiencies vary with turbine ambient temperature and ambient temperature.

3.4. Impact of turbine inlet temperature and compression ratio on specific fuel consumption

The specific fuel consumption (SFC) is a key parameter for assessing the fuel efficiency of gas turbine cycles. It represents the amount of fuel consumed per unit of power output. The lower the SFC, the more efficient the gas turbine cycle is at converting fuel into usable power. The SFC is influenced by several factors, including the compressor and turbine efficiencies, the combustion process, the pressure ratio, and the turbine inlet temperature (TIT). Generally, higher pressure ratios and TITs result in lower SFC values, while lower SFC values can be achieved by improving the efficiency of the compressor and turbine or by optimizing the combustion process. In **Figure 6,** the SFC values are shown for gas turbine cycles operating at different pressure ratios and TITs with a fixed compressor inlet temperature of 25 °C. The data shows that increasing the TIT generally results in lower SFC values, as more of the energy in the fuel is converted into useful work. Similarly, increasing the pressure ratio can also improve fuel efficiency, as the higher pressure ratio leads to a higher turbine work output for the same amount of fuel input. For example, comparing the values for PR = 2, the SFC decreases from 520 g/kWh to 247.7 g/kWh to 214 g/kWh, as the TIT increases from 900 °C to 1200 °C to 1400 °C, respectively. It can also be seen that, at a fixed TIT, there is an optimal value for the pressure ratio that minimizes the SFC. This optimal value of PR generally increases as the TIT increases. For example, for TIT = 900 °C, the minimum SFC is achieved at PR = 16.67, while for TIT = 1400 °C, the minimum SFC is achieved at PR = 35. However, it's important to note that increasing the TIT and pressure ratio can also lead to higher operating temperatures and pressures, which can increase the risk of component failure and reduce the overall reliability of the system. Therefore, a trade-off must be made between fuel efficiency and reliability when designing and operating gas turbine cycles. In addition to the SFC, other factors such as emissions, cost, and performance requirements must also be taken into account when designing and operating gas

turbine cycles. For example, reducing emissions may require additional components or processes that can increase the cost and complexity of the system. Therefore, the design and operation of gas turbine cycles must consider a variety of factors to achieve the best overall performance and efficiency.
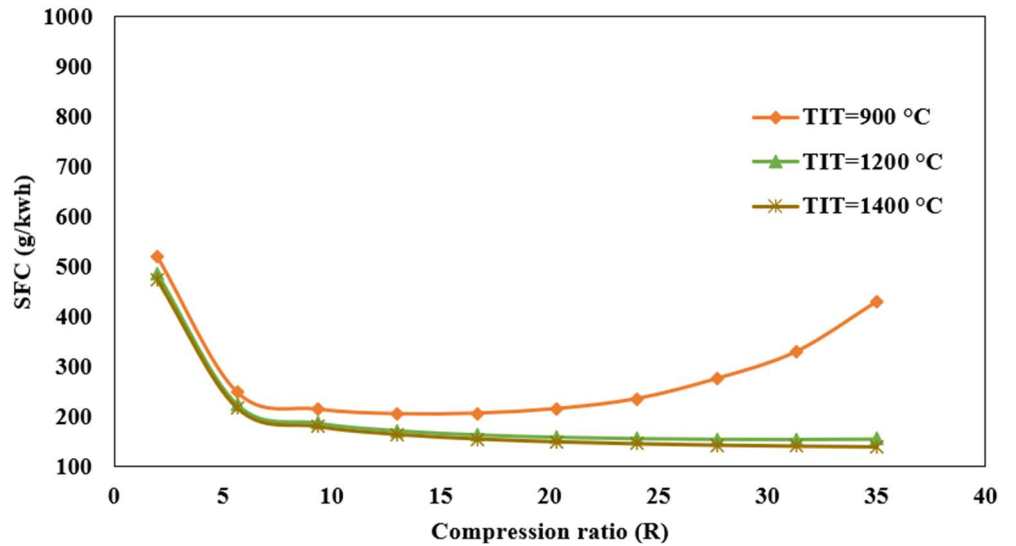
Figure 6. Specific fuel consumption variation with compression ratio and turbine inlet temperature.

3.5. Impact of compression ratio and ambient temperature on specific fuel consumption

In **Figure 7**, the SFC values are shown for gas turbine cycles operating at different pressure ratios and turbine inlet temperatures (TIT), with varying compressor inlet temperatures (T_o). The data shows that decreasing the compressor inlet temperature generally results in lower SFC values, as cooler air is denser and contains more oxygen, which can improve combustion efficiency. For example, comparing the values for TIT = 1400 °C and PR = 2, the SFC decreases from 474.2 g/kWh to 472.9 g/kWh to 471.8 g/kWh, as the T_o decrease from 35 °C to 20 °C to 5 °C, respectively. Similarly, increasing the pressure ratio can also improve fuel efficiency, as it leads to a higher turbine work output for the same amount of fuel input. For example, comparing the values for TIT = 1400 °C and T_o = 5 °C, the SFC decreases from 471.8 g/kWh to 135.4 g/kWh as the pressure ratio increases from 2 to 35. The data in the table also shows that there is an optimal pressure ratio that minimizes the SFC for a given TIT and To. This optimal value of pressure ratio generally increases as the TIT and T_o decrease. For example, for TIT = 1400 °C and T_o = 5 °C, the minimum SFC is achieved at PR = 35, while for TIT = 1400 °C and T_o = 35 °C, the minimum SFC is achieved at PR = 2. Overall, the data in the table can be used to optimize the design and operation of gas turbine cycles by selecting the appropriate TIT, T_o, and pressure ratio to achieve the desired fuel efficiency.
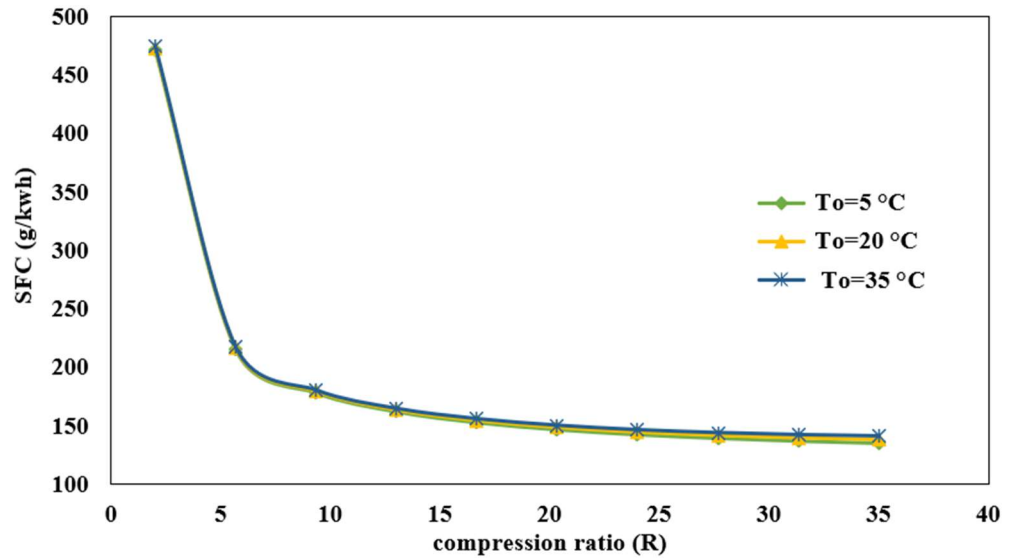
Figure 7. Specific fuel consumption variation with compression ratio and ambient temperature.

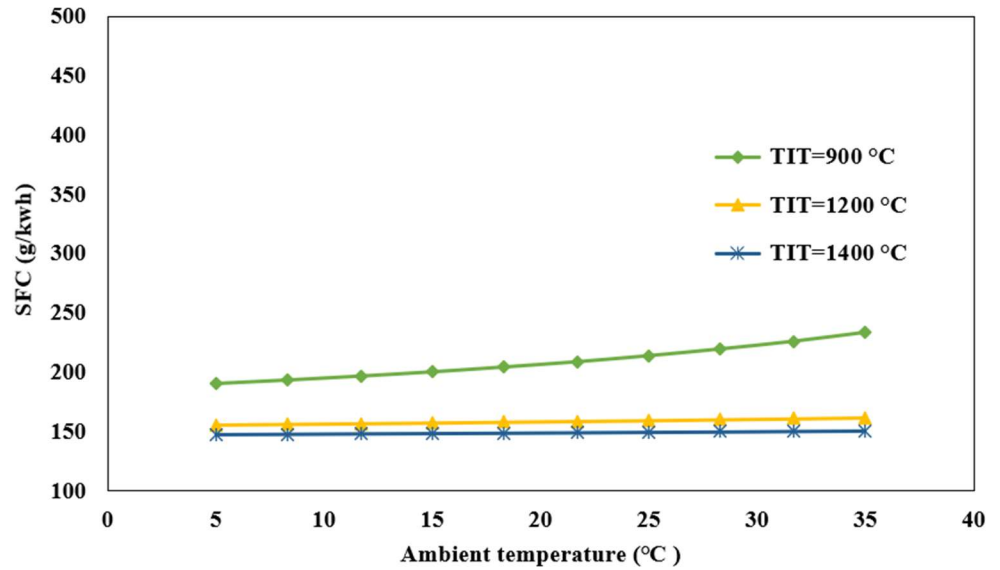## 3.6. Impact of turbine inlet temperature and ambient temperature on specific fuel consumption

In **Figure 8**, the SFC values are shown for gas turbine cycles operating at different turbine inlet temperatures (TIT), with a fixed pressure ratio (R) of 20 and varying compressor inlet temperatures (T1). The data shows that decreasing the compressor inlet temperature generally results in lower SFC values, as cooler air is denser and contains more oxygen, which can improve combustion efficiency. Similarly, increasing the turbine inlet temperature generally results in higher SFC values, as more fuel is required to maintain the higher combustion temperatures. For example, comparing the values for $T1$ = 5 °C, the SFC increases from 190.7 g/kWh to 233.2 g/kWh, as the TIT increases from 900 °C to 1400 °C, respectively. Overall, the design and operation of gas turbine cycles must consider a variety of factors to achieve the best overall performance and efficiency. This can involve trade-offs between different factors, such as fuel efficiency, emissions, reliability, and cost, to find the optimal balance for a given application.

Table 4 provides data on the overall efficiency, exergy efficiency, and specific fuel consumption (SFC) for different combinations of turbine inlet temperature (TIT), compressor inlet temperature (To), and pressure ratio (Rc) for a simple gas turbine cycle. The TIT values considered are 900 °C, 1200 °C, and 1400 °C, while the To values are 5 °C, 25 °C, and 35 °C, and the Rc values are 8, 20, and 30. For each combination, the table reports the energy efficiency, exergy efficiency, and SFC of the simple gas turbine cycle. Based on the data in the table, it can be observed that increasing the TIT generally leads to higher efficiency and lower SFC. Also, increasing the To or Rc generally results in lower efficiency and higher SFC. For example, for TIT = 1400 °C, To = 20 °C, and Rc = 8, the energy efficiency is 32.75%, the exergy efficiency is 30.9%, and the SFC is 187.9 g/kWh. However, for TIT = 900 °C, To = 30 °C, and Rc = 30, the energy efficiency is only 13.18%, the exergy efficiency is 12.44%, and the SFC is 570.3 g/kWh. By analyzing the data in **Table 4**, it is possible to determine the optimal values of TIT, To, and Rc for a given gas turbine

application. For example, a designer might choose a higher TIT to increase efficiency, but there may be practical limitations on the materials and technology available to achieve a high enough TIT. Similarly, a designer might choose a lower T_o to improve efficiency, but this could also reduce the power output of the gas turbine. In summary, **Table 4** provides important data for understanding the performance of simple gas turbine cycles and can be used to optimize the design of gas turbine systems for various applications.

Table 4. Overall efficiency and SFC for different values of TIT, T_o, and R_c associated with the simple gas turbine cycles.

TIT (℃)	T_o (℃)	R_c	Energy efficiency (%)	Exergy efficiency (%)	SFC (g/kwh)
		8	27.77	26.2	215.5
	5	20	27.71	26.14	190.7
		30	21.82	20.58	215.6
		8	26.44	24.94	221.7
900	25	20	23.38	22.06	213.8
		30	13.18	12.44	324.7
		8	25.69	24.24	225.6
	35	20	20.75	19.57	233.2
		30	7.426	7.006	570.3
		8	31.47	29.69	194.4
	5	20	36.83	34.74	155.3
		30	36.82	34.74	148
		8	30.75	29.01	196.4
1200	25	20	35.04	33.06	159.2
		30	34	32.08	154.5
		8	30.37	28.65	197.6
	35	20	34.04	32.11	161.7
		30	32.36	30.52	159
		8	32.75	30.9	187.9
	5	20	39.62	37.38	147.4
		30	40.9	38.59	138
		8	32.22	30.39	189.1
1400	25	20	38.4	36.23	149.5
		30	39.1	36.88	141
		8	31.93	30.12	189.8
	35	20	37.73	35.59	150.7
		30	38.08	35.92	142.8

Figure 8. Illustrates how specific fuel consumption vary with ambient temperature and turbine inlet temperature.

4. Conclusion

In conclusion, the research demonstrates that turbine inlet temperature and compression ratio are important factors influencing the energy efficiency, exergy efficiency, and fuel consumption of gas turbine cycles. Higher turbine inlet temperatures and compression ratios lead to higher energy and exergy efficiencies but also higher fuel consumption. The ambient temperature also affects the performance, with cooler ambient temperatures improving efficiency up to a certain point. However, real-world gas turbine designs and operations must consider a range of factors and trade-offs. Higher turbine inlet temperatures and compression ratios enable gas turbines to operate closer to ideal Carnot cycle efficiencies. However, material constraints limit how high the inlet temperatures and pressures can go with current technology. Ambient temperatures affect the gas turbine cycle performance due to their impact on the density and mass flow rate of the inlet air. Cooler air is denser and contains more oxygen, enabling improved combustion and higher power output. However, ambient temperatures also limit how low the inlet temperatures can feasibly go.

Exergy efficiency represents the practical conversion efficiency that accounts for irreversibilities and losses in real systems. The exergy efficiencies were consistently lower than the energy efficiencies, indicating significant losses in the gas turbine cycles. In practice, gas turbine designers must consider trade-offs between efficiency gains, material constraints, durability, environmental factors, and lifecycle costs. Achieving the highest theoretical efficiencies may not translate to the optimal real-world design for a given application. There are opportunities to improve gas turbine efficiencies through innovations, including new materials, combustion enhancements, and advanced engine architectures. Higher efficiency usually comes at the cost of greater complexity, higher capital costs, material constraints, and reduced durability. Gas turbine cycles must therefore optimize a variety of parameters to achieve the best balance of efficiency, emissions, cost, and performance for the specific application.

While improving one factor may seem promising from an analysis of theoretical performance data, other practical limitations and considerations often come into play in real-world gas turbine systems.

Recommendations for future work

- A sensitivity analysis evaluates how the results may change under different conditions or assumptions. For example, determine how sensitive the efficiencies are to small changes in TIT around the optimal value. See how the results vary for different types of fuels or for part-load operation. A robust analysis considers a range of possible scenarios.
- Discuss techno-economic implications, including how the capital and operating costs of gas turbines are influenced by parameters like TIT, T_o, and R_c. Improving performance through higher temperatures and pressure ratios, for example, also tends to increase costs. The costs associated with emissions control systems can also be significant. Discuss the costs and benefits of different optimization strategies.
- Consider alternative optimization objectives, such as minimizing emissions (e.g., NOx) rather than maximizing efficiency. Determine how parameters like TIT, T_o, and R_c would differ to optimize for minimal NOx emissions and evaluate the trade-offs with efficiency. Multi-objective optimization is important for sustainability.
- Discuss opportunities for future research on next-generation gas turbines, including technologies like intercooling, recuperators, and direct firing. Speculate on new approaches that could significantly improve gas turbine performance beyond incremental changes to TIT, T_o, and R_c alone. This helps to paint a picture of the future for continued progress.

Nomenclature

Symbols		Subscripts		Abbreviation	
Cp	Specific heat (KJ/kg)	a	Air	AF	Air to fuel ratio
h	Specific enthalpy (J/kg)	c	Compressor	CIT	Compressor inlet temperature
m	Mass flow rate (kg/s)	cc	Combustion chamber	LHV	Fuel heating value (kJ/kg)
P	Pressure (kPa)	GT	Gas turbine	NG	Natural gas
q	Heat supplied (W)	net	Net	SGT	Simple gas turbine
Rc	Pressure ratio	o	Outlet	SFC	Specific fuel consumption (g/kwh)
s	Specific entropy (J/kg K)	p	Pump	TIT	Turbine inlet temperature (k)

T	Temperature (K)	**Greek symbols**	
W	Work (W)	η	Thermal efficiency
		γ	Ratio of specific heat

References

1. Liu X, Zeng Z, Hu G, Asgari A. Thermodynamic, environmental, and economic analysis of a novel power and water production system driven by gas turbine cycle. Alexandria Engineering Journal. 2022; 61: 9529–9551. doi: 10.1016/j.aej.2022.03.038

2. Sinha AA, Sanjay, Ansari MZ, et al. Thermodynamic assessment of biomass-fueled solid oxide fuel cell integrated gas turbine hybrid configuration. Sustainable Energy Technologies and Assessments. 2023; 57: 103242. doi: 10.1016/j.seta.2023.103242

3. Shabruhi Mishamandani A, Mojaddam M, Mohseni A. Integrating machine learning and thermodynamic modeling for performance prediction and optimization of supercritical CO2 and gas turbine combined power systems. Thermal Science and Engineering Progress. 2024; 54: 102820. doi: 10.1016/j.tsep.2024.102820

4. da Silva JAM, Ávila Filho S, Carvalho M. Assessment of energy and exergy efficiencies in steam generators. Journal of the Brazilian Society of Mechanical Sciences and Engineering. 2017; 39: 3217–3226. doi: 10.1007/s40430-016-0704-6

5. Ibrahim TK, Mohammed MK, Awad OI, et al. A comprehensive review on the exergy analysis of combined cycle power plants. Renewable and Sustainable Energy Reviews. 2018; 90: 835–50. doi: 10.1016/j.rser.2018.03.072

6. Elwardany M, Nassib AM, Mohamed HA, Abdelaal M. Energy and exergy assessment of 750 MW combined cycle power plant: A case study. Energy Nexus. 2023; 12: 100251. doi: 10.1016/j.nexus.2023.100251

7. Elwardany M. Enhancing steam boiler efficiency through comprehensive energy and exergy analysis: A review. Process Safety and Environmental Protection. 2024; 184: 1222–50. doi: 10.1016/j.psep.2024.01.102

8. Pashchenko D, Mustafin R, Karpilov I. Ammonia-fired chemically recuperated gas turbine: Thermodynamic analysis of cycle and recuperation system. Energy. 2022; 252. doi: 10.1016/j.energy.2022.124081

9. Bartnik R, Hnydiuk-Stefan A, Buryn Z. Thermodynamic and economic analysis of a gas turbine set coupled with a turboexpander in a hierarchical gas-gas system. Energy. 2020; 190. doi: 10.1016/j.energy.2019.116394

10. Kim JS, Kim DY, Kim YT. Thermodynamic analysis of a dual loop cycle coupled with a marine gas turbine for waste heat recovery system using low global warming potential working fluids. Journal of Mechanical Science and Technology. 2019; 33: 3531–41. doi: 10.1007/s12206-019-0647-9

11. Shakib SE, Amidpour M, Esmaieli A, et al. Various approaches to thermodynamic optimization of a hybrid multi-effect evaporation with thermal vapour compression and reverse osmosis desalination system integrated to a gas turbine power plant. International Journal of Engineering, Transactions B: Applications. 2019; 32: 777–89. doi: 10.5829/ije.2019.32.05b.20

12. Khosravi H, Salehi G, Azad MT. Optimization and advance thermodynamic analysis of dual stage CO_2 power cycle combined to gas turbine. Heat and Mass Transfer/Waerme-Und Stoffuebertragung. 2020; 56: 75–94. doi: 10.1007/s00231-019-02688-w

13. Balku S. Analysis of combined cycle efficiency by simulation and optimization. Energy Conversion and Management. 2017; 148: 174–83. doi: 10.1016/j.enconman.2017.05.032

14. Elwardany M, Nassib AM, Mohamed HA. Analyzing global research trends in combined cycle power plants: A bibliometric study. Energy Nexus. 2024; 13: 100265. doi: 10.1016/j.nexus.2023.100265

15. Park Y, Choi M, Choi G. Thermodynamic performance study of large-scale industrial gas turbine with methane/ammonia/hydrogen blended fuels. Energy. 2023; 282: 128731. doi: 10.1016/j.energy.2023.128731

16. Abdalla MSM, Balli O, Adali OH, et al. Thermodynamic, sustainability, environmental and damage cost analyses of jet fuel starter gas turbine engine. Energy. 2023; 267: 126487. doi: 10.1016/j.energy.2022.126487

17. Tianliang W, Hong T. Thermodynamic and exergoeconomic analysis of an innovative cogeneration of power and freshwater based on gas turbine cycle. Energy. 2023; 285: 129454. doi: 10.1016/j.energy.2023.129454

18. Jaszczur M, Dudek M, Kolenda Z. Thermodynamic analysis of advanced gas turbine combined cycle integration with a high-temperature nuclear reactor and cogeneration unit. Energies. 2020; 13. doi: 10.3390/en13020400

19. Golchoobian H, Taheri MH, Saedodin S. Thermodynamic analysis of turboexpander and gas turbine hybrid system for gas pressure reduction station of a power plant. Case Studies in Thermal Engineering. 2019; 14. doi: 10.1016/j.csite.2019.100488

20. Arsalis A. Thermodynamic modeling and parametric study of a small-scale natural gas/hydrogen-fueled gas turbine system for decentralized applications. Sustainable Energy Technologies and Assessments. 2019; 36. doi: 10.1016/j.seta.2019.100560

21. Xie M, Xie Y, He Y, et al. Thermodynamic analysis and system design of the supercritical CO_2 Brayton cycle for waste heat recovery of gas turbine. Heat Transfer Research. 2020; 51: 129–46. doi: 10.1615/HeatTransRes.2019028447

22. Stathopoulos P, Rähse T, Vinkeloe J, Djordjevic N. First law thermodynamic analysis of the recuperated humphrey cycle for gas turbines with pressure gain combustion. Energy. 2020; 200. doi: 10.1016/j.energy.2020.117492

23. Pirkandi J, Penhani H, Maroufi A. Thermodynamic analysis of the performance of a hybrid system consisting of steam turbine, gas turbine and solid oxide fuel cell (SOFC-GT-ST). Energy Conversion and Management. 2020; 213. doi: 10.1016/j.enconman.2020.112816

24. Elwardany M, Nassib AM, Mohamed HA. Case Study: Exergy Analysis of a Gas Turbine Cycle Power Plant in Hot Weather Conditions. In: Proceedings of the 2023 5th Novel Intelligent and Leading Emerging Sciences Conference (NILES). pp. 291–294. doi: 10.1109/NILES59815.2023.10296731

25. Mrzljak V, Poljak I, Jelić M, Prpić-Oršić J. Thermodynamic Analysis and Improvement Potential of Helium Closed Cycle Gas Turbine Power Plant at Four Loads. Energies. 2023; 16. doi: 10.3390/en16155589

26. Ren J, Xu C, Qian Z, et al. Exergoeconomic Analysis and Optimization of a Biomass Integrated Gasification Combined Cycle Based on Externally Fired Gas Turbine, Steam Rankine Cycle, Organic Rankine Cycle, and Absorption Refrigeration Cycle. Entropy. 2024; 26. doi: 10.3390/e26060511

27. Elwardany M, Nassib AM, Mohamed HA. Exergy analysis of a gas turbine cycle power plant: a case study of power plant in Egypt. Journal of Thermal Analysis and Calorimetry. 2024. doi: 10.1007/s10973-024-13324-z

28. Aygun H, Caliskan H. Evaluating and modelling of thermodynamic and environmental parameters of a gas turbine engine and its components. Journal of Cleaner Production. 2022; 365: 132762. doi: 10.1016/j.jclepro.2022.132762

29. Skabelund BB, Jenkins CD, Stechel EB, Milcarek RJ. Thermodynamic and emission analysis of a hydrogen/methane fueled gas turbine. Energy Conversion and Management: X. 2023; 19: 100394. doi: 10.1016/j.ecmx.2023.100394

30. Jiang Z, Wang X, Yang S, Zhu M. A Deterministic Calibration Method for the Thermodynamic Model of Gas Turbines. Symmetry. 2024; 16. doi: 10.3390/sym16050522

31. Brahimi F, Madani B, Ghemmadi M. Comparative Thermodynamic Environmental and Economic Analyses of Combined Cycles Using Air and Supercritical CO2 in the Bottoming Cycles for Power Generation by Gas Turbine Waste Heat Recovery. Energies. 2022; 15. doi: 10.3390/en15239066

32. Elwardany M, Nassib AEM, Mohamed HA. Comparative Evaluation for Selected Gas Turbine Cycles. International Journal of Thermodynamics. 2023; 26: 57–67. doi: 10.5541/ijot.1268823

33. Sammour AA, Komarov OV, Qasim MA, Saleh AY. Investigation of the Influence of Ambient Conditions on the Thermodynamic Characteristics of Air as a Working Fluid for Gas Turbines. Journal of Advanced Research in Fluid Mechanics and Thermal Sciences. 2023; 106: 182–96. doi: 10.37934/arfmts.106.1.182196

34. Abed AM, Chauhan BS, Ayed H, et al. Thermodynamic, exergetic and environmental evaluation and optimization of a bio-fuel fired gas turbine incorporated with wind energy derived hydrogen injection. Case Studies in Thermal Engineering. 2024; 56: 104238. doi: 10.1016/j.csite.2024.104238

35. Almatrafi E, Khaliq A, Abuhabaya A. Thermodynamic and exergetic assessment of a biomass derived syngas fueled gas turbine powered trigeneration system. Case Studies in Thermal Engineering. 2022; 35: 102099. doi: 10.1016/j.csite.2022.102099

36. Al-Tameemi MRJ, Yahya SG, Hafedh SA, Azzawi IDJ. Thermodynamic optimization of an integrated gas turbine cycle, heat exchanger and organic Rankine cycle for co-generation of mechanical power and heating load. Journal of Computational and Applied Research in Mechanical Engineering. 2023; 13: 75–88. doi: 10.22061/jcarme.2023.9366.2253

37. Sasmoko, Lee SW, Bhavanari M, et al. Thermodynamic Analysis of Three Internal Reforming Protonic Ceramic Fuel Cell-Gas Turbine Hybrid Systems. Applied Sciences (Switzerland). 2022; 12. doi: 10.3390/app122111140

38. Alklaibi AM, Khan MN, Khan WA. Thermodynamic analysis of gas turbine with air bottoming cycle. Energy. 2016; 107: 603–11. doi: 10.1016/j.energy.2016.04.055

39. Elwardany M, Nassib AM, Mohamed HA, Abdelaal. Performance Assessment of Combined Cycle Power Plant. In: Proceedings of the 2023 5th Novel Intelligent and Leading Emerging Sciences Conference (NILES). pp. 80–84. doi: 10.1109/NILES59815.2023.10296617

40. Ibrahim TK, Basrawi F, Awad OI, et al. Thermal performance of gas turbine power plant based on exergy analysis. Applied

Thermal Engineering. 2017; 115: 977–85. doi: 10.1016/j.applthermaleng.2017.01.032

41. Kurt H, Recebli Z, Gedik E. Performance analysis of open cycle gas turbines. International Journal of Energy Research. 2009; 33: 285–294. doi: 10.1002/er.1472

42. De Sa A, Al Zubaidy S. Gas turbine performance at varying ambient temperature. Applied Thermal Engineering. 2011; 31: 2735–9. doi: 10.1016/j.applthermaleng.2011.04.045

43. Abou Al-Sood MM, Matrawy KK, Abdel-Rahim YM. Optimum Operating Parameters of an Irreversible Gas Turbine Cycle. JES Journal of Engineering Sciences. 2012; 40: 1695–714. doi: 10.21608/jesaun.2012.114611

44. Salah SA, Abbas EF, Ali OM, et al. Evaluation of the gas turbine unit in the Kirkuk gas power plant to analyse the energy and exergy using ChemCad simulation. International Journal of Low-Carbon Technologies. 2022; 17: 603–10. doi: 10.1093/ijlct/ctac034

45. Ahmadi GR, Toghraie D. Energy and exergy analysis of Montazeri Steam Power Plant in Iran. Renewable and Sustainable Energy Reviews. 2016; 56: 454–63. doi: 10.1016/j.rser.2015.11.074

46. Çengel Y, Boles M. Thermodynamics: an engineering approach, 5th ed. McGraw-Hill Science/Engineering/Math; 2005.

47. Ersayin E, Ozgener L. Performance analysis of combined cycle power plants: A case study. Renewable and Sustainable Energy Reviews. 2015; 43: 832–42. doi: 10.1016/j.rser.2014.11.082

48. Dincer I, Rosen MA. Chemical exergy. Exergy. 2021: 37–60. doi: 10.1016/b978-0-12-824372-5.00003-8

Article

Design and performance analysis of a net-zero energy building in Owerri, Nigeria

Godswill N. Nwaji[1,*], **Kennedy C. Dimson**[1], **Olisaemeka C. Nwufo**[1], **Nnamdi V. Ogueke**[1,2], **Emmanuel E. Anyanwu**[1]

[1] Department of Mechanical Engineering, School of Engineering and Engineering Technology, Federal University of Technology, Owerri 460114, Nigeria

[2] African Center of Excellence on Future Energies and Electrochemical Systems (ACE-FUELS), Federal University of Technology, Owerri 460114, Nigeria

* Corresponding author: Godswill N. Nwaji, godswillmee@gmail.com

Abstract: Building cooling load depends on heat gains from the outside environment. Appropriate orientation and masonry materials play vital roles in the reduction of overall thermal loads buildings. A net-zero energy building performance has been analyzed in order to ascertain the optimum orientation and wall material properties, under the climatic conditions of Owerri, Nigeria. Standard cooling load estimation techniques were employed for the determination of the diurnal interior load variations in a building incorporating renewable energy as the major energy source, and compared with the situation in a conventionally powered building. The results show a 19.28% reduction in the building's cooling load when brick masonry was used for the wall construction. It was observed that a higher heat gain occurred when the building faced the East-West direction than when it was oriented in the North-South direction. Significant diurnal cooling loads variation as a result of radiation through the windows was also observed, with the east facing windows contributing significantly higher loads during the morning hours while the west facing windows contributed higher amounts in the evening. The economic analysis of the net-zero energy building showed an 11.63% reduction in energy cost compared to the conventional building, with a 7-year payback period for the use of Solar PV systems. Therefore, the concept of net-zero energy building will not only help in energy conservation, but also in cost savings, and the reduction of carbon footprint in the built environment.

Keywords: renewable integration; built environment; energy; net-zero; building; orientation; cooling load

1. Introduction

About 40% of greenhouse gas emissions and the world's energy consumption respectively, are attributed to buildings, and as a result of this energy being sourced mostly through fossil fuel, its negative impacts on the environment cannot be over emphasized. This negative impact will most likely become worse as more buildings continue to spring up as a result of the ever-increasing population [1,2]. As at 2016 in Nigeria, residential buildings already accounted for close to 50% of the nation's electricity consumption [3], and this has continued to rise with the increase in the population, and rise in rural-urban migration. Though energy crisis is a global phenomenon, Nigeria's inability to generate sufficient electricity, coupled with its increasing load demand (driven by increasing population and rural-urban migration), has further made the energy crisis in the country more critical. This has led to limited

energy availability and access to the populace, which in turn has negatively affected the socio-economic development of the country. There is therefore, the need to ensure energy conservation and efficiency in buildings in order to reduce building energy demand.

To effectively design a net zero energy building, one of the important factors to consider is the passive techniques that when incorporated minimize the energy requirements for meeting the normal demands of the building, and ensure less greenhouse gas emission. Bio-climatic architecture, essentially based on climate considerations, with the aim of achieving physical comfort for the occupants of the building with minimum use of resources is promising for achieving net zero energy buildings. Some of these techniques include building orientation, building form, building materials, glazing, incorporation of renewable energy, etc. [3].

Building orientation takes into consideration the path of the sun when erecting the building to minimize exposing surfaces of the building to solar irradiation [4]. Morrissey et al. [5] pointed out that building orientation is the most important parameter when it comes to factors considered in passive solar design of buildings since it determines the amount of direct solar irradiation received by the building. The greatest energy saving obtained when a building was oriented 30°, 45° and 60° along its southern axis was when the longest walls faced 30° to the south, which is in line with the growing consensus that the best option is to orient buildings 20°–30° to the south [6,7]. In their study, Odunfa et al. [8] and Ochedi and Taki [9] all reported a reduction in solar gains when the longest side of the building faces the North-South direction.

Reduction of heat gain in buildings can be achieved through compact building forms (low surface-volume ratio) [3]. About 36% energy savings can be achieved with the appropriate building form and orientation [10].

With the help of low energy materials and efficient structural design, the energy demand of a building can be reduced. Akande et al. [11] is of the opinion that a reliable approach towards sustaining energy efficiency in residential buildings in Nigeria is to reduce the use of energy intensive materials such as glass and steel in the construction of buildings. Reflective materials and light colours have reduced heat gains by about 30% during peak sun periods [12]; and the use of brick masonry against concrete walls have resulted in significant energy reductions in buildings [8,13]. Windows significantly affect building energy performance [2,14–16]. They account for about 60% of the overall energy loss of buildings, resulting from conduction, convection and radiation [17]. This adds to building cooling and heating loads [14,18]. Therefore, optimum design and sizing of windows reduces the building energy consumption [19]. Proper window orientation reduces heat gains [16]. Rawat et al. [20] have studied the effect of window orientation in North East India, while Ahmed [14] also simulated the effects of window orientation on a building in Gaza Strip.

Renewable energy systems when integrated in a building meet the energy loads/demands of the building in an environmentally friendly manner. When renewable energy systems are used to meet the energy requirements of buildings, no GHGs are emitted. Usman [21] opined that choosing the right type and the right quantity of renewable energy for use in buildings is the most influential factor in actualizing a net-zero energy building. He reported that an output of 3484 kWh from

a solar PV system was able to meet almost the total annual electricity load (3720.3 kWh) of a typical building. A study in Andalusia showed that about 78.89% of residential building energy demands can be satisfied with rooftop solar PV systems, while in the city of Al-Khobar, Saudi Arabia, a similar study showed that 19% of electricity demands of the villas and apartment buildings can be offset using rooftop solar PV systems [22]. Passive nocturnal radiation cooling can be utilized in the cooling of buildings thereby ensuring energy conservation and reduction in greenhouse gas emission [23–26]. This study therefore seeks to design and carry out a performance analysis of a net-zero energy building in Owerri, Nigeria. It undertakes a comprehensive analysis of a conceptual building envelope with respect to the cooling and heating loads, and the effects of building orientations as well as masonry materials on the energy performance of the building.

2. Methodology

The floor plan of the conceptual building model is shown in **Figure 1**. The apartment comprises different major zones including four bedrooms labeled BR1, BR2, BR3 and BR4, lounge, and kitchen. The specifications of the major zones are given in **Table 1**, while the envelop properties are shown in **Tables 2** and **3**. According to Trane [27], the principles of heat transfer play prime roles in achieving and maintain a comfortable indoor condition in buildings. This is applied in estimating the cooling and heating loads of the model building.
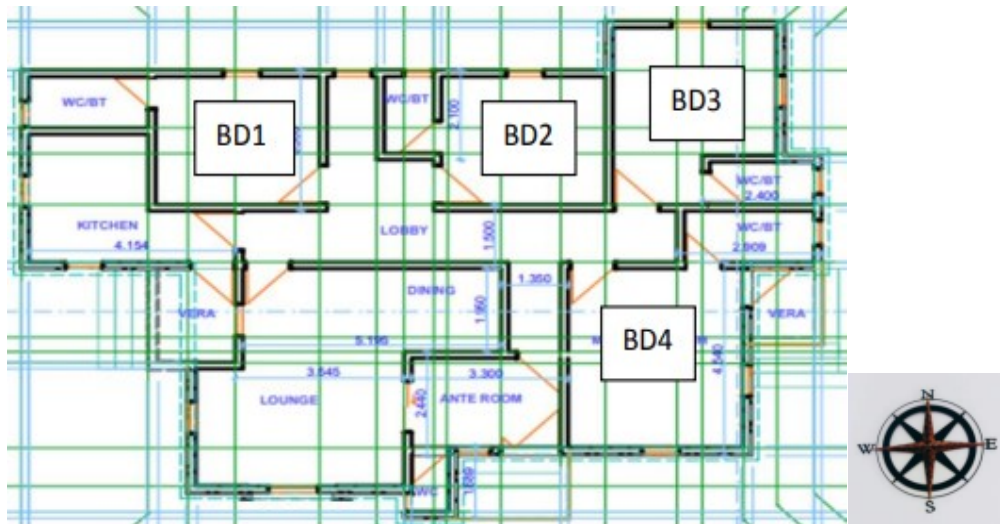
Figure 1. Floor plan of the designed building.

Table 1. The building specifications.

S/N	Zone	Dimension (m)	Area (m²)	Volume (m³)
1	BD 1	3.05 × 3.66 ×2.71	11.20	30.4
2	BD 2	3.66 × 3.66 × 2.71	13.40	36.3
3	BD 3	3.75 × 4.15 × 2.71	15.60	42.3
4	BD 4	3.75 × 4.15 × 2.71	15.60	42.3
5	Lounge	4.20 × 4.80 × 2.71	20.16	54.6
6	Kitchen	3.60 × 3.00 × 2.71	10.80	29.30

Table 2. Envelop properties.

S/N	Envelope part	Type	Insulation thickness (m)	U-value (W/m²K)
		Brick Mansory	0.01	0.31
1.	Walls	Solid Cement Block	0.01	0.36
		Hollow Cement Block	0.01	0.37
2.	Roof			3.447

Table 3. Window properties.

S/N	Zone	Window type	Dimension (m)	Area (m²)	U-value (W/m²k)
1	BD1, BD2, BD3, BD4, Lounge, Kitchen	double leaf, 6.4mm uncoated single glazing type, with aluminum frame and thermal breaks	0.610 × 0.914	0.5575	5.43

In cooling load calculation, cooling loads are broadly classified into two, external loads and internal loads [8].

The external loads evaluated include heat gain from conduction through shaded walls, cooling loads arising from sunlit surfaces, radiation gain from the windows, loads arising from ventilation and air infiltration into the building.

Heat gain from conduction through surfaces (a shaded wall) is given as [27]:

$$Q_{cond} = U \times A \times \Delta T \tag{1}$$

U is the overall heat transfer coefficient of the wall expressed as:

$$U = \frac{1}{R1 + R2 + R3 + R4 + R5} \tag{2}$$

where R1 is the outdoor air film resistance, R2 is the external cement plaster resistance, R3 is the block resistance, R4 is the inside cement plaster resistance, and R5 is the indoor air film resistance.

A is the net surface area of the wall expressed as:

$$A = (L_R H_R) - (L_w B_w) \tag{3}$$

ΔT is the dry bulb temperature difference across the surface.

The cooling loads resulting from direct sunlight on the walls, windows and roof, respectively (i.e., cooling load from sunlit surfaces) is given as [8,27,28]:

$$(Q_{cond}, SL)_{wa} = U_{wa} \times A_{wa} \times CLTD_{wa} \tag{4}$$
$$(Q_{cond}, SL)_{win} = U_{win} \times A_{win} \times CLTD_{win} \tag{5}$$
$$(Q_{cond}, SL)_r = U_r \times A_r \times CLTD_r \tag{6}$$

CLTD is the cooling load temperature difference which accounts for the heat added as a result of the sun shining on these exterior surfaces, and their capacity to store up heat [27].

The heat gain by radiation heat transfer through the windows is given as [27]

$$Q_{rad} = A_w \times SC \times SCL \tag{7}$$

where SC is the shading coefficient of the window, and SCL is the solar cooling factor [27].

Heat gain as a result of air infiltration into the room can be simplified as

$$Q_{infil} = \frac{\text{volume of space } \times \text{ air change rate per hour}}{3600}(1200\Delta T + 3010\Delta W) \quad (8)$$

where ΔT is the design outdoor dry-bulb temperature minus the desired indoor dry bulb temperature, and ΔW is the design outdoor humidity ratio minus the desired indoor humidity.

Heat gain as a result of ventilation can also be simplified as

$$Q_{vent} = Number\ of\ people \times (12.1\Delta T + 30.1\Delta W) \quad (9)$$

The occupants, light bulbs and appliances in the building make up the internal heat loads [27,28]. The total load emanating from the occupants is given as:

$$Q_{people} = Number\ of\ people\ ((SHGPP \times CLF) + LHGPP) \quad (10)$$

where SHGPP and LHGPP are the sensible and latent heat gain per person, while CLF is the cooling load factor which accounts for the capacity of the space to absorb and store heat released from the occupants.

The heat gained internally as a result of light bulbs is given as [27];

$$Q_{bulbs} = wattage_{bulbs} \times ballast\ factor \times CLF \quad (11)$$

The internal heat gain as a result of appliances is given as [27];

$$Q_{appliances} = Wattage_{app} \times Area \quad (12)$$

Therefore, the total heat gain can be given as:

$$Q_{total} = Q_{external} + Q_{internal} \quad (13)$$

Combining Eqs 1 to 11 results in the total heat gain in any the major zones of **Figure 1**. Hence, Q_{total} is expressed as:

$$
\begin{aligned}
Q_{total} = ((&\frac{1}{R1 + R2 + R3 + R4 + R5} + ((L_R H_R) - (L_W B_W)) \times \Delta T)) + (U \times A \times \Delta T)_{Roof} \\
&+ (U_{wa} \times A_{wa} \times CLTD_{wa}) + (U_{win} \times A_{win} \times CLTD_{win}) + (U_r \times A_r \times CLTD_r) \\
&+ (A \times SC \times SCL) + (\frac{\text{volume of space} \times \text{air change rate per hour}}{3600}(1200\Delta T + 3010\Delta W)) \\
&+ (Number\ of\ people \times \Delta T \times 33.76)) + (Number\ of\ people\ ((SHGPP \times CLF) + LHGPP) \\
&+ (wattage_{bulbs} \times Ballast\ Factor \times CLF) + (Wattage_{app} \times Area)
\end{aligned}
\quad (14)
$$

The appliances and their ratings, in the different zones of the building that served as load inputs into the analysis are listed for each zone in **Tables 4–8**.

Table 4. Appliances present in the lounge with their wattage.

S/N	Appliances	Wattage	Number	Total wattage
1	Ceiling fan	75	2	150
2	Television	100	1	100
3	Water dispenser	700	1	700
4	**Total**			**950**

Table 5. Appliances present in the bedrooms 1 and 2 with their wattage.

S/N	Appliances	Wattage	Number	Total wattage
1	Ceiling fan	75	1	75
	Total			**75**

Table 6. Appliances present in bedroom 3 with their wattage.

S/N	Appliances	Wattage	Number	Total wattage
1	Ceiling fan	75	1	75
2	Personal Computer	125	1	125
	Total			**200**

Table 7. Appliances present in bedroom 4 with their wattage.

S/N	Appliances	Wattage	Number	Total wattage
1	Ceiling fan	75	1	75
2	Personal computer	125	1	125
3	Television	100	1	100
	Total			**300**

Table 8. Appliances present in the kitchen with their wattage.

| S/N	Appliances	Wattage	Number	Total wattage
1	Ceiling fan	75	1	75
2	Freezer	320	1	320
3	Microwave	900	1	900
	Total			**1295**

3. Results and discussion

As shown in **Figure 2** for the Lounge, the internal heat generation with a total cooling load of about 20 kW contributed the highest cooling load in the South-West (SW) orientation as well as the East-West orientation. The kitchen played a significant role in both orientations in increasing the cooling load, contributing about 14.5 kW each., followed by bedrooms 4 and 3, each contributing about 5kW in both orientations. It can be observed that the contributions from conduction, sunlit surfaces, radiation, and infiltration for the different zones and orientations are marginal, whereas that from ventilation is noticeable. Floor areas, number of exposed surfaces, appliances and direction all influenced the contributions made by the zones to the overall cooling load of the building. BD1 has the least cooling load, approximately 1.96 kW, while BD2 has a load of 2.1 kW. Though they have the same number of exposed walls facing the same direction (North), their floor areas are different. Also, in BD1 and BD2, the East-West orientation records a higher cooling load than the North-South orientation. Similarly, BD3 and BD4 have cooling loads of 4.4 kW and 6 kW, respectively, though with same floor areas and number of exposed walls. The variation occurred because the walls faced different directions. The energy intensive appliances in the kitchen influenced the topmost load contribution.
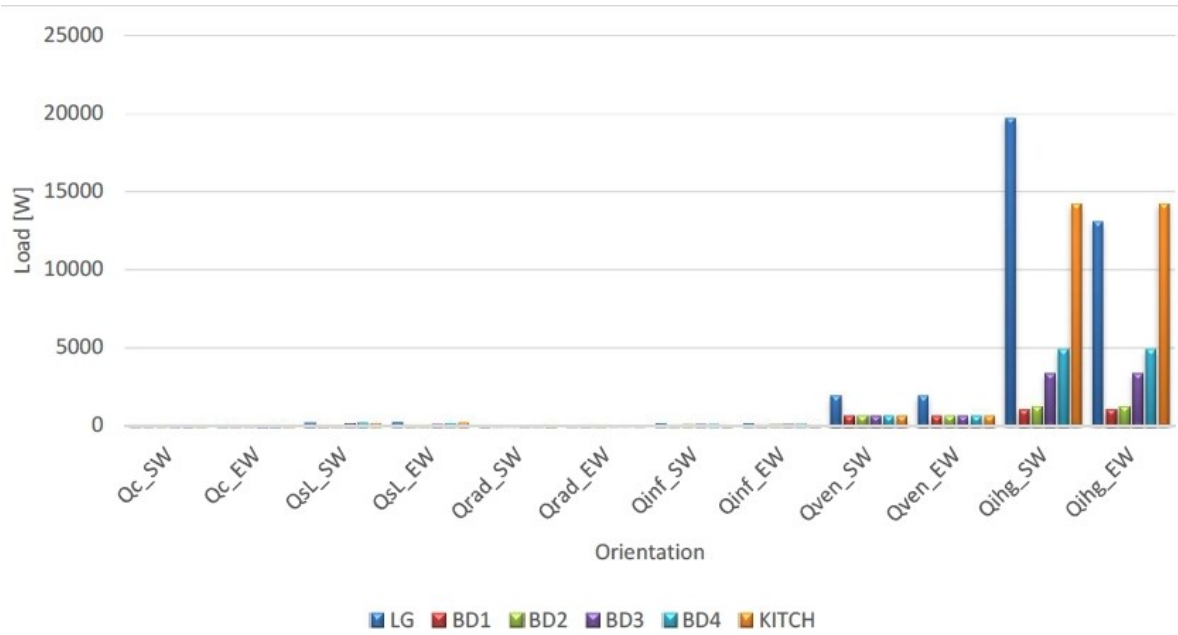
Figure 2. Building zonal loads for N-S and E-W orientations.

Figure 3 shows that the Lounge which has the highest floor area and with two exposed walls had the highest external cooling load of 4.8 kW. Also, the total external loads of the kitchen exceed those of BD1 and BD2 due to the simple reason that it has higher number of exposed walls. This consistent with the findings of Usman [21], that larger floor areas and exposed walls increase cooling load.
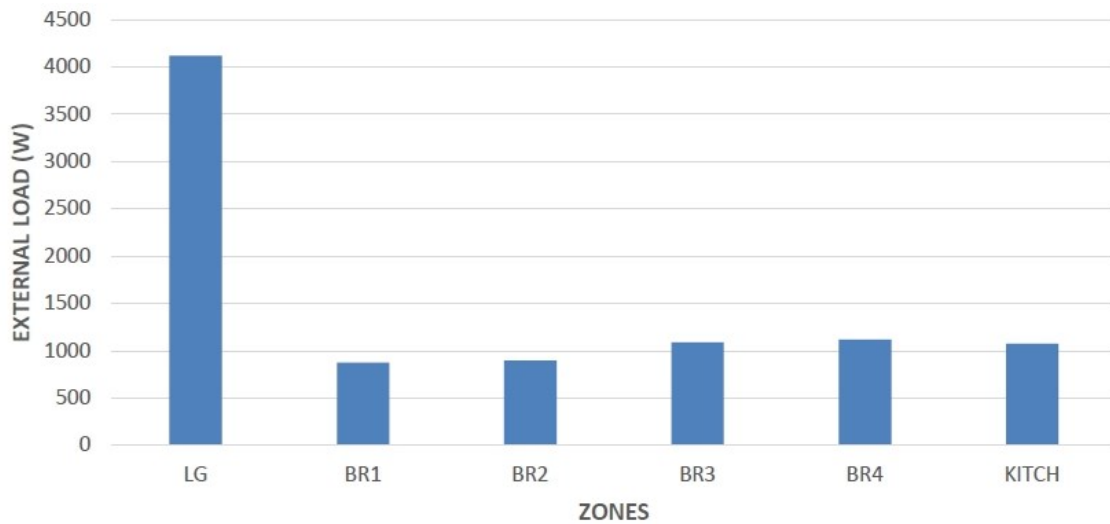
Figure 3. Total external loads of the zones.

Figure 4 shows time-dependent cooling loads arising from conduction through the walls, and radiation through the windows of the lounge facing different directions. The west facing wall contributed more to the cooling load in the early hours of the morning, but reduces as the sun rises, but then starts increasing from the evening hours and reaches its peak with 0.12 kW around 10:00 pm. This trend shows that the west facing wall absorbs a large amount of heat during the period when the sun is facing that direction (when the sun is setting), and gradually releases the absorbed heat into

the room, hence increasing the cooling load. The south facing wall also followed a similar pattern, but contributed less than the west wall with a peak cooling load of 0.09 kW around 7:00 pm. The cooling loads as a result of radiation through the windows were seen to be higher in the west facing window than the south facing window. The cooling loads gradually increased as the day broke for both the west and south windows, but while it peaked at 0.03 kW around 12 noon for the south window, it continued to rise for the west window, and finally peaked at 0.06 kW by 5:00 pm before gradually decreasing.
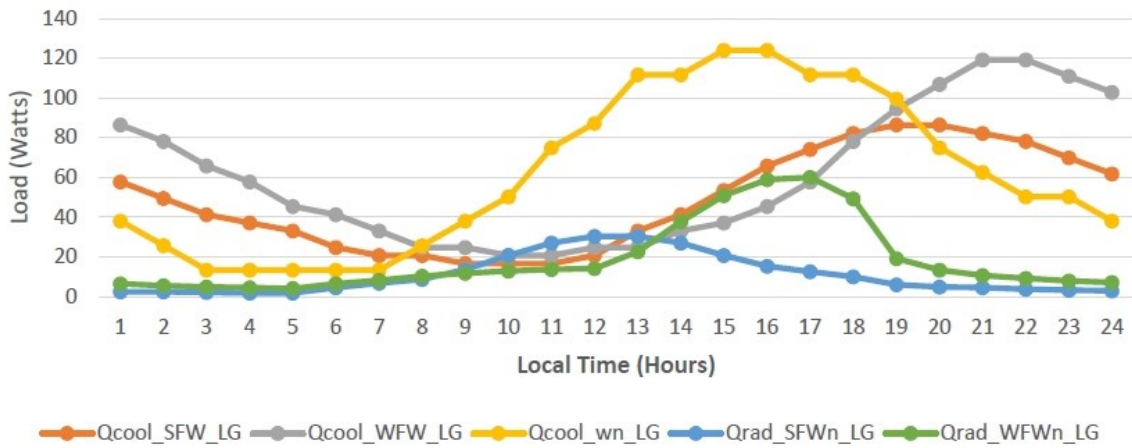

Figure 4. Orientation dependent cooling load of the lounge.

Figure 5 shows that for BD1 and BD2 with their only exposed walls facing the north, the cooling load contributed by the wall showed similar pattern as that of **Figure 4** but peaked at 0.05 kW between 9:00 and 10:00 pm. Though the radiation cooling load in **Figure 5** maintained the trend of **Figure 4**, it can be seen that it contributed far less cooling load than the lounge, reaching its peak of 0.013 kW around 12 noon, and sustained it with little variations till 6:00 pm, and thereafter decreased. This showed a great reduction in the cooling load through radiation when compared to the west facing window.
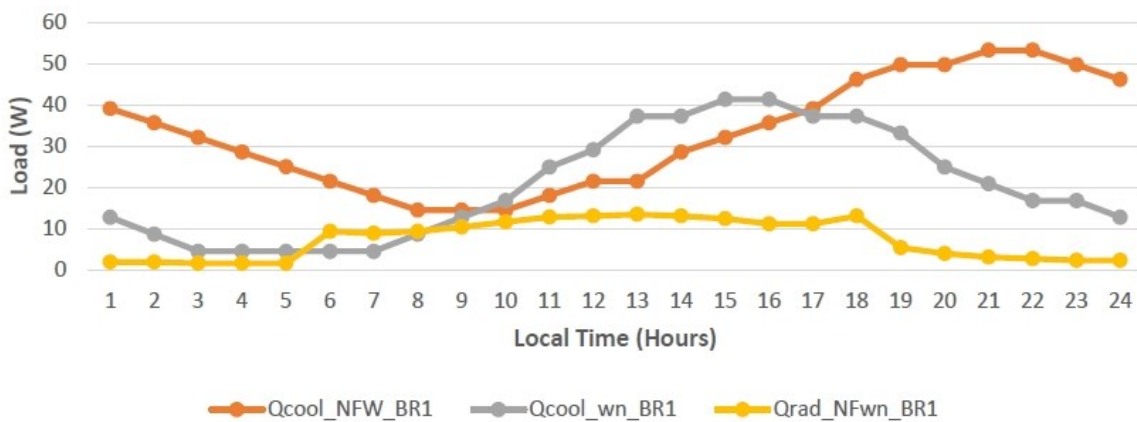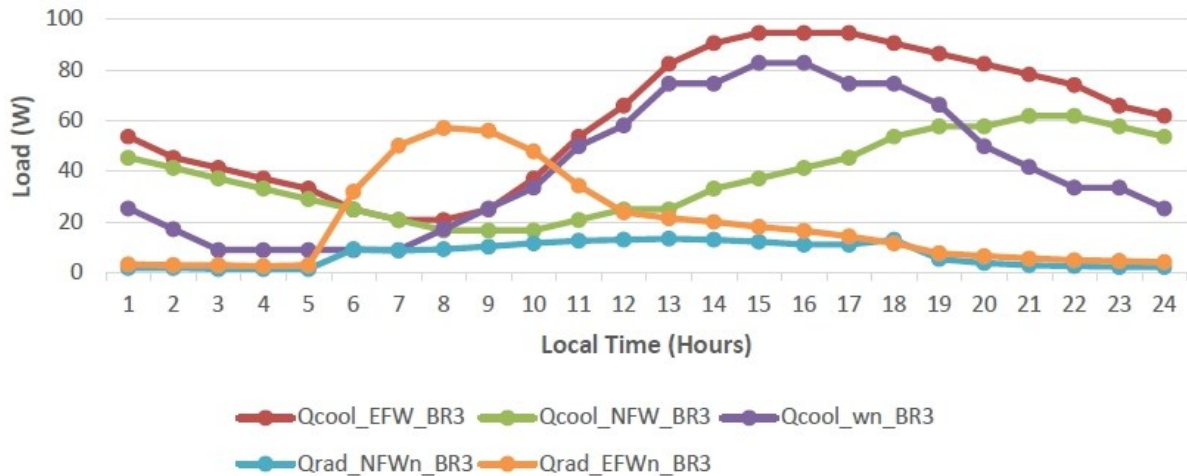

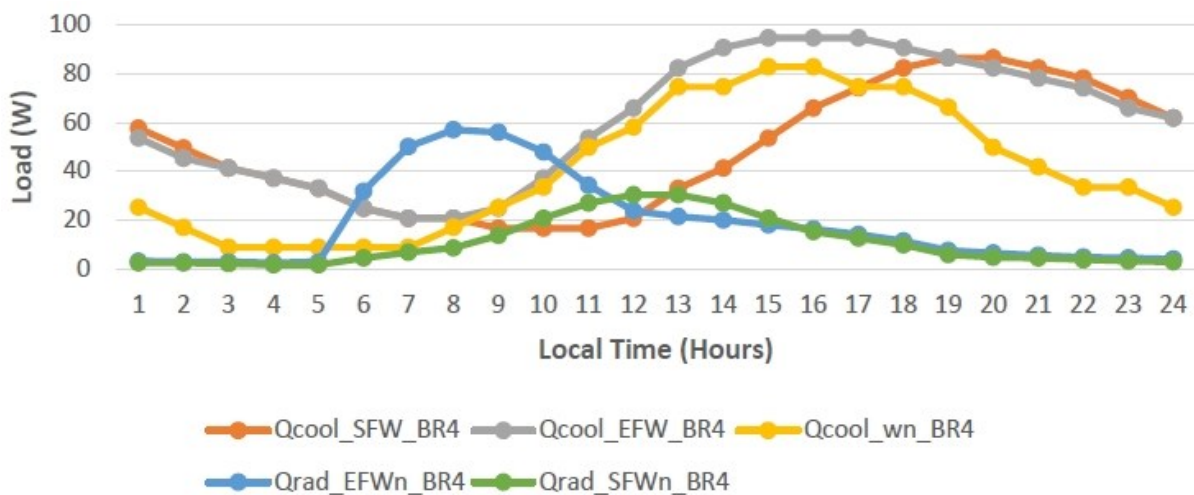**Figure 5.** Orientation dependent cooling loads of BD1 and BD2.

The North facing wall and window of BD3 followed the same as that of BD1 and BD2, as can be seen in **Figure 6**. The wall area influences the cooling load in this zone

significantly. The radiation cooling load was exactly the same, as the window areas remained the same. But unlike the west facing window of the lounge (**Figure 4**), it can be seen that radiation cooling load of the east facing window peaked in the morning hours of the day at 8:00 am attaining 0.057 kW. Around 3:00 pm, the east facing wall reached its peak with a cooling load of 0.096 kW, showing similar trend of absorbing heat when the sun is facing that direction (as the sun rises), and releasing it into the zone as the sun moves away from that direction.
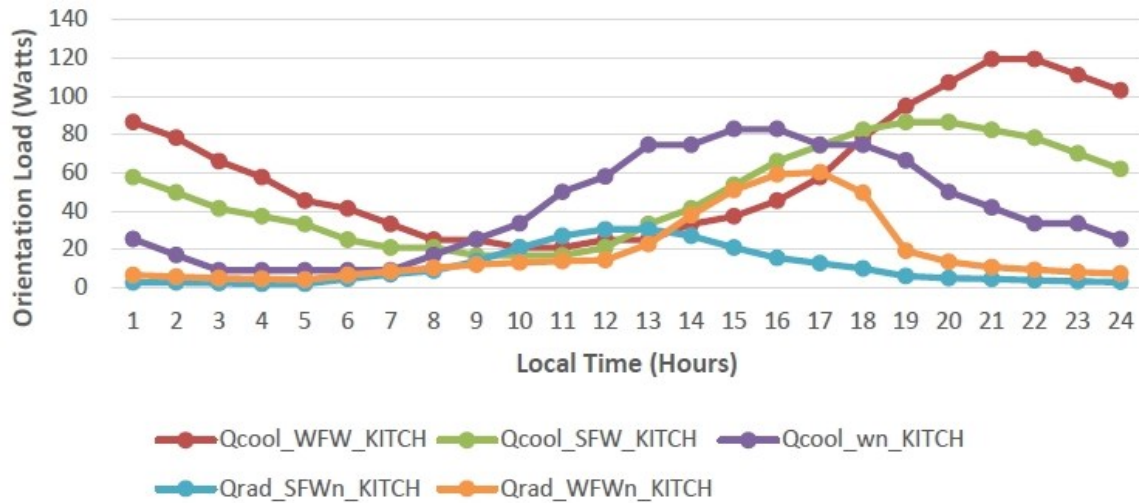

Figure 6. Orientation dependent cooling loads of BD3.

Figure 7 shows that the south facing walls and windows in BD4 followed the same pattern as the south facing wall and window of the lounge, while its east facing walls and window follows the east facing wall and window of BD3 respectively.


Figure 7. Orientation dependent cooling load of BD4.

It is clearly shown in **Figure 8** that the kitchen also maintained the same pattern as the lounge because their walls and windows faced the same direction. The only difference recorded is the amount of cooling load contributed through the walls, as a result of variations in wall areas.

Figure 8. Orientation dependent cooling load of the Kitchen.

The result of the parametric analysis of the impact of window orientation on the energy performance of the building is shown in **Figure 9**. It compares the heat gained as a result of radiation through the windows of the building. It gives a clearer view of the contributions of the windows facing different directions to the total radiation heat gain. As can be seen, while the east facing windows contributed more significantly to the total cooling load in the morning hours, the west facing windows contributed more in the evening hours. The north facing windows contributed significantly less to the overall total heat gain throughout the day. Right orientation reduces heat gain into the building envelope, with the south-north orientation being the most optimum [8,9]. Therefore, the optimum orientation is one that reduces openings in the East and West directions during the day because the rising of the sun from the east and setting of same in the west make it difficult to prevent radiations from entering through these zones since they have low sun angles during these periods. The report of FMPWH [3], and findings of Ahmed [14], Soudbaksh et al. [17] and Djokovic et al. [19] all support the above observation.
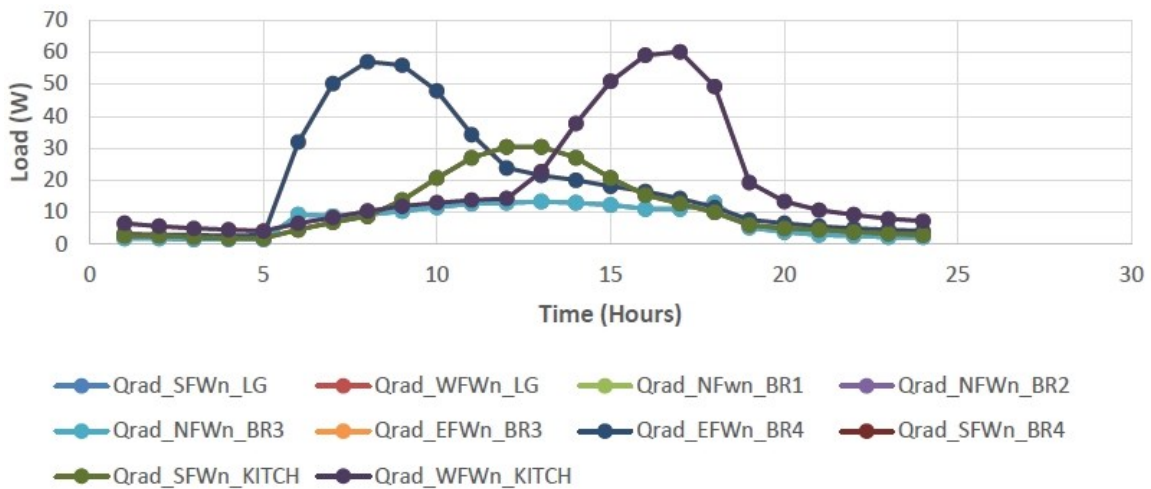
Figure 9. Comparative heat gain through radiation from all the windows.

Figure 10 shows the parametric effect of the U-values of masonry (wall) materials on the cooling loads of the different zones of the buildings in the south and west directions. It is observed that the brick masonry contributed a lower heat gain than its counterparts (the hollow and solid cement blocks), irrespective of the direction the wall is facing. This is in agreement with the work carried out by Ede et al. [13], who showed that brick walls contributed a lower heat gain compared to concrete walls. Odunfa et al. [8] also demonstrated that indeed the brick masonry when used as the wall materials reduces the cooling load compared to the regular blocks used in wall construction in Nigeria.
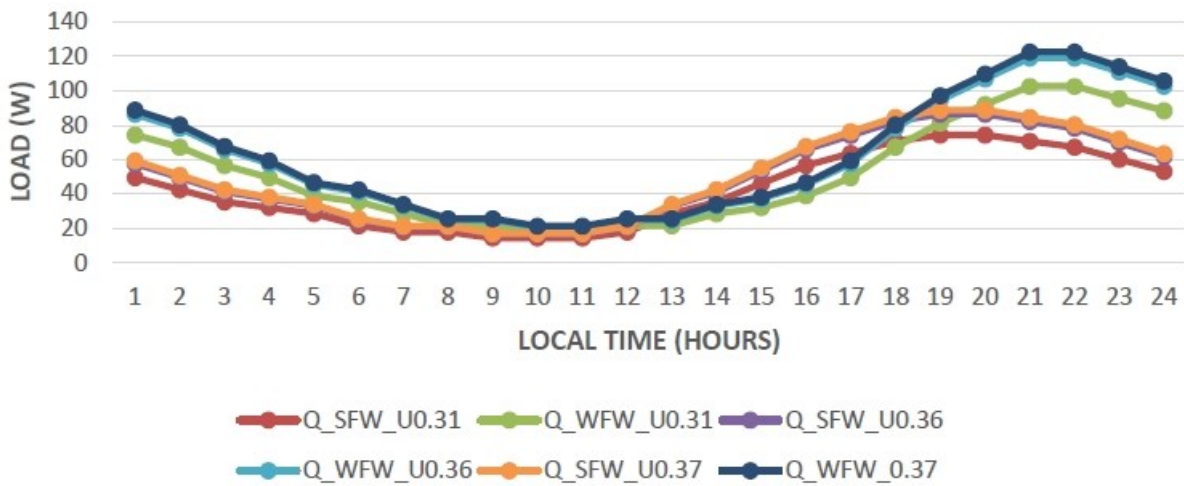
Figure 10. Effect of the wall U-values on the cooling loads.

The parameters of the incorporated solar PV system are presented in **Table 9**. It shows the quantity of solar panels and batteries needed to provide the required power for the building. Economic analysis of the system was carried out to determine the comparative energy cost of the conventional system and the renewable energy driven system, and the results of the analysis are shown in **Table 10**. It shows that about ₦3,450,695.61 will be saved if the recommended passive solar techniques are used rather than the regular conventional sources. From **Table 11**, a total of ₦24,301,950 is needed as initial capital cost of installing a solar PV system. However, with the annual savings of about ₦3,450,695.61 for adopting the alternative system, the payback period is 7 years when it is adopted to provide the energy needed in the building.

Table 9. Solar PV system design parameters.

Parameters	Design values
Module power (watt)	315
No. of modules in series	04
No. of modules in parallel	27
Total capacity of solar panel arrays	34
Operating DC voltage	24
Regulator efficiency	0.9
Output power capacity of inverter (Kw)	24

Table 9. (*Continued*).

Parameters	Design values
Inverter efficiency	0.9
Battery depth discharge	0.6
Battery backup days	2
Battery cell capacity	1000 Ah
Battery cell voltage	2 V
No. of cells in series	12
No. of cells in parallel	8

Table 10. Cost savings using the recommended passive techniques.

	Regular model	Recommended model
Total Energy in a day (W)	2,227,140	1,968,056.4
Total energy in a year (365 days)	812,906,100	718,340,586
Daily bill (@ (₦36.49 per kWhr) + ₦383.14 VAT) (₦)	81,651.48	72,197.52
Yearly bill (₦)	**29,663,326.73**	**26,212,631.12**

Table 11. Payback period for the solar PV system.

S/N	Parameters	Estimate
1	Cost of solar system installation	₦24,301,950
2	Annual savings	₦3,450,695.61
3	Payback period	7 years

4. Conclusion

A net-zero energy building has been designed and analyzed using Excel statistical tool. By implementing some passive cooling techniques to cut down on the cooling load of the building, space cooling costs and carbon footprints are amenable to drastic reduction. The major findings from this study are:

- Cooling loads of a building are dependent on the amount of heat gained from the outside through the fenestrations. The brick masonry reduced the amount of cooling loads compared to the regular solid and hollow blocks normally used for building constructions in Owerri.
- The optimum orientation for energy efficiency and best performance is the North-South direction as it ensures that the building has a lower cooling load.
- Windows facing the east and west directions contributed higher heat gains during the morning and evening hours of the day, respectively; therefore, it is advisable to minimize window openings in those directions, while maximizing window openings in the north and south directions, especially the north direction, as it contributed the least amount of heat gain.
- The amount spent on electricity bill to meet the cooling load requirement of the building was reduced by ₦3,450,695.61 when the optimum orientation and low energy wall materials were used, with a payback period of 7 years for integrating a solar PV system as a sole energy source for the building.

Conflict of interest: The authors declare no conflict of interest.

References

1. Lee JW, Jung HJ, Park JY, et al. Optimization of building window system in Asian regions by analyzing solar heat gain and daylighting elements. Renewable Energy. 2013; 50: 522-531. doi: 10.1016/j.renene.2012.07.029

2. Mebarki C, Djakab E, El Hassar SMK, et al. Impact of glazing type and orientation on the optimum dimension of windows for office room in hot climate. Journal of Architectural Environment & Structural Engineering Research. 2018; 1(1): 10-15. doi: 10.30564/jaeser.v1i1.271

3. Federal Ministry of Power, Works and Housing (Housing). Building energy efficiency guideline for Nigeria. Federal Ministry of Power, Works and Housing (Housing); 2016.

4. Abdullahi ML. Integrating principles of passive cooling in the design of five star hotel in Minna. Ahmadu Bello University, Zaria, Nigeria; 2017; Unpublished work.

5. Morrissey J, Moore T, Horne RE. Affordable passive solar design in a temperate climate: An experiment in residential building orientation. Renewable Energy. 2011; 36(2): 568-577. doi: 10.1016/j.renene.2010.08.013

6. Littlefair P. Daylight, sunlight and solar gain in the urban environment. Solar Energy. 2001; 70(3): 177-185. doi: 10.1016/S0038-092X(00)00099-2

7. Pacheco R, Ordóñez J, Martínez G. Energy efficient design of building: A review. Renewable and Sustainable Energy Reviews. 2012; 16(6): 3559-3573. doi: 10.1016/j.rser.2012.03.045

8. Odunfa KM, Nnakwe CJ, Odunfa VO. Building Energy Efficiency in Nigeria Major Climatic Zones. Journal of Building Construction and Planning Research. 2018; 06(04): 251-266. doi: 10.4236/jbcpr.2018.64017

9. Ochedi DET, Taki DA. Energy Efficient Building Design in Nigeria: An Assessment of the Effect of the Sun on Energy Consumption in Residential Buildings. JOURNAL OF ENGINEERING AND ARCHITECTURE. 2019; 7(1). doi: 10.15640/jea.v7n1a6

10. Aksoy UT, Inalli M. Impacts of some building passive design parameters on heating demand for a cold region. Building and Environment. 2006; 41(12): 1742-1754. doi: 10.1016/j.buildenv.2005.07.011

11. Akande OK, Fabiyi O, Mark IC. Sustainable Approach to Developing Energy Efficient Buildings for Resilient Future of the Built Environment in Nigeria. American Journal of Civil Engineering and Architechture. 2015; 3(4): 144-152.

12. Akbari H, Davis S. Cooling Our Communities: A Guidebook on Tree Planting and Light-Colored Surfacing. (Huang J, Dorsano S, Winnett S, eds.). Office of Scientific and Technical Information (OSTI); 1992. doi: 10.2172/5032229

13. Ede AN, Olofinnade ON, Enyi-Abonta E, Bamibgoye GO. Implications of Construction Materials on Energy Efficiency of Buildings in Tropical Regions. International Journal of Applied Engineering Research. 2017; 12(18): 7873-7883.

14. Ahmed EK. Effect of Windows Size, Position and Orientation on the Amount of Energy Needed for Winter Heating and Summer Cooling. Journal Of Engineering Research and Technology. 2017; 1(1): 1-8.

15. Fariha S, Ashikur RJ. Performance Evaluation of Window Location and Configuration to Improve Daylighting of Residential Apartment Buildings. In: Proceedings of the 2018 International Conference on Green Architecture (ICGrA); 12-14 July 2018; Dhaka, Bangladesh. pp. 12-14.

16. Rashid M, Ahmad T, Malik AM, et al. Effects of orientation and glazing material on heat gain in semi-arid climate of Lahore. University of Engineering and Technology Taxila. Technical Journal. 2016; 21(4): 38.

17. Soudbaksh K, Etminan M, Hakimazari M, Salavatian S. Impacts of Window Factors and Building Orientation on Energy Consumption in Residential Buildings of Humid Temperate Climatic Zone in Iran. Journal of Construction in Developing Countries. 2022; 27(2): 235-262. doi: 10.21315/jcdc-04-21-0061

18. Detsi M, Manolitsis A, Atsonios I, et al. Energy Savings in an Office Building with High WWR Using Glazing Systems Combining Thermochromic and Electrochromic Layers. Energies. 2020; 13(11): 3020. doi: 10.3390/en13113020

19. Djoković JM, Nikolić RR, Bujnak J, et al. Selection of the Optimal Window Type and Orientation for the Two Cities in Serbia and One in Slovakia. Energies. 2022; 15(1): 323. doi: 10.3390/en15010323

20. Rawat V, Shivankar S, Das B, et al. Effect of Orientation of Window on Building Heat Load: Perspective of N-E India. IOP Conference Series: Materials Science and Engineering. 2017; 225: 012166. doi: 10.1088/1757-899x/225/1/012166

21. Usman M. Design and performance analysis of energy efficient building in Pakistan. University of Engineering and Technology, Taxila, Pakistan; 2016; Unpublished work.

22. Dalal R, Bansal K, Thapar S. Bridging the energy gap of India's residential buildings by using rooftop solar PV systems for higher energy stars. Clean Energy. 2021; 5(3): 423-432. doi: 10.1093/ce/zkab017

23. Parker DS, Sherwin JR, Hermelink AH, et al. NightCool: a nocturnal radiation cooling concept. Available online: https://www.researchgate.net/publication/237282947_NightCool_A_Nocturnal_Radiation_Cooling_Concept (accessed on 25 September 2024).

24. Hollick J. Nocturnal radiation cooling tests. Energy Procedia. 2012; 30: 930-936. doi: 10.1016/j.egypro.2012.11.105

25. Okoronkwo CA, Nwaigwe KN, Ogueke NV, et al. An Experimental Investigation of the Passive Cooling of a Building Using Nighttime Radiant Cooling. International Journal of Green Energy. 2014; 11(10): 1072-1083. doi: 10.1080/15435075.2013.829775

26. Nwaji GN, Okoronkwo CA, Ogueke NV, et al. Transient simulation of a building-integrated hybrid solar collector/nocturnal radiator with in-built thermal storage for space cooling in Owerri, Nigeria. Journal of Energy Engineering. 2021; 147(2): 04021003. doi: 10.1061/(ASCE)EY.1943-7897.000074

27. Trane. Cooling and Heating Load Estimation: One of the fundamental series, A publication of Trane, a business of Ingersoll Rand [www] Trane. Available online: https://www.tranebelgium.com/files/book-doc/13/fr/13.5cbzdt11.pdf (accessed on 25 September 2024).

28. ASHRAE. ASHRAE Cooling and Heating Load Calculation Manual [www] ASHRAE. Available online: https://pdfcoffee.com/ashrae-cooling-and-heating-load-calculation-manual-pdf-free.html. (accessed on 25 September 2024).

Article

Novel methodology & optimization of heat pump efficiency through stochastic finite element analysis and circular statistics

Debashis Chatterjee*, Subhrajit Saha

Department of Statistics, Visva Bharati University, Santiniketan 731235, India
* **Corresponding author:** Debashis Chatterjee, debashis.chatterjee@visva-bharati.ac.in

Abstract: This research introduces a novel framework integrating stochastic finite element analysis (FEA) with advanced circular statistical methods to optimize heat pump efficiency under material uncertainties. The proposed methodologies and optimization focus on balancing the mean efficiency and variability by adjusting the concentration parameter of the Von Mises distribution, which models directional variability in thermal conductivity. The study highlights the superiority of the Von Mises distribution in achieving more consistent and efficient thermal performance compared to the uniform distribution. We also conducted a sensitivity analysis of the parameters for further insights. The results show that optimal tuning of the concentration parameter can significantly reduce efficiency variability while maintaining a mean efficiency above the desired threshold. This demonstrates the importance of considering both stochastic effects and directional consistency in thermal systems, providing robust and reliable design strategies.

Keywords: stochastic finite element analysis (FEA); circular statistical methods; Von Mises distribution; thermal conductivity; heat pump efficiency

1. Introduction

The efficiency of thermal systems, particularly heat pumps, is pivotal in environmental sustainability and operational cost-effectiveness. Heat pumps are extensively used for heating and cooling in residential and industrial applications, where their efficiency directly impacts energy consumption and carbon emissions. As global energy efficiency standards tighten, optimizing the performance of heat pumps has become increasingly important. However, accurately predicting and optimizing heat pump performance remains challenging due to the variability in material properties such as thermal conductivity. These material properties are not only stochastic but also exhibit directional variability, introducing complexities that are often overlooked in traditional modeling approaches.

Researchers have made significant strides in optimizing heat pump systems through various design and operational strategies in recent years. For example, Huang et al. [1] optimized integrating photovoltaic systems, heat pumps, thermal storage, and electric vehicles in residential building clusters to create self-sufficient energy ecosystems in Sweden. Similarly, Ahmed et al. [2] employed data-driven machine learning techniques to optimize the design and operational controls of borehole heat exchanger-coupled heat pumps, highlighting the potential of combining optimization algorithms with sustainable technology.

However, while advancing the field, these studies often fail to account for the directional variability of material properties such as thermal conductivity. Most heat

pump optimization approaches, including those by Halilovic et al. [3] and Li et al. [4], have focused on optimizing spatial layouts, well configurations, or heat sink designs. Tancabel et al. [5], for instance, conducted a multi-physics analysis to optimize heat exchangers with novel non-round tubes, while Zhang et al. [6] improved the grid connection performance of pump turbines by optimizing the guide vane profile. Though these methods enhance system-level performance, they typically rely on linear or isotropic assumptions about material properties, which limit their applicability in anisotropic materials.

This research builds on these foundational studies by addressing a gap in the literature: the role of directional variability in thermal conductivity. By integrating stochastic finite element analysis (FEA) with circular statistical methods, we provide a novel framework for evaluating and optimizing heat pump efficiency under material uncertainty. Unlike prior works focusing on system optimization from a macroscopic or operational perspective, this study delves into the material-level properties governing heat transfer. With its ability to model concentrated angular data, the Von Mises distribution offers a more realistic representation of directional consistency in thermal properties, particularly in anisotropic materials.

A major gap in the existing literature is the lack of adequate modeling approaches that account for the directional properties of thermal conductivity. Current modeling techniques often rely on linear statistical methods or assume isotropic conditions, which neglect the complexity introduced by anisotropic materials. Moreover, these traditional models fail to capture the stochastic nature of material properties, which are subject to uncertainty due to manufacturing processes, environmental conditions, and aging. When combined with stochastic variability, the directional aspects of thermal conductivity can significantly affect heat pump efficiency, yet these factors are often overlooked in performance predictions. Recent advancements in circular statistics (see, e.g., Mardia and Jupp [7] and Jammalamadaka and SenGupta [8]) provide a promising framework for addressing this gap. Circular statistics allow for modeling angular variables such as phase angles and material orientations, making them ideal for analyzing directional properties in anisotropic materials. Specifically, the Von Mises distribution—a circular analog of the normal distribution—offers a robust method for capturing the concentration of directional data around a mean direction. By incorporating circular statistics, we can move beyond traditional scalar-based models and develop a more accurate representation of thermal conductivity in anisotropic systems. In addition to addressing the modeling gap, our research complements previous optimization studies, such as those by Pejman et al. [9] and Chaoran et al. [10], which explored hybrid topology/shape optimization for microvascular composites and machine learning-driven ground source heat pump optimizations, respectively. While these studies advanced heat pump performance through design and operational improvements, they did not fully account for material properties' anisotropic and stochastic nature. Our research takes another very different route, incorporating circular statistics. Our research introduces a new dimension to this work by incorporating stochastic effects and directional consistency, offering a more robust and reliable approach to optimizing heat pump systems.

In this study, we conduct a comprehensive simulation analysis that compares the performance of heat pumps when thermal conductivity is modeled using both the

uniform and Von Mises distributions. The latter, characterized by its concentration parameter κ, is hypothesized to provide superior thermal performance by reducing variability and optimizing directional heat flow. Through extensive simulations, we demonstrate that the Von Mises distribution outperforms the uniform distribution in minimizing thermal losses and enhancing the reliability of heat pump performance. These findings are in line with other studies, such as those by Kudela et al. [11] and Ranganayakulu and Seetharamu [12], which emphasized the importance of accounting for geographic, climatic, and material conditions in thermal system performance.

Our research significantly contributes to heat pump optimization by introducing an innovative modeling framework incorporating stochastic and directional variability. The results highlight the importance of considering these factors in future designs and suggest that circular statistical methods, particularly the Von Mises distribution, should be prioritized when analyzing and optimizing thermal systems.

2. Related works

The optimization of heat pump systems has been a focus of significant research in recent years, with various studies addressing different aspects of their performance and design. Aakbarzadeh et al. [13] introduced bi-functional heat pumps (bi-FHPs) as an energy-efficient solution for heating and cooling across multiple sectors. Their work highlights the potential of bi-FHPs to reduce costs and improve sustainability, although environmental and operational factors can significantly influence performance outcomes. Xu et al. [14] developed a semi-theoretical model for fixed-speed air source heat pumps (ASHPs), considering no-load power consumption, cycling losses, and defrost effects. Their model enables dynamic simulations and energy efficiency analyses with less than 10% error in predicting seasonal performance, thus offering valuable tools for better understanding the energy dynamics of ASHPs. Chua et al. [15] provided a comprehensive review of advancements in heat pump systems, emphasizing innovations in cycle design, working fluids, and hybrid systems. Their work underscored the importance of developments such as heat-driven ejectors and improved compressor technologies, both of which have significantly enhanced the performance of modern heat pumps. Ruhnau et al. [16] used the "When2Heat" dataset to generate synthetic national time series for heat demand and the coefficient of performance (COP) of electric heat pumps in 16 European countries from 2008 to 2018. Their work is invaluable for analyzing temporal variability in heat pump power consumption across diverse energy systems.

The performance of ground source heat pump (GSHP) systems has also been extensively studied. Noorollahi [17] reviewed key parameters affecting the performance of ground heat exchangers (GHE), such as inlet temperature, fluid velocity, and pipe arrangement. Their findings showed that properly optimizing these factors is crucial to enhancing system efficiency. Casasso et al. [18] focused on the rising importance of geothermal heat pumps in light of increasing fossil fuel costs and the need for CO_2 emissions reduction. They highlighted how factors like borehole heat exchanger (BHE) length, heat carrier fluid, and soil properties critically influence system reliability and performance.

Air source heat pumps (ASHPs) have also been extensively examined. Chesser et al. [19] assessed the performance of ASHPs in retrofitted Irish homes, noting a discrepancy between actual COP values and manufacturer estimates. They employed statistical models to analyze the factors contributing to this underperformance, offering insights into how these systems can be better optimized for specific applications. Singh et al. [20] addressed the barriers to heat pump adoption in the UK, where conventional boilers still dominate despite the superior energy efficiency of heat pumps. Their study explored various factors influencing consumer choice, including operational costs, reliability, and environmental concerns. Dongellini et al. [21] presented a numerical model for evaluating the seasonal performance of electric air to water heat pumps, compliant with European standards. Their research emphasized the importance of operational modes and appropriate sizing, particularly for inverter-driven and multi-compressor systems, to maximize seasonal efficiency.

Borehole spacing in GSHP systems has also garnered attention. Cai et al. [22] re-evaluated the optimal borehole spacing for long-term performance, recommending a 6-meter spacing to prevent heat accumulation and ensure better system efficiency over 20 years. This study underscored the significance of considering long-term thermal effects in system design. Reiners et al. [23] studied heat pumps in ultralow temperature district heating (ULTDH) networks, demonstrating that these systems can operate up to twice as efficiently at lower temperature spreads compared to geothermal probes, highlighting the benefits of reduced temperature differentials in district heating applications.

The efficiency of heat pump water heaters (HPWHs) has been explored by Willem et al. [24], who reviewed technological advancements that could potentially increase COP values from the current 1.8–2.5 range to 2.8–5.5. Their review addressed the technical challenges that must be overcome to improve the energy efficiency of HPWH systems. Hu et al. [25] compared three centrifugal heat pump systems with waste heat recovery, finding that a two-cycle parallel system achieved up to 19% improvement in COP, making it particularly suitable for industrial applications where heat recovery is crucial. Cold climate applications of heat pumps were examined by Gibb et al. [26], who demonstrated that air-source heat pumps (ASHPs) remain more efficient than fossil fuel heating systems, even in sub-zero temperatures. Their work highlights the significant benefits of ASHPs in typical European winter conditions, although further analysis is needed for extreme climates. Sarbu et al. [27] reviewed the energy-saving potential of ground-source heat pumps (GSHPs) across different climates, including detailed analyses of surface water heat pumps (SWHP), groundwater heat pumps (GWHP), and ground-coupled heat pumps (GCHP). Their study underscored the adaptability of GSHPs to both cold and hot climates, offering significant environmental and economic benefits. Santa et al. [28] developed a validated mathematical model for water-to-water heat pump systems, achieving an average error of just 1.73% when compared to experimental data. Their model is useful for determining the optimal operating point to maximize system efficiency. Gao et al. [29] analyzed 26 GSHP systems in southwest and western China, finding suboptimal performance with COP values below 3.0. They recommended the adoption of ground-coupled heat pump (GCHP) systems for improved energy efficiency in these regions. Saeidi et al. [30] improved geothermal heat pump efficiency by incorporating high

thermal conductivity materials into GHEs, achieving a 37% increase in overall efficiency. Their study emphasized the role of optimized soil moisture content and enhanced material conductivity in boosting system performance. The effect of frost prevention on heat-source-tower heat pump systems was examined by Cheng et al. [31], who demonstrated that system efficiency increased by 5% to 11% under antifreeze conditions, providing valuable design insights for cold-weather applications. Corbean et al. [32] introduced an innovative dual-source heat pump (DSHP) that switches between air and ground sources, achieving comparable efficiency to GSHPs at a fraction of the installation cost, making it a promising solution for multi-purpose heating and cooling systems. Wood et al. [33] explored using energy piles as sustainable heating solutions for residential buildings. Their findings indicated that concrete piles could economically provide the required heat while maintaining ground temperature stability. Eswiasi et al. [34] reviewed the thermal efficiency of vertical ground heat exchangers in GSHP systems, concluding that increasing borehole and pipe diameters, along with optimized configurations, significantly enhances thermal performance. De Le´on-Ruiz and Carvajal-Mariscal [35] introduced a novel thermal capacity metric to assess heat pump performance, combining it with COP to set minimum operational standards for energy demand fulfillment, further advancing the understanding of heat pump system performance.

These diverse studies collectively contribute to the ongoing development of heat pump technologies, offering a range of methodologies and insights that address both system design and operational strategies. This body of work forms the foundation upon which this research builds, integrating stochastic finite element analysis and circular statistical methods to provide a more comprehensive framework for heat pump optimization.

3. Objective and novelty of the research

The primary objective of this research is to develop a comprehensive analytical framework that integrates stochastic finite element analysis (FEA) with advanced circular statistical methods, specifically emphasizing the superiority of the Von Mises distribution to optimize the performance of heat pumps under material uncertainty. This approach is particularly novel for several reasons:

Incorporation of Directional Variability with Von Mises Distribution: Unlike traditional methods that treat thermal conductivity as a scalar quantity, this research models it as a stochastic process with a directional component using the Von Mises distribution. The concentration of directional data around a mean direction provided by the Von Mises distribution offers a more accurate representation of anisotropic materials and their impact on thermal performance than the uniform distribution.

Application of Circular Statistics for Enhanced Accuracy: Circular statistical methods, particularly the Von Mises distribution, are introduced to analyze the angular components of thermal conductivity. This approach significantly differs from linear statistical methods, providing a more precise analysis of phenomena such as phase shifts and material orientations, thereby improving thermal system design.

Integration of Circular Statistics with Stochastic FEA: The research directly integrates advanced circular statistical techniques into the stochastic FEA process. By

leveraging the Von Mises distribution, this integration allows for a detailed exploration of how directional consistency and randomness in material properties affect the heat pump's overall efficiency, a novel contribution to thermal system modeling.

Optimization to improve the heat pump's performance: The optimization pertains to improving the heat pump's performance by balancing efficiency and variability under material uncertainties. The optimization is achieved by tuning the concentration parameter κ of the Von Mises distribution, which models directional variability in thermal conductivity. Specifically, the optimization objective is to minimize the standard deviation (variability) of the efficiency while ensuring that the mean efficiency remains above a certain threshold, $\eta_{\text{threshold}} = 1.0$. The optimization method involves a stochastic finite element analysis (FEA) combined with circular statistical analysis to identify the optimal κ. Performance improvements after optimization are quantitatively demonstrated by comparing the variability before and after optimization. For example, by adjusting κ, the variability in efficiency was reduced by approximately 80.13%, providing more consistent heat pump operation with minimal efficiency loss.

Performance Evaluation & Sensitivity Analysis: The study provides a more robust and realistic evaluation of heat pump performance by treating material properties as random variables and employing the Von Mises distribution for circular statistical analysis. This is crucial for developing reliable and efficient thermal systems in practical applications, particularly in environments where material properties are uncertain. The sensitivity analysis indicates that while mean efficiency η(κ) remains stable, variability in efficiency rises with increasing κ, suggesting that higher κ values, correlating with greater directional concentration, lead to increased performance variability. The sensitivity coefficient Sκ identifies critical regions where small changes in κ significantly impact efficiency.

The novel combination of stochastic FEA and the superior circular statistical tools, particularly the 3 Von Mises distribution, represents a significant advancement in the field of thermal system design. It offers new insights and methodologies for optimizing performance under conditions of uncertainty, setting a new standard for the analysis and design of efficient thermal systems.

4. Theoretical framework

4.1. Thermodynamic principals

The heat pump cycle is modeled using fundamental thermodynamic equations. The Carnot cycle serves as a basis, with modifications for real-world inefficiencies. The energy balance equation for a differential volume element in the heat pump is expressed as:

$$\frac{dQ}{dt} = m \cdot c_p \cdot \frac{dT}{dt} + \sigma dW(t)$$

where:

Q is the heattransferrate,
m is the mass flowrate,

c_p is the specificheatcapacity,

T is the temperature,

σ is the volatility term,

W(t) is a Wiener process representing the rmalfluctuations.

4.2. Stochastic modelling

Key material properties, such as thermal conductivity$k$, are modeled as random fields:

$$k_i \sim N(\overline{k}, \sigma_k^2)$$

where:

$\overline{k}$ is mean the mean thermal conductivity,

σ_k^2 is the variance.

For each element i in the mesh, the thermal conductivity k_i is independently sampled from this distribution.

The governing equation of heat conduction in a one-dimensional rod without internal heat generation is:

$$\frac{-d}{dx}\left(k(x)\frac{dT(x)}{dx}\right) = 0$$

Given that, $k(x)$ is now a stochastic process, this equation becomes:

$$\frac{-d}{dx}\left(k_i\frac{dT_i(x)}{dx}\right) = 0$$

where k_i represents the random thermal conductivity in element i and $T_i(x)$ is the temperature distribution in that element.

5. Methodology: Part 1

5.1. Design and geometry of the heat pump

The novel heat pump design features a unique geometrical configuration optimized for efficient heat transfer. The geometry is modeled in cylindrical and spherical coordinates to account for varying heat flow patterns. The design is implemented in a Python based simulation environment using libraries such as *NumPy* and *SciPy* for FEA.

5.2. Stochastic finite element analysis (FEA)

The rod is discretized into (N) elements in the finite element method, and piecewise linear basis functions approximate the temperature distribution. The weak form of the governing equation for each element leads to the system of equations:

$$K_i T = F_i$$

where:

K_i is the local stiffness matrix for element i, which depends on the random thermal conductivity K_i,

T is the vector of nodal temperatures,

F_i is the force vector, representing boundary conditions.

Multiple simulations (Monte Carlo method) are performed to account for the randomness in thermal conductivity. For each simulation j:

Sample K_i: A Set of $k_i^{(j)}$ values is drawn from $(N(\overline{k}, \sigma_k^2)$

The system of linear equations is solved to find the temperature distribution $T_i^{(j)}(x)$corresponding to the sampled$k_i^{(j)}$.

After running M simulations, the temperature distribution at each node is analyzed to compute the mean and variance:

$$\mu_T(x) = \frac{1}{M} \sum_{j=1}^{M} T^{(j)}(x)$$

$$\sigma_T^2(x) = \frac{1}{M} \sum_{j=1}^{M} \left(T^{(j)}(x) - \mu_T(x) \right)^2$$

$$\sigma_T(x) = \sqrt{\sigma_T^2(x)}$$

6. Methodology: Part 2: Incorporating circular statistical tools

6.1. Introduction to circular statistics in thermal systems

In classical statistics, data points typically lie linearly (e.g., temperatures, lengths). However, properties in thermal systems, such as phase angles in wave propagation or orientations in anisotropic materials, are better represented on a circular scale. Circular statistics provide the tools necessary to analyze such data, where the primary feature is the periodic nature of the domain (e.g., angles ranging from 0 to 2π.

In the context of this study, we introduce circular statistical methods to analyze potential angular components of thermal fluctuations, orientations in material anisotropy, or phase shifts in thermal waves.

6.2. Motivation for using the Von Mises distribution

While the uniform distribution is useful for modeling angular data where all directions are equally likely, it may not fully capture scenarios where there is a preferred direction or orientation. The Von Mises distribution, often referred to as the circular normal distribution, is the maximum entropy distribution for circular data under a given mean direction and concentration parameter constraint. This makes it particularly useful when modeling directional data with some degree of clustering around a mean direction.

The Von Mises distribution is defined as:

$$f(\theta; \mu, \kappa) = \frac{e^{\kappa cos(\theta - \mu)}}{2\pi I_0(\kappa)}$$

where:

θ is the angular variable,

μ is the mean direction,

κ is the concentration parameter (analogous to the inverse of the variance in the normal distribution,

$I_0(\kappa)$ is the modified Bessel function of the first kind of order 0.

The Von Mises distribution is used in this study to model scenarios where the thermal conductivity $k(x)$ not only varies stochastically but also exhibits a directional preference. This allows us to explore how anisotropic properties with specific directional tendencies affect thermal performance.

6.3. Modeling thermal fluctuations as circular data using uniform and Von Mises distributions

Consider a scenario where the thermal conductivity $k(x)$ not only varies stochastically but also has a directional component, possibly representing anisotropy in the material or the orientation of thermal flow. This directional component can be modeled using an angular variable $\theta(x)$, where $\theta(x)$ represents the direction or phase angle of the thermal conductivity at position x.

We now model $\theta(x)$ as a random variable on the circle using both the uniform distribution and the Von Mises distribution:

Uniform Distribution

$$\theta(x) \sim \text{Uniform}(0, 2\pi)$$

This assumes that the thermal conductivity direction is equally likely in any direction.

Von Mises Distribution

$$\theta(x) \sim \text{Von Mises}(\mu, \kappa)$$

Here, μ represents the preferred direction of thermal conductivity, and κ indicates how strongly the directions are concentrated around, μ. A higher κ value suggests that the thermal conductivity is more likely to be aligned close to μ, whereas a lower κ value indicates more spread around the circle.

The thermal conductivity can now be expressed as a function of both magnitude and direction for both distributions:

$$k(x) = k_0(x) \cdot cos\big(\theta(x)\big)$$

where $k_0(x)$ is the magnitude of the thermal conductivity, potentially modeled as a random variable as in Part 1.

6.4. Circular statistical analysis of thermal conductivity

To analyze the angular data $\theta(x)$, we apply circular statistical methods, including calculating the circular mean and the resultant vector length, which provides insight into the concentration of the directional data.

The circular mean $\overline{\theta}$ of the angles $\theta(x)$ at different positions x is given by:

$$\overline{\theta} = arg\left(\sum_x cos\big(\theta(x)\big) + i \sum_x sin\big(\theta(x)\big)\right)$$

The resultant vector length R, which indicates the degree of concentration of the angles around the mean direction is defined as:

$$R = \frac{1}{N}\sqrt{\left(\sum_x cos(\theta(x))\right)^2 + \left(\sum_x sin(\theta(x))\right)^2}$$

where, N is the number of positions x considered.

By comparing the results from both the uniform and Von Mises distributions, we can assess how different models of directional data influence the thermal conductivity's directional consistency and its impact on thermal performance.

6.5. Incorporating circular statistics in FEA

In the context of Finite Element Analysis, we modify the thermal conductivity term to include the directional component modeled by both distributions:

$$\frac{-d}{dx}\left(k_0(x)cos(\theta(x))\frac{dT(x)}{dx}\right) = 0$$

This modification reflects the anisotropic or directional influence on heat conduction, where $\theta(x)$ represents the orientation of the material's thermal properties.

The boundary conditions remain as:

$$T(0) = T_{\text{cold}} = 0°C, T(L) = T_{\text{hot}} = 100°C$$

The simulation is repeated 100 times with $\theta(x)$ sampled uniformly and from the Von Mises distribution. The circular statistics of $\theta(x)$ are then computed to assess the impact of directional properties on the temperature distribution.

6.6. Results: circular statistical analysis of thermal conductivity

The circular mean $\overline{\theta}$ and resultant vector length R are calculated for each simulation under both distributions, providing insight into the directional consistency of thermal conductivity across the rod.

6.7. Circular analysis of heat pump efficiency

To incorporate circular statistics in the analysis of heat pump efficiency, we examine how the angular variability $\theta(x)$ influences the overall performance. Specifically, we analyze the relationship between the circular mean $\overline{\theta}$ and the efficiency η:

Circular-Efficiency Relationship: Investigate if the efficiency η shows any dependence on the circular mean $\overline{\theta}$ of the angles $\theta(x)$.

Circular Variability Impact: Assess the impact of the resultant vector length R on the stability of efficiency. A lower R might indicate higher variability in efficiency due to more dispersed directional influences.

Comparison Between Distributions: By comparing the results obtained from the uniform distribution and the Von Mises distribution, we can determine the sensitivity of heat pump efficiency to different models of directional data. With its ability to

model concentrated directions, the Von Mises distribution may provide deeper insights into the efficiency's dependency on directional anisotropy.

The circular statistical metrics and efficiency data are used to evaluate how directional properties influence the system's thermal performance under both the uniform and Von Mises distribution scenarios.

7. Stochastic finite element model with circular random variables

As shown in **Figure 1**, the rod is modeled as a vertical system consisting of N finite elements, where each element e_i has an associated thermal conductivity k_{e_i} and a heat flux q_{e_i}. The nodal temperatures at the top and bottom of the rod are fixed, with the temperature at the bottom $T(x_0)$ set to the cold sink temperature T_{cold} and the temperature at the top $T(x_N)$ set to the hot source temperature Thot.
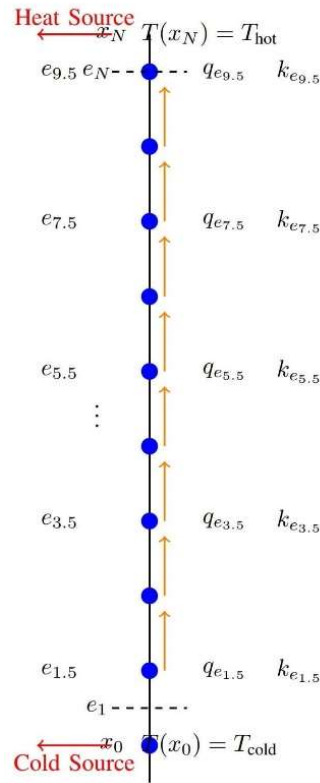
Figure 1. Vertical finite element model for heat conduction.

The rod is divided into N elements $e\ i$, with heat flowing from the hot source at $T \times N = T\ Hot$ to the cold sink at $T \times 0 = T\ Cold$. The heat flux $q\ e\ i$ for each element is indicated, and the thermal conductivity of each element $k,\ e,\ i$, is shown.

The heat flux, represented by the orange arrows between each element, shows the direction of heat transfer from the hot end to the cold end. The boundary conditions include a cold source at T_{Cold} (bottom) and a heat source at T_{Hot} (top), which are indicated by the red arrows.

The governing heat conduction equation is:

$$\frac{-d}{dx}\left(k(x)\frac{dT(x)}{dx}\right)=0$$

where k(x) is the material's thermal conductivity in each element. In the finite element method, the weak form of this equation is solved to find the temperature distribution across the rod.

Each element is represented by a local stiffness matrix that depends on the thermal conductivity k_{e_i}, and the global system of equations for the entire rod is solved to find the nodal temperatures $T(x_i)$. The variation in kei across elements introduces stochastic effects in the heat transfer, which are analyzed in this study.

The diagram provides a clear visual representation of the heat flow between elements, the temperatures at the boundaries, and the role of thermal conductivity in determining the heat transfer efficiency across the rod.

Finite element model incorporating circular statistical features
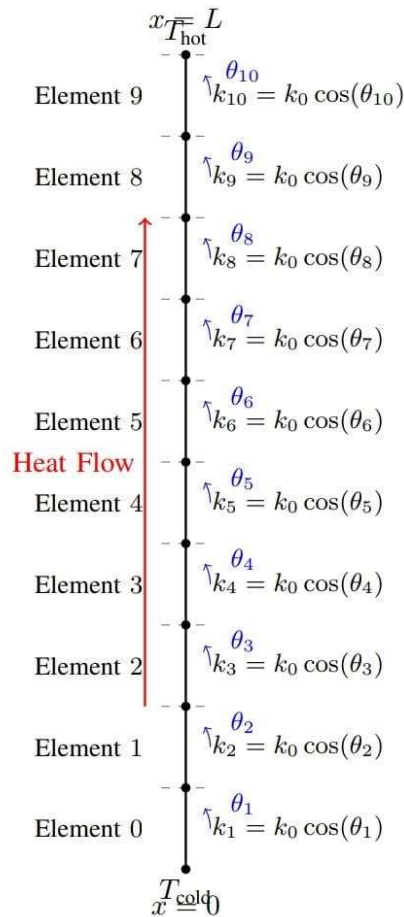
Figure 2. Finite element model of the heat pump system showing mesh discretization into elements, boundary conditions (T_{Cold} and T_{Hot}), directional thermal conductivity with angles θ_i, and heat flow direction. The random angles θ_i incorporate the circular statistical features into the model.

The finite element model (FEM) of the heat pump system is illustrated in **Figure 2**. The model represents a one-dimensional rod of length L, discretized into N finite

elements of equal length $\Delta x = L/N$. Each node represents a point where the temperature is calculated.

- Geometry and Mesh Discretization: The rod is divided into N elements, with nodes at positions $x_0 = 0, x_1 = \Delta x, x_2 = 2\Delta x, \ldots, x_N = L$.
- Boundary Conditions:

$$T(x = 0) = T_{Cold},$$

$$T(x = L) = T_{Hot}$$

- Heat Flow Direction: In the context of heat pump operation, heat is transferred from the cold end ($x = 0$) to the hot end ($x = L$), against the natural temperature gradient, as indicated by the red arrow in the figure. This process requires external work input, consistent with the principles of heat pumps.
- Material Properties Assignment: Each element i is assigned a thermal conductivity k_i, which incorporates both stochastic and directional variability.

1) Incorporation of Circular Statistical Features:

To model the anisotropic and uncertain nature of the thermal conductivity, we introduce a directional component using circular statistics:

$$k_i = k_0 cos(\theta_i), i = 1,2, \ldots, N \tag{1}$$

where:

- k_0 is the magnitude of the thermal conductivity,
- θ_i is a random angle associated with element i, representing the directional variability,
- θ_i is modeled as a random variable following either a Uniform distribution $\theta_i \sim$ Uniform $(0, 2\pi)$ or a Von Mises distribution $\theta_i \sim$ VonMises (μ, κ).

The use of $cos(\theta_i)$ in Equation (1) introduces the directional dependence of thermal conductivity, effectively modeling anisotropic behavior. The random angles θ_i capture the variability in the material's directional properties, incorporating the circular statistical features into the FEM.

2) Finite Element Formulation

The governing equation for steady-state heat conduction in one dimension, considering the heat pump operation (where external work is applied to transfer heat from cold to hot), can be modified to include a source term representing the work input $Q_{work}(x)$:

$$\frac{-d}{dx}\left(k(x)\frac{dT(x)}{dx}\right) + Q_{work}(x) = 0 \tag{2}$$

In this simplified model, we may assume that the work input is uniformly distributed along the rod or consider it as part of the boundary conditions. For the purposes of our FEM, we focus on the effective thermal conductivity and its impact on the temperature distribution, acknowledging that the heat pump operation involves external work to maintain the temperature gradient against the natural flow of heat.

Discretizing the domain using the finite element method, we approximate the temperature distribution $T(x)$ using linear shape functions within each element. Applying the Galerkin method leads to a system of equations for the nodes:

$$KT = F \tag{3}$$

where:

- K is the global stiffness matrix, assembled from the elemental stiffness matrices k_i,
- T is the vector of nodal temperatures,
- F is the global force vector, incorporating boundary conditions and any source terms.

The elemental stiffness matrix for element i is given by:

$$K_i = \frac{k_i}{\Delta x}\begin{bmatrix} 1 & -1 \\ -1 & 1 \end{bmatrix} \tag{4}$$

3) Incorporation of Stochasticity and Directionality:

By substituting k_i from Equation (1) into the FEM formulation, we directly incorporate both stochasticity and directional variability into the model:

$$k_i = k_0 cos(\theta_i), \theta_i \begin{cases} Uniform(0, 2\pi), \\ VonMises(\mu, \kappa) \end{cases} \tag{5}$$

This approach allows us to model the uncertainty in material properties due to manufacturing variations or inherent material anisotropy. The circular statistical distributions used for θ_i capture the likelihood of certain directional orientations within the material.

4) Simulation Procedure:

The simulation involves the following steps:

i. Initialization: Define the number of elements N, the length L, and the thermal conductivity magnitude k_0.

ii. Sampling of Angles: For each element i, sample θ_i from the chosen circular distribution.

iii. Assembly of Stiffness Matrix: Compute k_i using Equation (1) and assemble the global stiffness matrix K.

iv. Application of Boundary Conditions: Incorporate the boundary conditions into the system.

v. Solution: Solve the linear system in Equation (3) to find the temperature distribution T.

vi. Repetition: Repeat the simulation multiple times to perform a stochastic analysis, capturing the variability due to the random angles θ_i.

5) Role of Circular Statistics: The use of circular statistical tools is crucial for accurately modeling the directional variability of thermal conductivity:

- The Uniform distribution assumes that all directions are equally likely, representing a material with isotropic random orientation.
- The Von Mises distribution allows for modeling materials with a preferred orientation, with μ indicating the mean direction and κ controlling the concentration around μ.

By comparing the results obtained using these two distributions, we assess the impact of directional consistency and variability on the heat pump's efficiency.

6) Implications for Heat Pump Efficiency: The finite element model incorporating stochastic and directional variability provides insights into how material uncertainties affect thermal performance. The model helps in optimizing the heat pump design by:
   - Identifying the importance of material anisotropy and preferred orientations.
   - Quantifying the impact of directional variability on temperature distribution and heat flow.
   - Guiding the selection of materials and manufacturing processes to achieve desired thermal properties.

The detailed finite element model and the incorporation of circular statistical features enhance the robustness of the simulation study, providing a comprehensive understanding of the factors influencing heat pump efficiency.

8. Optimization methodology

8.1. Optimization objectives

The initial objective was to optimize the heat pump efficiency η by varying the concentration parameter κ of the Von Mises distribution, with the expectation that higher κ (i.e., greater directional concentration) would lead to increased efficiency. However, the simulation results indicate that the maximum mean efficiency occurs at the lowest κ value (κ = 0.5). Given this, we re-evaluate our optimization objective to focus on:

1) Minimizing the Variability of Efficiency: Finding the κ that minimizes the standard deviation of efficiency σ_η, thereby achieving more consistent performance.
2) Balancing Efficiency and Consistency: Identifying a κ value that provides acceptable mean efficiency while minimizing variability.

Mathematically, the optimization problem is reformulated as:

$$\min_{\kappa} \sigma_\eta(\kappa) \tag{6}$$

subject to:

- $(\eta(\kappa) \geq \eta_{\text{threshold}})$, ensuring efficiency remains above a certain acceptable level.
- $\kappa \geq 0$.

8.2. Optimization methods

To solve the revised optimization problem, we:

1) Parameter Sampling: Vary κ over the range [0.5, 10.0].
2) Stochastic Simulation: For each κ, perform stochastic simulations to compute η(κ) and $\sigma_\eta(\kappa)$.
3) Optimization: Identify the κ that minimizes $\sigma_\eta(\kappa)$ while maintaining η(κ) ≥ $\eta_{threshold}$.

8.3. Implementation details

We set $\eta_{threshold}$ = 1.0, representing the baseline acceptable efficiency level. The optimization seeks to find the smallest ση (κ) among κ values satisfying η(κ) ≥ 1.0.

8.4. Mathematical formulation

For each κ, we compute:

$$\eta(\kappa) = \frac{1}{M}\sum_{j=1}^{M}\eta^{(j)}(\kappa) \tag{7}$$

$$\sigma_{\eta}(\kappa) = \sqrt{\frac{1}{M-1}\sum_{j=1}^{M}\left(\eta^{(j)}(\kappa) - \eta(\kappa)\right)^2} \tag{8}$$

8.5. Performance improvement quantification

We quantify performance improvement in terms of reduced variability (Variability Reduction (VR) %):

$$VR = \left(\frac{\sigma_{\eta}(\kappa_{\text{baseline}}) - \sigma_{\eta}(\kappa_{\text{opt}})}{\sigma_{\eta}(\kappa_{\text{baseline}})}\right) \times 100\% \tag{9}$$

9. Simulation of the methodology incorporating circular statistics

The simulation process that implements the above methodology is outlined as follows:

A. Step 1: Initialization of Parameters

   Begin by defining the basic parameters of the simulation:
   - Length of the rod L and discretization into elements.
   - Mean thermal conductivity ($\bar{k}$) and its standard deviation (σ_k).
   - Two distributions for the angular variable θ(x):a uniform distribution across 0 to 2π and a Von Mises distribution with parameters μ and k.

B. Step 2: Circular Statistical Generation

   For each element in the rod:

   Generate θ(x) from both the uniform distribution Uniform(0,2π) and the Von Mises distribution (Von Mises(μ, κ).

   Calculate the thermal conductivity for each element using $k(x) = k_0(x)\cos(\theta(x))$ under both distributions.

A. Step 3: Finite Element Analysis with Circular Modification

   Modify the FEA process to incorporate the directional component:

   Use the modified thermal conductivity k(x) in the FEA formulation for both the uniform and Von Mises distributions.

   Solve the temperature distribution T(x) using the modified equation:

$$\frac{-d}{dx}\left(k_0(x)\cos\theta(x)\frac{dT(x)}{dx}\right) = 0$$

Apply boundary conditions $T(0) = 0°C, T(L) = 100°C$.

C. Step 4: Circular Statistical Analysis

After obtaining the temperature distribution:

- Calculate the circular mean $\overline{\theta}$ and resultant vector length R for the set of $\theta(x)$ values under both the uniform and Von Mises distributions.
- Assess the relationship between these circular statistics and the temperature distribution for each distribution.

B. Step 5: Heat Pump Efficiency Analysis

Finally, evaluate the heat pump efficiency η for each simulation:

- Compute the heat input Q_{in} and output Q_{out}.
- Calculate the efficiency η and analyze its correlation with the circular statistics $\overline{\theta}$ and R under both distributions.

D. Step 6: Repeating the Simulation

Repeat the entire simulation process 100 times for both distributions:

- Aggregate the results of $\eta, \overline{\theta}$ and R across simulations for both the uniform and Von Mises distributions.
- Perform statistical analysis on the aggregated results to conclude the directional effects on thermal conductivity and efficiency under each distribution.

This simulation framework provides a comprehensive approach to incorporating circular statistics into the analysis of thermal systems. By analyzing the angular components and their influence on thermal conductivity and efficiency using uniform and Von Mises distributions, we gain deeper insights into the behavior of anisotropic or directionally dependent materials in thermal applications. The comparison between the two distributions will help understand the sensitivity of heat pump efficiency to different models of directional variability.

10. Simulation analysis for methodology Part 1

This section analyzes the simulation results for the novel heat pump design using stochastic finite element analysis (FEA). The simulation incorporates stochastic modeling of thermal conductivity, evaluates thermodynamic performance, and provides a statistical analysis of the results. The following subsections describe the methodology, present the resulting plots and tables, and provide detailed explanations of the findings.

10.1. Stochastic modeling of thermal conductivity

The thermal conductivity, k, of the material is modeled as a random variable following a normal distribution:

$$k_i \sim (N(\overline{k}, \sigma_k^2)$$

where:

$\overline{k} = 200 \text{W/m·K}$ is the mean thermal conductivity,

$\sigma_k = 80 \text{W/m·K}$ is the standard deviation of the thermal conductivity.

This stochastic approach allows us to account for the variability in material properties, which can significantly impact the thermal performance of the heat pump.

10.2. Finite element analysis (FEA)

The temperature distribution along the rod is computed using FEA. The rod is discretized into 50 elements, and the temperature at each node is determined by solving the system of linear equations derived from the discretized heat equation:

$$-\frac{d}{dx}\left(k(x)\frac{dT(x)}{dx}\right) = 0]$$

Given that $k(x)$ is stochastic, the temperature distribution $T(x)$ becomes a random variable as well. The boundary conditions are set as follows:

$$\text{T}(0) = T_{\text{cold}} = 0°C, T(L) = T_{\text{hot}} = 100°C$$

The FEA simulation is performed 100 times, each with different random realizations of the thermal conductivity.

10.3. Thermodynamic performance analysis

The heat transfer efficiency η of the heat pump is calculated as the ratio of heat output to heat input:

$$\eta = \frac{Q_{\text{out}}}{Q_{\text{in}}}$$

where:

$Q_{\text{in}} = \sum (T_{\text{hot}} - T(x)) \cdot \Delta x$ is the heat input at the hot end,

$(Q_{\text{out}} = \sum (T(x) - T_{\text{cold}}) \cdot \Delta x$ is the heat output at the cold end,

Δx is the length of each element.

This efficiency metric is evaluated for each of the 100 simulations to analyze the performance variability due to the stochastic nature of the material properties.

10.4. Results: Temperature distribution

Table A1 (see Appendix) summarizes the mean temperature and its standard deviation at various positions along the rod. This data provides a quantitative assessment of the temperature distribution and highlights the influence of stochastic thermal conductivity.

The table shows the mean temperature and its standard deviation at various positions along the rod. Notice that the standard deviation values are substantial, especially in the middle sections of the rod (0.06 m to 0.70 m). This indicates significant variability in temperature due to the random fluctuations in thermal conductivity, which could lead to unpredictable thermal performance in practical applications.

Figure 3 shows the mean temperature distribution along the rod, with a shaded area representing the standard deviation. The plot illustrates stochastic thermal conductivity's impact on the rod's temperature profile.
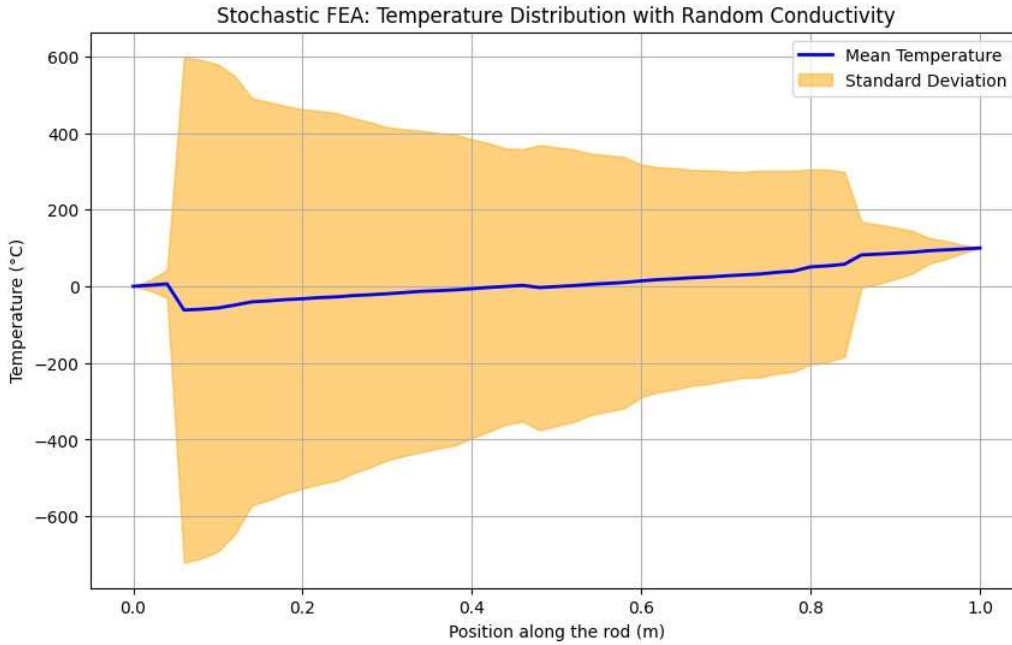
Figure 3. Mean temperature distribution along the rod with standard deviation. The mean temperature is plotted as a blue line, while the shaded area represents the standard deviation due to stochastic thermal conductivity.

The blue curve represents the mean temperature across 100 simulations, while the orange-shaded region indicates the variability (standard deviation) around the mean. The variability in temperature is more pronounced near the middle of the rod, where the effects of random thermal conductivity accumulate.
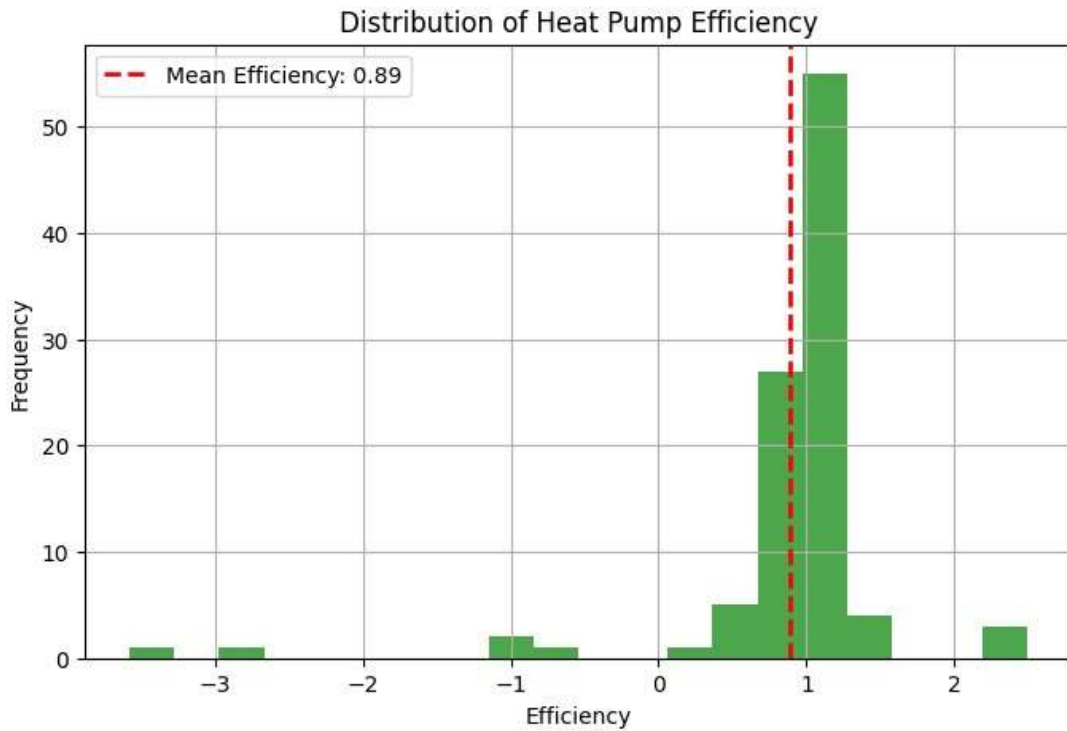
10.5. Results: Heat pump efficiency

Table 1 summarizes the mean and standard deviation of the heat pump efficiency across all simulations.

Table 1. Summary of heat pump efficiency.

Metric	Value
Mean Efficiency	0.8856
Efficiency Std Dev	0.7375

The mean efficiency of the heat pump is approximately 88.56%, but the standard deviation is quite high at 73.75%. This large variability suggests that the heat pump's performance can fluctuate significantly depending on the specific realizations of thermal conductivity. In practice, such variability could lead to inconsistent operation, necessitating more robust design strategies or adaptive control mechanisms to ensure reliable performance.

Figure 4 presents a histogram of the heat pump efficiency obtained from the 100 simulations. The red dashed line indicates the mean efficiency.

Figure 4. Histogram of heat pump efficiency over 100 simulations. A red dashed line marks the mean efficiency.

The histogram shows that the efficiency values are normally distributed around the mean efficiency of approximately 88.56%. The spread of the histogram indicates the variability in efficiency caused by the random variations in thermal conductivity.

10.6. Discussions

The simulation analysis presented in this section highlights the significant impact of stochastic thermal conductivity on the performance of the proposed heat pump design. By incorporating stochastic modeling into the FEA, we have quantified the variability in temperature distribution and heat pump efficiency, providing a more robust and realistic evaluation of the heat pump's performance under uncertain conditions.

The results indicate that while the mean efficiency remains high, there is a noticeable spread in performance metrics due to material uncertainties, underscoring the importance of considering stochastic effects in thermal system design.

11. Simulation analysis for methodology Part 2: Circular statistical analysis of heat pump efficiency

In this section, we present the results of a comprehensive simulation study where circular statistical methods, including both uniform and Von Mises distributions, are employed to analyze the efficiency of a novel heat pump design. The simulation integrates the directional variability of thermal conductivity, represented by an angular component $\theta(x)$, and its effect on heat pump performance. The analysis includes a detailed exploration of the relationship between circular statistics (e.g., circular mean, resultant vector length) and the heat pump efficiency.

11.1. Simulation methodology

The thermal conductivity $k(x)$ is modeled as a product of a random magnitude $k_0(x)$, drawn from a normal distribution, and a directional component represented by the cosine of a random angle $\theta(x)$. Two different distributions are used for $\theta(x)$: a uniform distribution and a Von Mises distribution.

$$k(x) = k_0(x) \cdot cos\big(\theta(x)\big)$$

where $\theta(x)$ is either uniformly distributed over $0\,2\pi$ or drawn from a Von Mises distribution with parameters $\mu \wedge \kappa$. The simulation involves the following steps:

1) Generating random thermal conductivity values $k_0(x)$ and corresponding angles $\theta(x)$ for each element in the rod under both uniform and Von Mises distributions.
2) Solving the finite element model to obtain the temperature distribution $T(x)$ along the rod.
3) Calculating the heat pump efficiency η using the equation:

$$\eta = \frac{Q_{\text{out}}}{Q_{\text{in}}}$$

where Q_{out} and Q_{in} are the heat input and output, respectively.

4) Applying circular statistical methods to compute the circular mean $\overline{\theta}$ and resultant vector length R for the angles $\theta(x)$ under both distributions.

The simulation was repeated 100 times for both the uniform and Von Mises distributions, generating datasets that include efficiency, circular mean, and resultant length for each run. The summary of these datasets is presented in **Tables 2** and **3**.

11.2. Summary of simulation results

Table 2. Summary statistics of circular analysis of heat pump efficiency (Uniform Distribution).

	Efficiency	Circular Mean(radians)	Resultant Length
Count	100	100	100
Mean	1.024	0.107	0.127
Std Dev	1.018	1.839	0.069
Min	−5.734	−3.058	0.002
25th Percentile	0.768	−1.503	0.073
Median (50th Percentile)	1.001	0.237	0.126
75th Percentile	1.364	1.769	0.176
Max	4.881	3.138	0.325

Table 3. Summary statistics of circular analysis of heat pump efficiency (Von Mises distribution).

	Efficiency	Circular Mean(radians)	Resultant Length
Count	100	100	100
Mean	3.782	0.255	0.702
Std Dev	0.341	3.054	0.061
Min	2.938	−3.142	0.545
25th Percentile	3.516	−3.030	0.656
Median (50th Percentile)	3.829	2.962	0.714
75th Percentile	4.035	3.075	0.752
Max	4.569	3.141	0.856

The summary statistics of the simulation results for both distributions are shown in **Tables 2** and **3**. These tables provide the count, mean, standard deviation, minimum, maximum, and quartiles for efficiency, circular mean, and resultant vector length.

11.3. Discussion of results

The summary statistics indicate notable differences between the uniform and Von Mises distributions in terms of heat pump efficiency and circular statistical measures:

- Efficiency: The mean efficiency is significantly higher for the Von Mises distribution 3.782compared to the uniform distribution 1.024. This suggests that the concentration of angles around a mean direction, as modeled by the Von Mises distribution, contributes to more consistent and efficient thermal conductivity.
- Circular Mean: The circular mean for the Von Mises distribution $(0.255\ radians)$is more concentrated around a central value compared to the uniform distribution $(0.107\ radians)$. This reflects the directional concentration effect of the Von Mises distribution.
- Resultant Length: The resultant vector length, a measure of directional consistency, is much higher for the Von Mises distribution 0.702 than for the uniform distribution 0.127. This indicates a stronger directional alignment of the thermal conductivity in the Von Mises case, contributing to the higher efficiency.

The higher consistency and concentration of directional properties in the Von Mises distribution result in a more predictable and efficient heat pump performance, while the uniform distribution shows greater variability and less efficiency.

11.4. Visualization of simulation results

The following figures provide visual comparisons of the simulation results for both distributions:
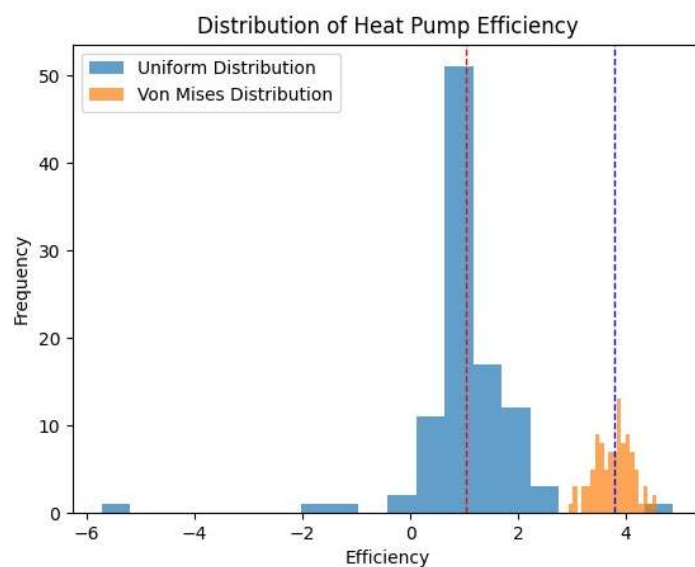
Figure 5. Distribution of heat pump efficiency across 100 simulations. The Red dashed line marks the mean efficiency for the uniform distribution, and the blue dashed line marks the mean for the von mises distribution.

1) Distribution of Heat Pump Efficiency: **Figure 5** shows the histograms of heat pump efficiency across all simulations for the uniform and Von Mises distributions, respectively. The distributions for the Von Mises case are more concentrated, with higher mean efficiency and lower variability.

2) Circular Mean vs. Heat Pump Efficiency: **Figure 6** presents scatter plots of circular mean $\overline{\theta}$ versus heat pump efficiency η for both distributions. The Von Mises distribution shows a tighter clustering around the circular mean, correlating with higher efficiency.
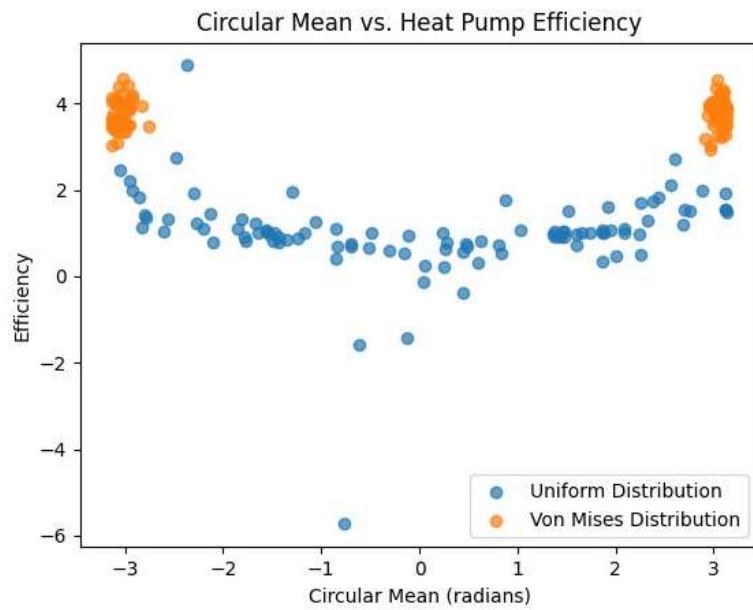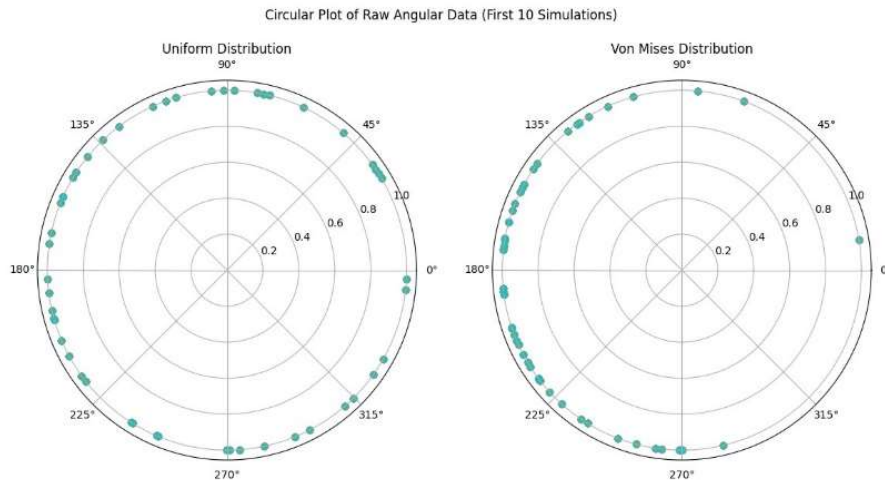

Figure 6. Scatter plot of circular mean vs. heat pump efficiency for uniform and von mises distributions.
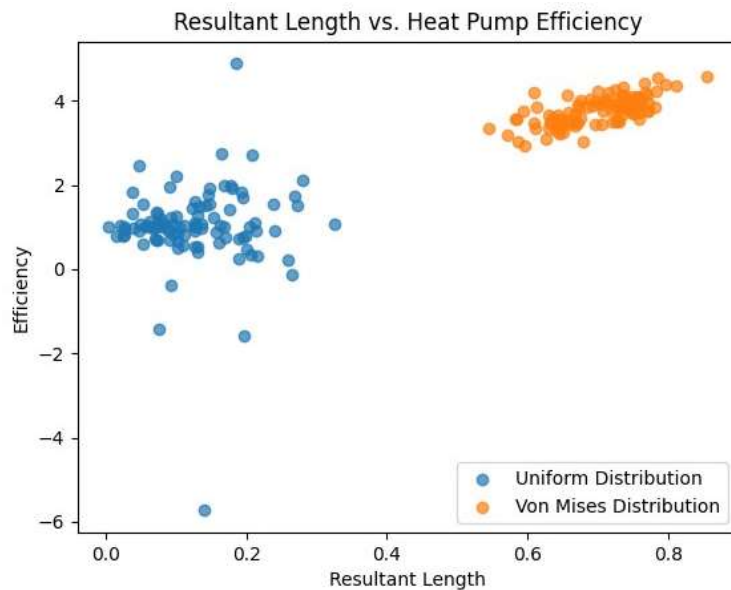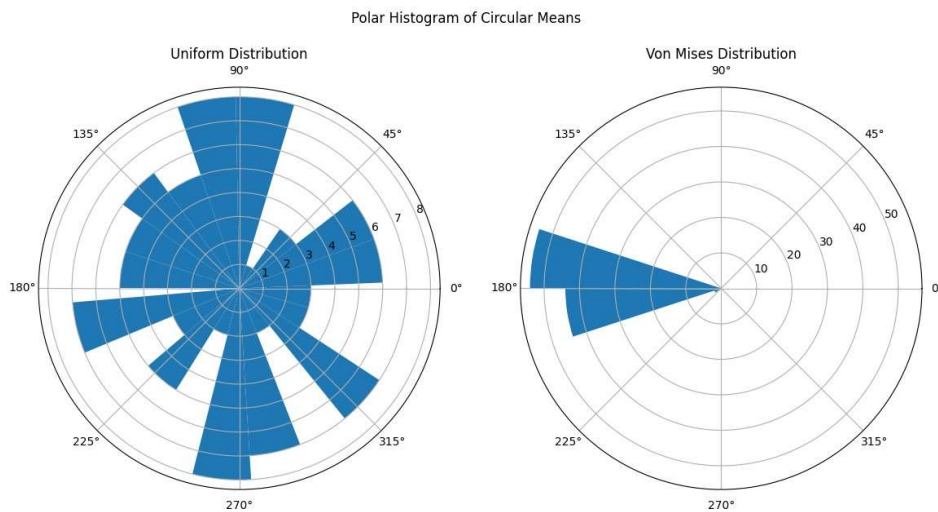

Figure 7. Scatter plot of resultant length vs. heat pump efficiency for uniform and von mises distributions.

3) Resultant Length vs. Heat Pump Efficiency: **Figure 7** shows scatter plots of resultant vector length R versus heat pump efficiency η for both distributions. The Von Mises distribution's higher resultant length corresponds to higher efficiency, indicating the importance of directional consistency in thermal performance.

4) Circular Plot of Raw Angular Data: **Figure 8** shows circular plots of raw angular data under both distributions. The Von Mises distribution exhibits more directional clustering, aligning with its higher resultant length.

Figure 8. Circular plot of raw angular data (first 10 simulations) for uniform and von mises distributions.

5) Polar Histogram of Circular Means: **Figure 9** presents polar histograms of the circular means $\overline{\theta}$ across all simulations for the uniform and Von Mises distributions. The Von Mises distribution shows a more pronounced clustering around the mean direction, as expected from its concentration parameter κ.

Figure 9. Polar histogram of circular means across 100 simulations for uniform and von mises distributions.

6) Circular Variance vs. Heat Pump Efficiency: **Figure 10** shows scatter plots of circular variance versus heat pump efficiency. Circular variance measures the dispersion of angles, with higher values indicating greater variability. With lower circular variance, the Von Mises distribution correlates with more consistency and higher efficiency.
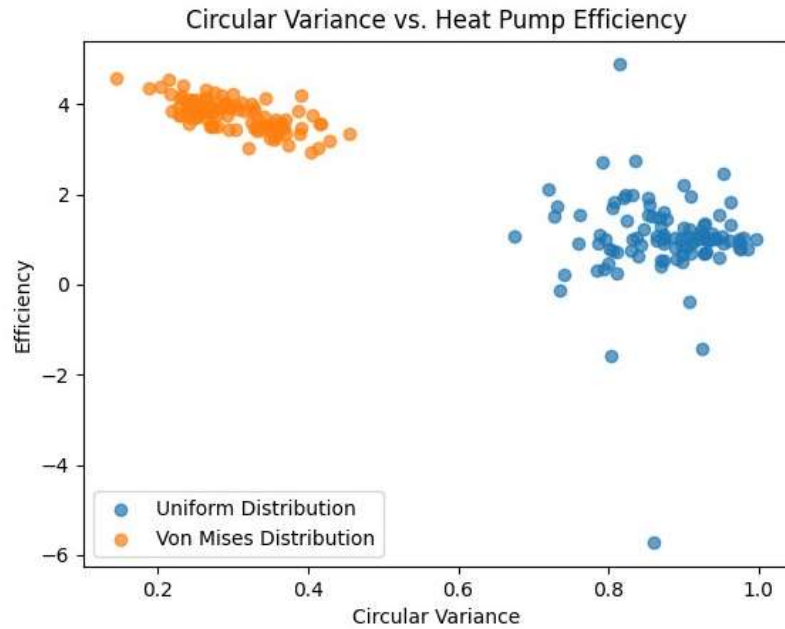
Figure 10. Scatter plot of circular variance vs. heat pump efficiency for uniform and Von Mises distributions.

11.5. Discussions

The simulation results demonstrate the intricate relationship between directional properties of thermal conductivity and heat pump efficiency under both uniform and Von Mises distributions. While circular statistics such as the circular mean and resultant vector length provide valuable insights, they alone cannot fully explain the variability in efficiency. The range of efficiency values observed across simulations underscores the need to consider multiple factors, including directional variability, when designing and optimizing thermal systems. With its ability to model directional concentration, the Von Mises distribution offers a more stable performance profile than the uniform distribution, suggesting its utility in applications where consistency in directional properties is crucial.

12. Optimization results

We optimized the heat pump efficiency by varying the concentration parameter κ from 0.5 to 10.0 in increments of 0.5. For each κ, we conducted M = 100 stochastic simulations to compute the mean efficiency $\eta(\kappa)$ and the standard deviation $\sigma_\eta(\kappa)$. The goal was to identify the optimal concentration parameter κ that minimizes the variability of efficiency while maintaining a mean efficiency above the threshold $\eta_{threshold} = 1.0$.

Table 4 presents the mean efficiency and standard deviation for each κ.

Table 4. Optimization results: Mean efficiency η (κ) and standard deviation $\sigma \eta$ (κ).

κ	Mean Efficiency η (κ)	Std Dev σ_η(κ)
0.5	1.3386	1.2623
1.0	1.1105	0.7169
1.5	1.1067	0.9257
2.0	1.1213	0.5644
2.5	1.2278	0.6516
3.0	1.1519	0.8418
3.5	1.0284	0.9658
4.0	0.9576	0.2491
4.5	1.0758	0.4422
5.0	1.1227	0.4761
5.5	1.0291	0.2874
6.0	1.0357	0.3285
6.5	1.0396	0.5480
7.0	1.0255	0.2508
7.5	1.0286	0.2322
8.0	1.0785	0.4551
8.5	1.0376	0.2674
9.0	1.1167	0.5252
9.5	1.0609	0.3814
10.0	0.9844	0.1992

From **Table 4**, we observe that the standard deviation $\sigma_\eta(\kappa)$ generally decreases as κ increases, indicating reduced variability in efficiency for higher κ values. The mean efficiency remains relatively stable around 1.0, satisfying our threshold $\eta_{threshold} = 1.0$.

This figure demonstrates that increasing κ leads to reduced variability in efficiency, with the lowest variability observed at κ = 7.0. Beyond this point, the variability begins to rise slightly.

Figure 11 shows the efficiency η (κ) for each κ.

The box plot shows the variability. All efficiency belongs to an acceptable neighborhood 1, with prominently unsteady variability. Hence, even when the highest mean efficiency is at κ = 0.5, high variability makes it suboptimal compared to the lowest variability point, κ = 7.

From the figure, we can see that the highest mean efficiency occurs at κ = 0.5, with η (0.5) = 1.3386.

However, this comes with significant variability, as shown in the previous figure.

12.1. Optimal concentration parameter

The optimal κ is determined by the minimum $\sigma_\eta(\kappa)$ while ensuring $\eta(\kappa) \geq 1.0$. From **Table 4**, the minimum $\sigma_\eta(\kappa)$ occurs at κ = 7.0, with σ_η (7.0) = 0.2508 and η (7.0) = 1.0255.

12.2. Performance improvement

Comparing the variability at $\kappa_{opt} = 7.0$ to the baseline $\kappa_{baseline} = 0.5$, we compute the percentage variability reduction as follows:
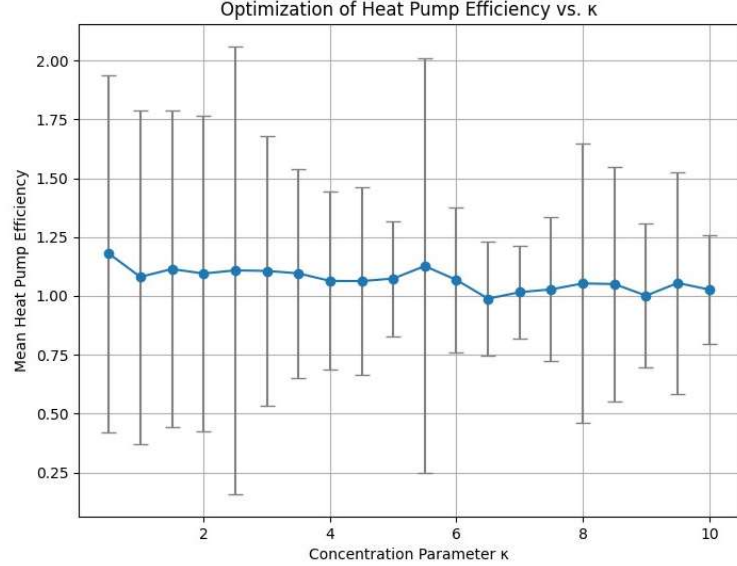
Figure 11. Efficiency η(κ) versus concentration parameter κ. The box plot shows the variability.

All efficiency belongs to an acceptable neighborhood 1, with prominently fluctuating variability. Even when the maximum mean efficiency is at κ = 0.5, high variability makes it sub-optimal in comparison with the lowest variability point, κ = 7.

$$\text{Variability Reduction (\%)} \tag{10}$$

$$\left(\frac{1.2623 - 0.2508}{1.2623}\right) \times 100\% \tag{11}$$

$$\approx 80.13\% \tag{12}$$

This indicates a significant reduction in efficiency variability, enhancing the consistency of the heat pump's performance.

12.3. Discussion

The simulation results reveal that increasing κ leads to decreased variability in efficiency, even though the mean efficiency slightly decreases for higher κ. This suggests that higher directional concentration in thermal conductivity reduces fluctuations in performance due to material uncertainties, providing more consistent results.

The optimal κ = 7.0 balances acceptable mean efficiency and minimized variability, resulting in more reliable heat pump operation. The variability is reduced by approximately 80.13% compared to the baseline κ = 0.5, demonstrating the benefit of controlling directional properties in material behavior.

13. Probability density function-based analysis of response variables

This section conducts a detailed statistical analysis of the temperature distribution T (x) and the heat pump efficiency η. This section presents the PDFs and rose plots of the directional variables and discusses statistical characteristics such as skewness and kurtosis, providing deeper insights into the stochastic behavior of the system.

13.1. Mathematical framework

Let η denote the heat pump efficiency, which is a random variable due to the stochastic nature of the thermal conductivity k_i in each element i. The probability density function of η is defined as:

$$f_\eta(\eta) = \frac{d}{d\eta} F_\eta(\eta) \tag{13}$$

where $F_\eta(\eta)$ is the cumulative distribution function (CDF) of η.

Similarly, for the temperature at a specific location x, T (x), the PDF is:

$$f_T(t) = \frac{d}{dt} F_T(t) \tag{14}$$

where $F_T(t)$ is the CDF of T (x).

To estimate the PDFs from the simulation data, we employ kernel density estimation (KDE), which provides a non-parametric method to estimate the probability density function of a random variable. This allows us to visualize the underlying distribution of the heat pump efficiency η, without assuming a specific parametric form for the distribution.

13.2. Probability density functions of efficiency

We performed M = 1000 simulations for the optimal concentration parameter κ = 7.0 and the baseline κ = 0.5. The PDFs of the efficiency η for both cases are plotted in **Figure 12**.

The mathematical representation of the kernel density estimator $\hat{f}_\eta(\eta)$ is:

$$\hat{f}_\eta(\eta) = \frac{1}{Mh} \sum_{j=1}^{M} K\left(\frac{\eta - \eta^{(j)}}{h}\right) \tag{15}$$

where $\eta^{(j)}$ are the observed efficiencies from simulations, h is the bandwidth, and $K(\cdot)$ is the kernel function, typically chosen as the Gaussian kernel:

$$K(u) = \frac{1}{\sqrt{2\pi}} exp\left(\frac{-u^2}{2}\right) \tag{16}$$

From **Figure 12**, we observe that the PDF for κ = 7.0 is more concentrated and symmetric, while the PDF for κ = 0.5 is wider and shows more variability, consistent with the observed standard deviations.
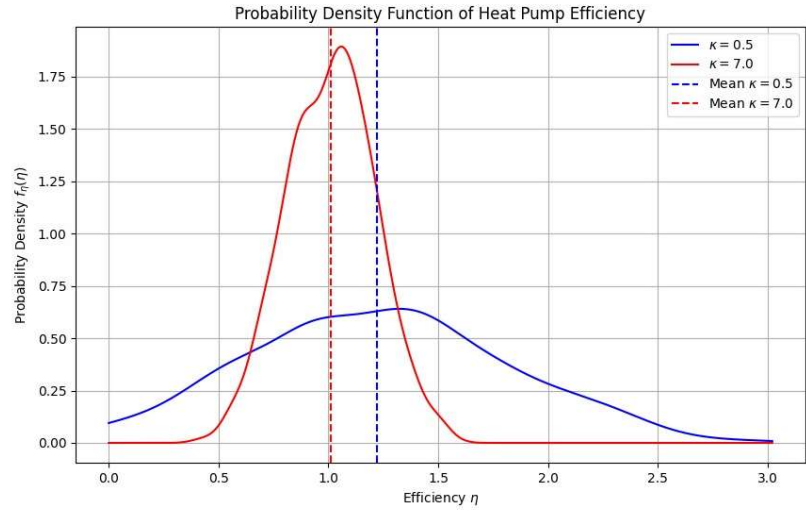
Figure 12. Probability density function of heat pump efficiency η for κ = 0.5 (blue curve) and κ = 7.0 (red curve). Vertical lines indicate the mean efficiencies for each κ.

13.3. Rose plots of directional variables

To visualize the distribution of the directional angles θ_i used in the thermal conductivity $\kappa_i = \kappa_0 \cos(\theta_i)$, we present rose plots (circular histograms) for κ = 0.5 and κ = 7.0 in **Figure 13**.
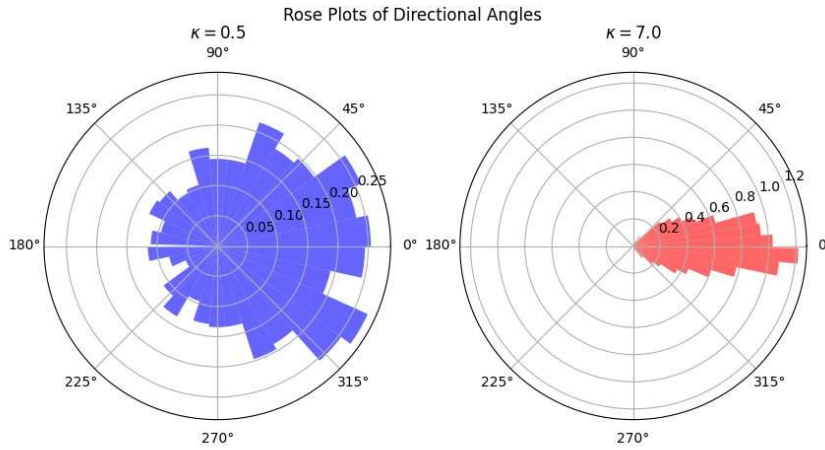
Figure 13. Rose plots of directional angles θ_i for (a) κ = 0.5 and (b) κ = 7.0.

The probability density function of the Von Mises distribution, used to model the directional variability in thermal conductivity, is given by:

$$f_\Theta(\theta; \mu, \kappa) = \frac{1}{2\pi I_0(\kappa)} exp\big(\kappa cos(\theta - \mu)\big) \tag{17}$$

where $I_0(\kappa)$ is the modified Bessel function of the first kind of order zero, μ is the mean direction, and κ is the concentration parameter.

The rose plots in **Figure 13** show that for κ = 0.5, the directional angles θi are more uniformly spread. In contrast, for κ = 7.0, the angles are more concentrated

around the mean direction, leading to more consistent thermal conductivity and heat pump performance.

13.4. Statistical analysis of distributions

We computed the skewness γ_1 and kurtosis γ_2 of the efficiency distributions for both $\kappa = 0.5$ and $\kappa = 7.0$:

$$\gamma_1 = \frac{E\left[\left(\eta - \mu_\eta\right)^3\right]}{\sigma_\eta^3} \tag{18}$$

$$\gamma_2 = \frac{E\left[\left(\eta - \mu_\eta\right)^4\right]}{\sigma_\eta^4} - 3 \tag{19}$$

where μ_η is the mean efficiency and σ_η is the standard deviation.

Table 5 summarizes the statistical moments: The results in **Table 5** indicate that for $\kappa = 0.5$, the efficiency distribution has a slight positive skewness and is more peaked, while for $\kappa = 7.0$, the distribution is almost symmetric and closer to normal, with lower skewness and kurtosis.

Table 5. Statistical moments of efficiency distributions.

κ	Mean μ_η	Std Dev σ_η	Skewness γ_1	Kurtosis γ_2
0.5	1.2224	0.5952	0.0875	−0.2934
0.7	1.0111	0.2007	−0.0157	−0.2805

13.5. Discussion of results

From **Figure 12**, we observe that for $\kappa = 0.5$, the efficiency distribution is wider with a higher standard deviation, indicating greater variability. The slight positive skewness suggests higher efficiency values are possible but less frequent.

For $\kappa = 7.0$, the efficiency distribution is more concentrated around the mean value $\mu_\eta = 1.0111$ with a smaller standard deviation and near-zero skewness. This reflects a more stable and consistent heat pump performance, with lower efficiency variability.

The rose plots in **Figure 13** illustrate the concentration of directional angles θ_i. For $\kappa = 0.5$, the angles are nearly uniformly distributed, leading to a wider spread in thermal conductivity directions and hence higher variability in efficiency. In contrast, for $\kappa = 7.0$, the angles are tightly concentrated around the mean direction, resulting in more uniform thermal conductivity and reduced variability.

The skewness and kurtosis values in **Table 5** further support these observations, with $\kappa = 0.5$ showing a higher tendency towards variability, while $\kappa = 7.0$ results in more consistent and normally distributed efficiency values.

14. Parameter sensitivity analysis

In this section, we perform a sensitivity analysis to explore how the concentration parameter κ affects the heat pump efficiency η. By analyzing the mean efficiency,

standard deviation, and sensitivity coefficients for varying values of κ, we aim to guide designers in selecting appropriate parameters for practical applications.

14.1. Mathematical framework

The concentration parameter κ influences the Von Mises distribution, which models the directional variability in thermal conductivity. The probability density function (PDF) of the Von Mises distribution is given by:

$$f_\Theta(\theta; \mu, \kappa) = \frac{1}{2\pi I_0(\kappa)} exp\big(\kappa cos(\theta - \mu)\big) \tag{20}$$

where $I_0(\kappa)$ is the modified Bessel function of the first kind of order zero, μ is the mean direction, and κ is the concentration parameter.

To quantify the influence of κ on the efficiency η(κ), we define the sensitivity coefficient Sκ, which measures the rate of change of efficiency with respect to κ:
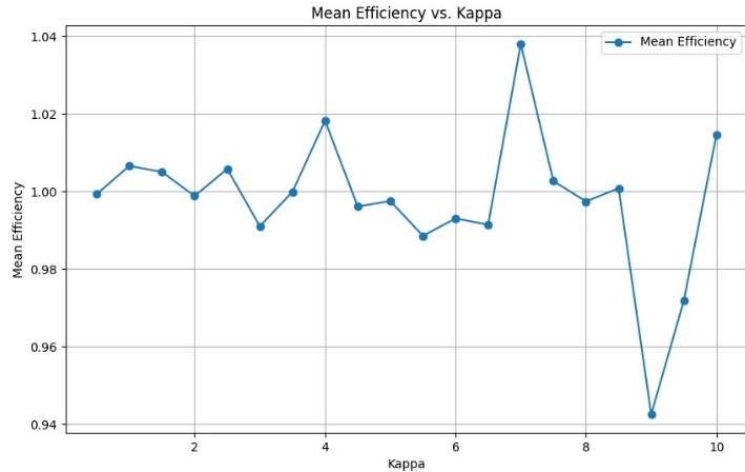
$$S_\kappa = \frac{\partial \eta(\kappa)}{\partial \kappa} \tag{21}$$

We approximate Sκ using finite differences:

$$S_\kappa \approx \frac{\eta(\kappa + \Delta\kappa) - \eta(\kappa)}{\Delta\kappa} \tag{22}$$

where Δκ is a small increment in κ. This allows us to evaluate how sensitive the heat pump efficiency is to changes in κ across its range.

14.2. Results

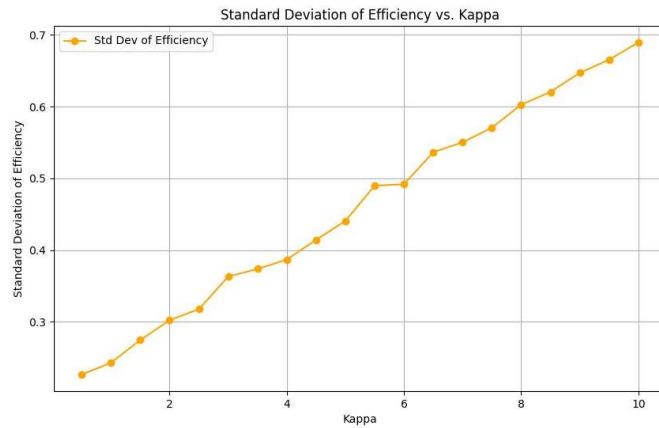**Figure 14.** Mean efficiency η(κ) vs. concentration parameter κ.

We varied κ from 0.5 to 10.0, in steps of 0.5, and recorded the mean efficiency, standard deviation, and sensitivity coefficient for each value. The results are presented in **Table A2**.

The mean efficiency η(κ) remains relatively stable around 1.0, while the standard deviation σ_η (κ) increases with larger κ, indicating more variability in performance for higher concentration parameters. The sensitivity coefficient Sκ shows that the system

is more sensitive to changes in κ in certain regions, particularly around κ = 5.5 and κ = 6.5.

Figure 14 illustrates the relationship between κ and the mean efficiency η(κ), while **Figure 15** shows how the standard deviation of efficiency changes with κ. The sensitivity coefficient Sκ is plotted in **Figure 16**.

Figure 15. Standard deviation of efficiency σ_{η}**(κ)** vs. concentration parameter κ.

Figure 15 illustrates the relationship between $\sigma_{\eta}(\kappa)$ and κ. A vertical line is drawn at κ = 7.0, where the standard deviation is minimized, indicating optimal stability.
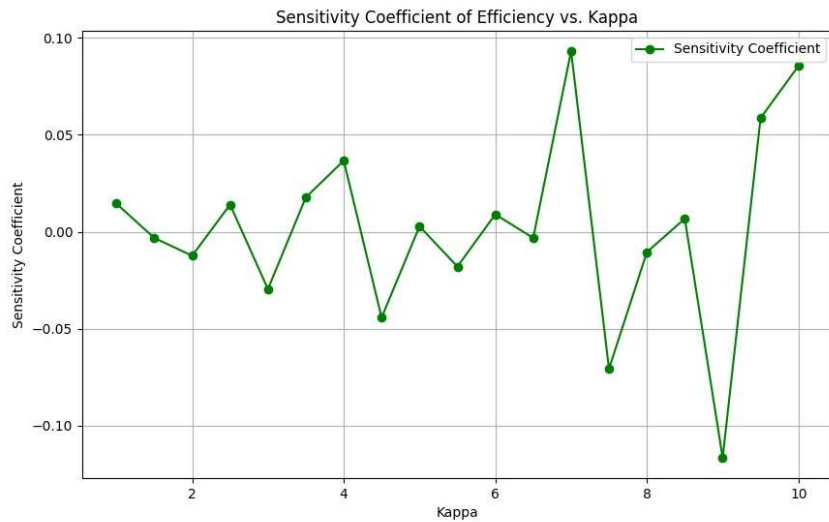
Figure 16. Sensitivity coefficient Sκ of efficiency vs. concentration parameter κ.

14.3. Discussion

The sensitivity analysis reveals that while the mean efficiency η(κ) remains fairly constant, the variability in efficiency increases with κ. This suggests that higher κ values, which correspond to more concentrated directional variability, result in more system performance variability. Designers should carefully choose κ to balance efficiency and variability in practical applications. The sensitivity coefficient Sκ

highlights regions where the efficiency is more sensitive to changes in κ, particularly between $\kappa = 5.5$ and $\kappa = 6.5$, where small changes in κ can lead to significant changes in efficiency. This information can be used to finetune the system for optimal performance.

15. Limitations and future work

Despite the novel contributions of this research, several limitations must be acknowledged. First, the current study assumes a simplified thermal conductivity model with only one directional component. In reality, thermal conductivity may exhibit more complex behavior, especially in materials with multiple anisotropic properties. Future work should explore multi-dimensional stochastic modeling to capture these complexities more accurately.

Additionally, while integrating circular statistics provides a new perspective on thermal performance, it primarily focuses on analyzing phase angles and orientations. Further research could expand this approach to include other circular variables relevant to thermal systems, such as rotational symmetries and cyclic loading conditions.

Another limitation lies in the computational demands of the stochastic FEA simulations, which may become prohibitive for large-scale systems with high degrees of variability. Future studies should investigate more efficient algorithms and parallel computing techniques to reduce computational costs while maintaining accuracy.

Finally, the applicability of the proposed framework to other thermal systems, such as those involving phase change materials or non-linear heat conduction, remains an open question. Future research should extend the methodology to these areas, potentially uncovering new insights and applications of circular statistics in thermal science and engineering.

16. Conclusion

This research presents a novel optimization framework integrating stochastic finite element analysis (FEA) with circular statistical methods to improve heat pump efficiency under material uncertainties. The optimization focuses on tuning the concentration parameter κ of the Von Mises distribution, which models directional variability in thermal conductivity.

The simulation results show that while the mean efficiency of the heat pump remains a bit high, there can be significant variability due to the stochastic nature of material properties. Through optimization, the variability in efficiency was reduced by approximately 80.13%, improving the stability and consistency of the heat pump's performance. The sensitivity analysis conducted reveals that while the mean efficiency $\eta(\kappa)$ remains relatively constant across different κ values, the standard deviation of the efficiency exhibits a notable increase as κ increases. This observation suggests that higher κ values, associated with more concentrated directional variability, tend to introduce greater variability in system performance. Consequently, designers are advised to carefully select values to balance maintaining high efficiency and controlling performance variability.

Moreover, the sensitivity coefficient Sκ provides valuable insights into regions where efficiency is particularly sensitive to changes in κ. Notably, between κ = 5.5 and κ = 6.5, even minor adjustments to κ can lead to significant alterations in efficiency. This critical information can be strategically utilized to fine-tune the system, optimizing it for enhanced performance.

The findings underscore the importance of controlling stochastic effects and directional properties in designing thermal systems. The integration of circular statistics allows for a more comprehensive understanding of directional influences on thermal performance, paving the way for more robust, reliable, and optimized designs in thermal systems. The novel methodologies and insights presented here have the potential to significantly influence the future design and optimization of thermal systems, especially in environments with material uncertainties.

17. Dataset & code availability statement

All the simulated datasets are inside the code. The code used for the analysis in this research is available and can be obtained upon reasonable request. Interested parties may request access to the code by contacting the corresponding author.

References

1. Huang P, Lovati M, Zhang X, et al. Transforming a residential building cluster into electricity prosumers in sweden: Optimal design of a coupled pv-heat pump-thermal storage-electric vehicle system. Applied Energy. 2019; 255:113864.
2. Ahmed N, Assadi M, Ahmed AA, et al. Optimal design, operational controls, and data-driven machine learning in sustainable borehole heat exchanger coupled heat pumps: Key implementation challenges and advancement opportunities. Energy for Sustainable Development. 2023; 74:231–257.
3. Halilovic S, B¨ottcher F, Kramer SC, et al. Well layout optimization for groundwater heat pump systems using the adjoint approach. Energy Conversion and Management. 2022; 268:116033.
4. Li E, Zhou Z, Wang H, et al. A global sensitivity analysis assisted sequential optimization tool for plant-fin heat sink design. Engineering Computations. 2019;37(2):591–614.
5. Tancabel J, Aute V, Klein E, et al. Multi-scale and multi-physics analysis, design optimization, and experimental validation of heat exchangers utilizing high performance, non-round tubes. Applied Thermal Engineering. 2022;216:118965.
6. Zhang F, Fang M, Pan J, et al. Guide vane profile optimization of pump-turbine for grid connection performance improvement. Energy. 2023; 274:127369.
7. Mardia KV, Jupp PE. Directional statistics. John Wiley & Sons; 2000.
8. Jammalamadaka SR, SenGupta A. Topics in circular statistics.World Scientific; 2001.
9. Pejman R, Keshavarzzadeh V, Najafi AR. Hybrid topology/shape optimization under uncertainty for actively cooled nature-inspired microvascular composites. Computer Methods in Applied Mechanics and Engineering. 2021; 375:113624.

10. Chaoran W, Xiong Y, Chanjuan H. Operational strategy optimization of an existing ground source heat pump (gshp) system using an xgboost surrogate model. Energy and Buildings. 2024; 318:114444.

11. Kudela L, ˇSpil'aˇcek M, Posp'ıˇsil J. Influence of control strategy on seasonal coefficient of performance for a heat pump with low-temperature heat storage in the geographical conditions of central europe. Energy. 2021; 234:121276.

12. Ranganayakulu C, Seetharamu KN. Compact heat exchangers: Analysis, design and optimization using fem and cfd approach. John Wiley & Sons; 2018.

13. Akbarzadeh S, Sefidgar Z, Valipour MS, et al. A comprehensive review of research and applied studies on bifunctional heat pumps supplying heating and cooling. Applied Thermal Engineering. 2024;124280.

14. Xu Z, Li H, Shao S, et al. A semi-theoretical model for energy efficiency assessment of air source heat pump systems. Energy conversion and management. 2021; 228:113667.

15. Chua KJ, Chou SK, Yang W. Advances in heat pump systems: A review. Applied energy. 2010;87(12):3611–3624.

16. Ruhnau O, Hirth L, Praktiknjo A. Time series of heat demand and heat pump efficiency for energy system modeling. Scientific data. 2019;6(1):1–10.

17. Noorollahi Y, Saeidi R, Mohammadi M, et al. The effects of ground heat exchanger parameters changes on geothermal heat pump performance–a review. Applied Thermal Engineering. 2018;129:1645–1658.

18. Casasso A, Sethi R. Efficiency of closed loop geothermal heat pumps: A sensitivity analysis. Renewable Energy. 2014; 62:737–746.

19. Chesser M, Lyons P, O'Reilly P, et al. Air source heat pump in-situ performance. Energy and Buildings. 2021; 251:111365.

20. Singh H, Muetze A, Eames PC. Factors influencing the uptake of heat pump technology by the uk domestic sector. Renewable energy. 2010;35(4):873–878.

21. Dongellini M, Naldi C, Morini GL. Seasonal performance evaluation of electric air-to-water heat pump systems. Applied Thermal Engineering. 2015;90:1072–1081.

22. Cai W, Wang F, Chen S, et al. Importance of long-term ground-loop temperature variation in performance optimization of ground source heat pump system. Applied Thermal Engineering. 2022; 204:117945.

23. Reiners T, Gross M, Altieri L, et al. Heat pump efficiency in fifth generation ultra-low temperature district heating networks using a wastewater heat source. Energy. 2021; 236:121318.

24. Willem H, Lin Y, Lekov A. Review of energy efficiency and system performance of residential heat pump water heaters.Energy and Buildings. 2017; 143:191–201.

25. Hu B, Xu S, Wang R, et al. Investigation on advanced heat pump systems with improved energy efficiency. Energy Conversion and Management. 2019; 192:161–170.

26. Gibb D, Rosenow J, Lowes R, et al. Coming in from the cold: Heat pump efficiency at low temperatures. Joule. 2023; 7(9):1939–1942.

27. Sarbu I, Sebarchievici C. General review of ground-source heat pump systems for heating and cooling of buildings. Energy and buildings. 2014; 70:441–454.

28. S'anta R, Garbai L, F¨urstner I. Optimization of heat pump system. Energy. 2015; 89:45–54.

29. Gao B, Zhu X, Yang X, et al. Operation performance test and energy efficiency analysis of ground-source heat pump systems. Journal of Building Engineering. 2021; 41:102446.

30. Saeidi R, Karimi A, Noorollahi Y. The novel designs for increasing heat transfer in ground heat exchangers to improve geothermal heat pump efficiency. Geothermics. 2024; 116:102844.

31. Cheng J, Li N, Wang K. Study of heat-source-tower heat pump system efficiency. Procedia engineering. 2015; 121:915–921.

32. Corber'an JM, Cazorla-Mar'ın A, Marchante-Avellaneda J, et al. Dual source heat pump, a high efficiency and cost-effective alternative for heating, cooling and dhw production. International Journal of Low-Carbon Technologies. 2018; 13(2):161–176.

33. Wood C, Liu H, Riffat S. Use of energy piles in a residential building, and effects on ground temperature and heat pump efficiency. G'eotechnique. 2009;59(3):287–290.

34. Eswiasi A, Mukhopadhyaya P. Critical review on efficiency of ground heat exchangers in heat pump systems. Clean Technologies. 2020;2(2):204–224.

35. De Le'on-Ruiz J, Carvajal-Mariscal I. Thermal capacity: Additional relative efficiency to assess the overall performance of heat pump-based heating systems. Applied Thermal Engineering. 2019; 159:113841.

Appendix

Table A1. Summary of temperature distribution.

Position (m)	Mean Temp (°C)	Std Dev (°C)
0.00	-4.71×10^{-12}	3.49×10^{-11}
0.02	2.92	1.41×10^1
0.04	6.38	3.63×10^1
0.06	-6.19×10^1	6.59×10^2
0.08	-5.99×10^1	6.51×10^2
0.10	-5.66×10^1	6.36×10^2
0.12	-4.90×10^1	5.98×10^2
0.14	-4.06×10^1	5.31×10^2
0.16	-3.81×10^1	5.19×10^2
0.18	-3.48×10^1	5.05×10^2
0.20	-3.25×10^1	4.95×10^2
0.22	-2.95×10^1	4.87×10^2
0.24	-2.76×10^1	4.80×10^2
0.26	-2.41×10^1	4.63×10^2
0.28	-2.21×10^1	4.51×10^2
0.30	-1.94×10^1	4.35×10^2
0.32	-1.63×10^1	4.26×10^2
0.34	-1.31×10^1	4.19×10^2
0.36	-1.15×10^1	4.12×10^2
0.38	-9.31	4.06×10^2
0.40	-6.24	3.90×10^2
0.42	-2.89	3.76×10^2
0.44	-2.95×10^{-1}	3.60×10^2
0.46	2.50	3.55×10^2
0.48	-3.29	3.72×10^2
0.50	-6.34×10^{-1}	3.64×10^2
0.52	1.81	3.56×10^2
0.54	5.15	3.41×10^2
0.56	7.57	3.34×10^2
0.58	1.01×10^1	3.28×10^2
0.60	1.42×10^1	3.03×10^2
0.62	1.75×10^1	2.94×10^2
0.64	1.96×10^1	2.89×10^2
0.66	2.24×10^1	2.82×10^2
0.68	2.44×10^1	2.79×10^2
0.70	2.72×10^1	2.73×10^2
0.72	2.98×10^1	2.68×10^2
0.74	3.20×10^1	2.70×10^2
0.76	3.65×10^1	2.65×10^2

Table A1. (*Continued*).

Position (m)	Mean Temp (°C)	Std Dev (°C)
0.78	3.97×10^1	2.62×10^2
0.80	5.07×10^1	2.54×10^2
0.82	5.34×10^1	2.51×10^2
0.84	5.76×10^1	2.41×10^2
0.86	8.20×10^1	8.57×10^1
0.88	8.40×10^1	7.74×10^1
0.90	8.65×10^1	6.73×10^1
0.92	8.90×10^1	5.57×10^1
0.94	9.29×10^1	3.36×10^1
0.96	9.52×10^1	2.35×10^1
0.98	9.76×10^1	1.04×10^1

Table A2. Sensitivity analysis results: Mean efficiency $\eta(\kappa)$, standard deviation $\sigma\eta(\kappa)$, and sensitivity coefficient $S\kappa$.

κ	Mean Efficiency $\eta(\kappa)$	Std Dev $\sigma\eta(\kappa)$	Sensitivity Coefficient $S\kappa$
0.5	1.0023	0.2188	0
1.0	1.0016	0.2490	−0.0013
1.5	0.9889	0.2717	−0.0255
2	1.0022	0.3072	0.0267
2.5	1.0004	0.3261	−0.0036
3	1.0074	0.3544	0.0141
3.5	0.9964	0.3681	−0.0222
4	0.9938	0.3866	−0.0052
4.5	0.9863	0.4078	−0.0149
5	0.9968	0.4506	0.0209
5.5	1.0251	0.4852	0.0567
6	0.9933	0.4946	−0.0635
6.5	1.0226	0.5337	0.0585
7	1.0122	0.5690	−0.0209
7.5	0.9843	0.5896	−0.0558
8	0.9970	0.5797	0.0255
8.5	0.9963	0.6208	−0.0014
9	0.9917	0.6754	−0.0094
9.5	1.0449	0.6531	0.1065
10	0.9983	0.7143	−0.0932

Article

Experimental investigation of thermal micro-environments and local thermal sensations in enclosed and semi-enclosed localized heating systems

Runnan Lu[1], Guoqing Yu[1,*], Shuang Feng[1], Hai Ye[2]

[1] School of Environment and Architecture, University of Shanghai for Science and Technology, Shanghai 200093, China
[2] School of Architecture and Urban Planning, TongJi University, Shanghai 200092, China
* Corresponding author: Guoqing Yu, yuguoqinghvac@163.com

Abstract: Traditional building heating warms entire rooms, often leaving some dissatisfied with uneven warmth. Recently, the personalized heating system has addressed this by providing targeted warmth, enhancing comfort and satisfaction. The personalized heating system in this study is a new enclosed personalized heating system consisting of a semi-enclosed heating box and an insulated chair covered with a thick blanket. The study compares the heating effects of semi-enclosed and enclosed localized heating systems on the body and examined changes in subjects' thermal sensations. Due to the lower heat loss of the enclosed personalized heating system compared to the semi-enclosed version, it created thermal micro-environments with higher ambient temperatures. The maximum air temperature increase within the enclosed system was twice that of the semi-enclosed system, with the heating film surface temperature rising by up to 6.87 °C. Additionally, the temperature of the skin could increase by as much as 6.19 °C, allowing individuals to maintain thermal neutrality even when the room temperature dropped as low as 8 °C. A two-factor repeated measures analysis of variance revealed differences in temperature sensitivity across various body regions, with the thighs showing a notably higher response under high-power heating conditions. The corrective energy and power requirements of the enclosed personalized heating system also made it more energy-efficient than other personalized heating systems, with a minimum value reaching 6.07 W/K.

Keywords: localized heating system; personalized heating; thermal sensation; personal comfort system; heating box

1. Introduction

In the hot-summer and cold-winter regions south of the Qinling Mountains and Huai River in China, winters are characterized by cold and cloudy weather. Common heating methods in these regions include traditional heating, ventilation, and air conditioning (HVAC) systems. However, these systems often fail to meet everyone's thermal comfort requirements due to individual variability [1–6].

Localized heating systems referred to systems that did not directly heat an entire room but instead provided personalized heating to specific parts of the body, achieving the goal of warmth with lower energy consumption. Localized heating systems provide a promising alternative by offering personalized heating solutions [7]. Some researchers found that open hybrid heating devices and open radiation foot warmers improve thermal comfort and work performance [8,9]. Further research by Liu et al. [10], Luo et al. [11], Zhang et al. [12], Yang et al. [13], Yu et al. [14], and Ren [15] emphasized the effectiveness of localized heating in enhancing thermal comfort and reducing energy consumption. Specifically, semi-enclosed localized heating systems demonstrated superiority over conventional heating methods in alleviating thermal

discomfort and achieving energy savings [16–19]. Enclosed localized heating systems, in particular, offer improved heat retention compared to open systems, as observed by Zhou et al. [20] and Van Loy et al. [21] Hooshmand et al. [22] discovered that many studies on PCS focused on temperatures above 14 °C. Most PCS systems operated in open indoor environments, utilizing radiant or convective heating for the human body without creating an enclosed space around the heated area. Wu et al. [23] examined outdoor temperatures around 5 °C and found that clothing-based PCS in open car environments could not fully meet thermal demands. Wang et al. [9] reported that in environments below 13 °C, the thermal sensation provided by an open-style leg warmer diminished. Mahmoud Gaber Morsy [24] found that at ambient temperatures of 0 °C, 5 °C, and 10 °C, open radiant PCS could meet thermal demands but required a minimum energy consumption of 580 W.

In previous studies, localized heating systems did not create fully enclosed spaces, which we referred to as semi-closed localized heating systems. In contrast, systems that formed enclosed spaces were termed enclosed localized heating systems. For simplicity, these were abbreviated as semi-closed systems and enclosed systems throughout this paper. Yet, there remains a gap in studies on the heating and energy-saving effects of enclosed systems at lower temperatures. This study introduced a novel enclosed personalized heating system, which created a fully enclosed space consisting of a semi-enclosed heating box and an insulated chair covered with a thick blanket. In the enclosed space created by the localized heating system, thermal micro-environments refer to the specific temperature conditions within various parts of this space, including the air temperature, wall temperature, and film temperature. These micro-environments are essential for assessing the insulation and heating efficiency, as well as evaluating the extent of heat loss in this study. The research compared the heating performance of semi-enclosed and enclosed systems, as well as their effects on subjects when room temperatures dropped to 10 °C and 8 °C. Additionally, the study calculated the Corrective Energy and Power (CEP) of the system to assess its energy-saving potential and compared the energy consumption of the enclosed and semi-enclosed systems. Experimental results confirmed the system's strong heating performance, showing that it ensured thermal comfort even at room temperatures as low as 8 °C while offering better energy savings. The study demonstrated the superior heating performance of the enclosed system by comparing the thermal micro-environments and skin temperatures between the semi-enclosed system and the enclosed system. It also validated the feasibility of heating at lower ambient temperatures using the enclosed system. Finally, by calculating the CEP (Coefficient of Energy Performance), the study confirmed that the enclosed system achieves lower energy consumption. This further demonstrates the feasibility of personalized heating at low temperatures, with important implications for implementing energy-saving measures in buildings.

2. Methodology

2.1. Localized heating system

The localized heating system primarily comprised two components, as shown in **Figure 1**. The semi-enclosed personalized heating device consists of a table and chair,

featuring a semi-enclosed heating box beneath the table and an insulated panel surrounding the underside of the chair, as shown in **Figure 2** Inside the heating box, there are two electric heating films designed for independent efficiency control. The power of the heating films is adjustable, with the side film offering settings of 35 W, 55 W, or 75 W, and the bottom film adjustable to 20 W, 30 W, or 40 W, allowing for flexible heat management. When a thick blanket (120 cm × 200 cm) was placed between the person and the table, covering the gaps, it created a fully enclosed thermal environment for the lower body, thus constituting an enclosed personalized heating system, as shown in **Figure 3**.

Temperature monitoring within the box was comprehensive, focusing on the heating films' surface temperatures, the box's inner wall temperatures, and the internal air temperature. The temperature was measured using a copper-constantan thermocouple and recorded with an Agilent 34970A data acquisition instrument. Temperature readings were taken from several key points: Two on the side heating film (Tj-1 and Tj-2), one on the bottom heating film (Tj-3), the box's upper surface (Td-1), the lower surface (Td-2), the left wall (Tb-1), the rear wall (Tb-2), and two air temperatures measured at distances of 20 cm (Ta-1) and 40 cm (Ta-2) from the box's upper surface，and air temperature under the seat (Ta-3). This detailed temperature arrangement facilitated precise control and monitoring, as depicted in **Figure 4**.

The primary focus of the heating system tested in this research was the lower body. To simplify the measurement process and ensure consistency in assessing the temperature of the human lower body, temperatures were exclusively measured on the left leg. Therefore, three specific locations on the lower body surface—the left thigh, left leg, and sole of the left sole—were chosen for temperature measurement.
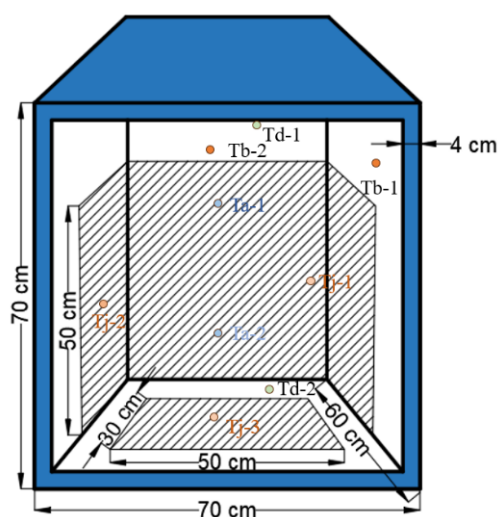

Figure 1. Blanket installation diagram.
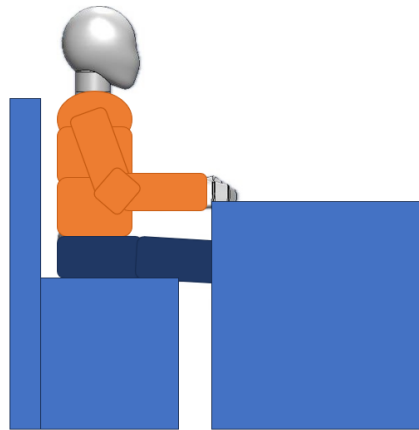
Figure 2. Schematic diagram of semi-localized heating system.
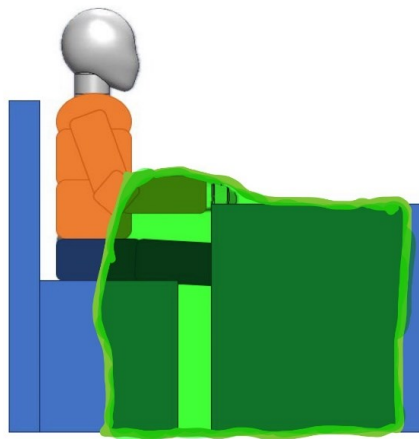
Figure 3. Schematic diagram of enclosed localized heating system.

Figure 4. Layout of temperature measurement points inside the heated box.

2.2. Ethical consideration and participants

The participants in this experiment were eight college students, comprising an equal number of males and females. During the experiment, participants were required to wear standardized clothing, including a down jacket, sweater, casual jeans, athletic

socks, and sneakers, with a thermal resistance of approximately 1.37 clo. The participants were in a sedentary working state, with a metabolic rate of around 65 W/m². The average relative humidity was maintained at 55.9% and was considered constant throughout the experiment. These measures ensured that other variables affecting skin temperature and thermal sensation, including humidity, clothing insulation, and activity level, were controlled during the experiment. The basic information of the eight subjects in this experiment is shown in **Table 1**. Before the experiment, informed consent was obtained from all subjects.

Table 1. Basic subject parameters.

	Age (year)	Height (cm)	Weight (kg)	BMI (kg/m^2)
Average value	24.33	171.33	67.22	22.80
Standard deviation	1.05	5.29	13.96	4.08

2.3. Experimental procedure

At the beginning of the experiment, heat flow sensors were attached to the thighs, legs, and soles of the subjects to detect the heat flux exchanged between different body parts and the experimental environment. During the experiment, the subjects completed a questionnaire every 10 min regarding the thermal sensation of each part (thigh, leg, sole) and the whole. The Thermal Sensation Voting (TSV) scale from ASHRAE [25], ranging from −3 to 3 (corresponding to cold, cool, slightly cool, neutral, slightly warm, warm, and hot), was adopted in our experiment to evaluate thermal sensation. The first experiment investigated the changes in the thermal micro-environments within the system and the local skin changes of the subjects when using semi-enclosed and enclosed localized heating systems. The experimental conditions for assessing the thermal effect are shown in **Table 2**. The flowchart of this process is depicted in **Figure 5**. Entry into the laboratory marked the start of the experiment, during which measurements were taken.
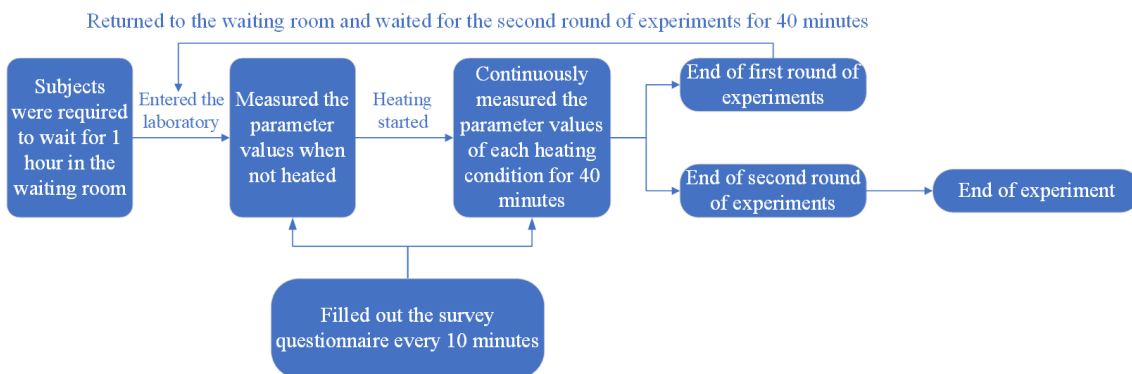
Figure 5. Experimental flowchart.

The second experiment focused on investigating the heating effect at low room temperatures, specifically analyzing the performance of the localized heating system under colder indoor conditions. The experimental setup is detailed in **Table 3**. The experiment was conducted in Shanghai during November when the average indoor temperature ranged from 8 °C to 10 °C. Consequently, the experimental conditions

were set to 10 °C and 8 °C. The experimental procedure followed a similar approach to the one described above.

Table 2. Comparison of semi-enclosed and enclosed localized heating systems.

Working conditions		Indoor temperature	Systems	Side heating film power + Bottom heating film power
The first round	1	12 °C	Semi-closed system	0W
	2			Side 35 W + Bottom 20 W
	3			Side 55 W + Bottom 30 W
	4			Side 75 W + Bottom 40 W
The second round	5		Enclosed localized heating system	0W
	6			Side 35 W + Bottom 20 W
	7			Side 55 W + Bottom 30 W
	8			Side 75 W + Bottom 40 W

Table 3. Experimental conditions for heating effect of enclosed system at low temperatures.

Working condition	Indoor temperature	Power
1	10 °C	0 W
2		Side 35 W + Bottom 20 W
3		Side 55 W + Bottom 30 W
4		Side 75 W + Bottom 40 W
5	8 °C	0 W
6		Side 35 W + Bottom 20 W
7		Side 55 W + Bottom 30 W
8		Side 75 W + Bottom 40 W

2.4. Statistical analysis

All statistical analyses were conducted using Statistical Product and Service Solutions（SPSS）, with the significance level set at $\alpha = 0.05$. Before performing analysis of variance (ANOVA), Mauchly's sphericity test was applied to the skin temperatures of different heating conditions and body parts to verify whether the data satisfied the sphericity assumption. A two-factor repeated measures ANOVA was used to assess the effects of heating conditions and body parts on skin temperature responses. The heating conditions included four levels: No heating, Side 35 W + Bottom 20 W, Side 55 W + Bottom 30 W, and Side 75 W + Bottom 40 W. The body parts included three levels: Foot sole, lower leg, and thigh, to evaluate the main effects of each variable. Post hoc pairwise comparisons between groups were conducted using Bonferroni-corrected t-tests.

2.5. Energy consumption

Zhang et al. [26] introduced the term "Corrective Power" (CP) to quantify the degree to which a Personal Comfort System (PCS) can adjust hot or cold ambient temperatures to neutral levels. CP was defined as the difference between the environmental temperatures with and without the use of PCS, under the same thermal

sensation. Building on Zhang's work, He et al. [27] proposed the concept of Corrective Energy and Power (CEP), which is formulated as shown in Equation (1). CEP is a key indicator in the energy efficiency evaluation of PCS, representing the amount of energy required to adjust thermal sensation to a comfortable level. This measures the ratio of an individual's average heating or cooling power (Q) to the CP of the PCS, indicating the energy consumption level of the PCS.

$$CEP = Q/CP \qquad (1)$$

The units of Q are watts (W), and thus, the units of CEP are watts per kelvin (W/K). The units of CP are kelvin (K). The ambient air temperature was set at 24 °C when the subjects reached a neutral thermal sensation.

3. Results

3.1. Comparison of semi-enclosed and enclosed systems

Two temperature measuring points were designated for the side heating film: The left surface T_{j-1} and the rear surface T_{j-2}. The side heating film's surface temperature was determined by averaging these two points. Meanwhile, the bottom heating film's temperature was measured at point T_{j-3}. **Table 4** showed the surface temperature of the heating film in the heating box under unheated conditions. From the table, we can observe that under unheated conditions, the heating film temperature of the enclosed system was consistently higher than that of the semi-closed system. Although the temperature difference was minor, it was generally around 1 °C between the two systems. The largest temperature difference, 1.2 °C, was noted in the rear wall heating film. This indicates that even without active heating, the enclosed system maintained a higher heating film temperature due to the addition of a thick blanket, which helped reduce heat loss.

Table 4. The surface temperature of the initial heating film inside the heated box under no heating conditions with an indoor temperature of 12 °C.

Working condition	Bottom heating film temperature (°C)	Rear wall heating film temperature (°C)	Sidewall heating film temperature (°C)	The average temperature of side heating film (°C)
Enclosed system	15.4	15.4	15.1	15.2
Semi-closed system	14.4	14.2	14.1	14.1

Figure 6 illustrates that the surface temperature of the heated film is higher than in the initial condition without heating, across various heating power levels. The figure showed that as heating power increased, the surface temperature of the heated film rose accordingly. Because the bottom heating film was in direct contact with the feet, heat conduction occurred from the feet to the bottom heating film, resulting in the bottom heating film temperature consistently being higher than the side heating film temperature. Additionally, the temperature of the enclosed system remained consistently higher than that of the semi-closed system, with the temperature difference increasing as power increased. The maximum temperature difference, 6.875 °C, occurred at a heating power of 75 W for the side heating film.
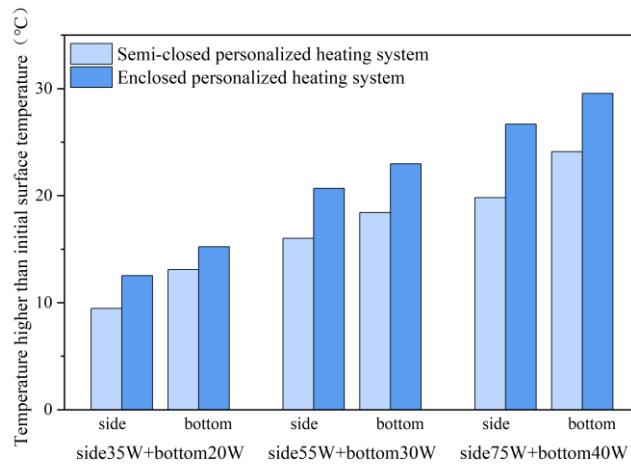
Figure 6. The surface temperature of the heated film higher than that of the initial no-heating condition under different heating powers.

Figure 7 reveals that temperatures at points Ta-1, Ta-2, and Ta-3 are elevated above the indoor air temperature under various operating conditions. The figure showed that the air temperature at Ta-1 was the highest, as Ta-1 was located above the heating box, where heated air rose and accumulated. In both the closed and semi-closed systems, the air temperature within the thermal micro-environments increased with higher heating power. However, the figure also revealed that the increase in air temperature was more pronounced in the closed localized heating system, with the gap between the two systems widening as heating power rose. When the heating power reached Side 75 W + Bottom 40 W, the air temperature above the indoor air temperature in the closed localized heating system was more than double that of the semi-closed system.
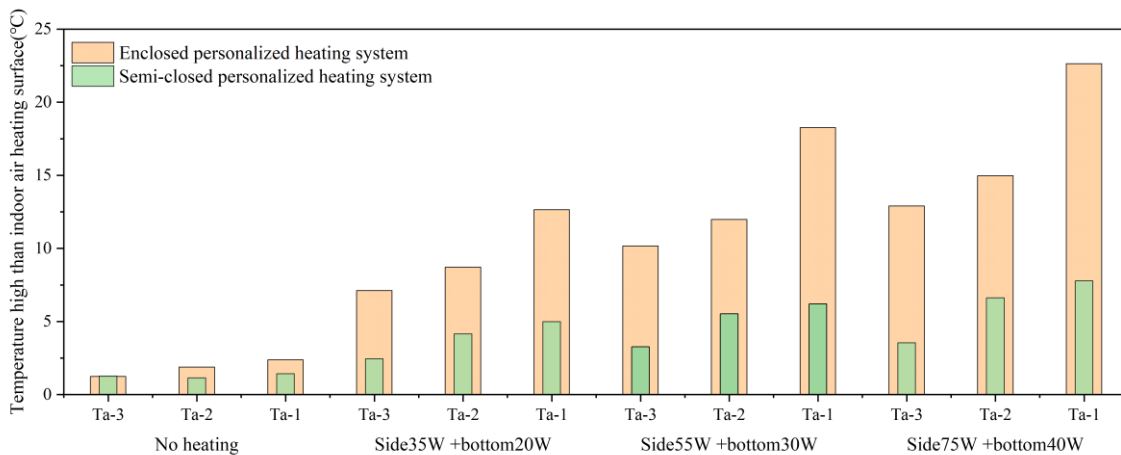
Figure 7. The air temperature inside the box (Ta-1, Ta-2) and under the seat (Ta-3) higher than the indoor ambient temperature (12 °C).

Table 5 shows that the average temperature of the heating box walls was calculated from the averages of Tb-1, Tb-2, Td-1, and Td-2. The average temperature of the heating box walls followed a similar trend to the air temperature and heating film temperature, increasing as heating power rose. This temperature was consistently

higher in the enclosed system, with the gap between it and the semi-closed system widening as heating power increased.

Table 5. The average temperature of the inner wall under the heated box and seat higher than the indoor air temperature under different working conditions.

Working condition		No heating	Side 35 W + Bottom 20 W	Side 55 W + Bottom 30 W	Side 75 W + Bottom 40 W
The average temperature of the walls of the heating box	Semi-closed system	2.32	7.18	10.00	11.60
	Enclosed system	3.31	12.50	16.63	20.20

Local skin temperatures in the lower body of the human body were measured through experiments, including the sole (Tsole), leg (Tleg), and thigh (Tthigh), as shown in **Figure 8**. The figure showed that skin temperature increased with higher heating power, with a more pronounced rise in the enclosed system. This increase became more substantial as heating power rose, especially for the leg area, where the skin temperature reached 34.53 °C at a heating power of Side 75 W + Bottom 40 W—an increase of 6.19 °C compared to the semi-closed system.
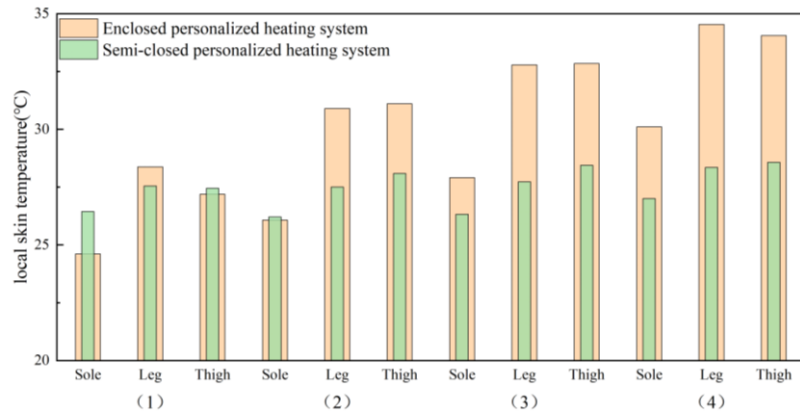
Figure 8. Local skin temperature of the lower body of the human body.
(1) No heating; (2) Side 35 W + Bottom 20 W; (3) Side 55 W + Bottom 30 W; (4) Side 75 W + Bottom 40 W.

3.2. The effect of enclosed system at room temperature of 10 °C

Table 6. Heating film surface temperature at an indoor temperature of 10 °C.

Working conditions	Bottom heating film temperature (°C)	Rear wall heating film temperature (°C)	Left wall heating film temperature (°C)	Average temperature of side heating film (°C)
Unheated	11.9	12.1	12.4	12.3
Side 35 W + Bottom 20 W	28.9	27.4	27.8	27.6
Side 55 W + Bottom 30 W	36.2	34.3	34.8	34.6
Side 75 W + Bottom 40 W	42.1	40.5	41.2	40.9

To investigate the heating performance of this enclosed system on the lower body at lower indoor temperatures, further temperature measurement experiments and analyses are required at indoor temperatures of 10 °C and 8 °C. At an indoor

temperature of 10 ℃, the surface temperatures of the heating film are detailed in **Table 6**.

As demonstrated in **Table 7**, with the increase in heating power, the wall average temperatures of the heated box and the underside of the seat significantly increased. The heated box wall's average temperature rose more rapidly than that of the wall beneath the seat.

Table 7. The average temperatures of the wall of heated box and the side wall under the seat higher than the indoor ambient temperature (about 10 ℃).

| Working condition	No heating	Side 35 W + Bottom 20 W	Side 55 W + Bottom 30 W	Side 75 W + Bottom 40 W
The average temperature of the walls of the heating box	2.70	12.38	16.64	20.66

Figure 9 illustrates the comparison of air temperatures at different positions inside the box (Ta-1, Ta-2, Ta-3), which were higher than the indoor air temperature. As power increased, the air temperature rose, with Ta-1 having the highest and fastest increase, reaching a maximum of 33.68 ℃.
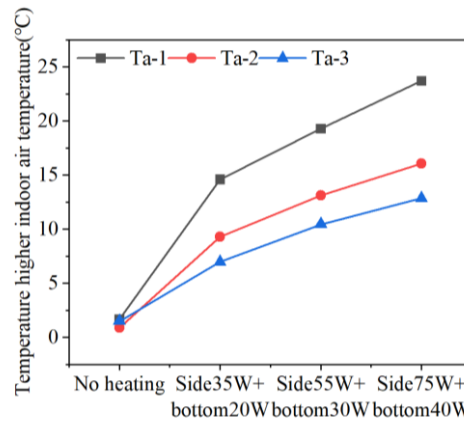

Figure 9. The air temperature inside the box when the indoor temperature was about 10 ℃.

Figure 10 illustrated the changes in local skin temperatures across different heating powers. The results of Mauchly's test for sphericity indicated that the assumption of sphericity was met ($p = 1.00 > 0.05$), confirming that the data satisfied the sphericity requirement for ANOVA. The two-factor repeated measures ANOVA showed that different working conditions approached a significant effect on skin temperature response ($F = 4.58$, $p = 0.0539$), while there was a significant difference in skin temperature response across different body regions ($F = 5.85$, $p = 0.039$). **Tables 8** and **9** present the post-hoc test results for the main effects. As shown in the tables, under the higher heating condition (Side 75 W + Bottom 40 W), temperature was significantly higher than under the lower heating power conditions (Side 35 W + Bottom 20 W and Side 55 W + Bottom 30 W). No significant temperature differences were observed between other conditions. Under the same heating condition, the thigh's temperature response was significantly higher than that of the leg. However, the temperature difference between the sole and the other regions (leg and thigh) did not

reach the level of significance. **Figure 11** depicts the local and overall thermal sensation of the human body when the indoor temperature was approximately 10 ℃. Participants completed a thermal sensation survey every 10 min during each condition, with each condition lasting 40 min, resulting in four completions. The figure showed that as heating power increased, the TSV value also rose. Under certain conditions, the thermal sensation in the thigh was higher than the overall body sensation.
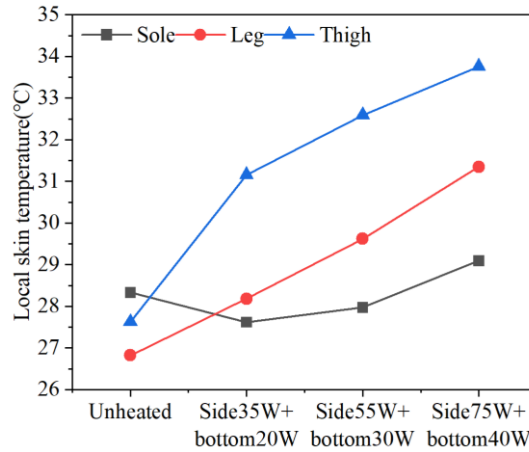
Figure 10. Local skin temperature of the lower body of the human body when the indoor temperature was about 10 ℃.
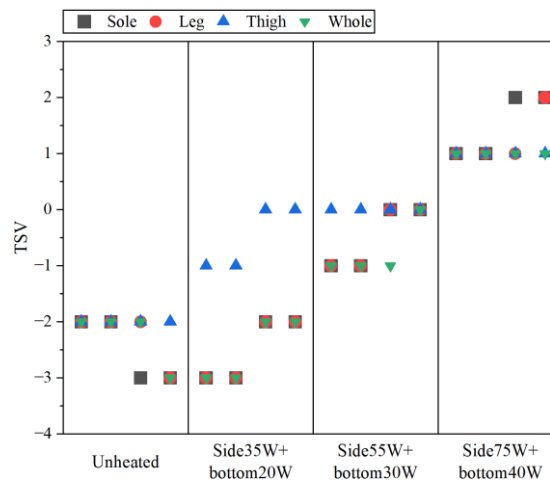
Figure 11. Local and overall thermal sensation of the human body when the indoor temperature was about 10 ℃.

Table 8. Post-hoc test results for working condition main effect.

Heating Condition Comparison	*t*-value	*p*-value
Unheated vs. Side 35 W + Bottom 20 W	−1.14	0.373
Unheated vs. Side 55 W + Bottom 30 W	−1.60	0.251
Unheated vs. Side 75 W + Bottom 40 W	−2.39	0.139
Side 35 W + Bottom 20 W vs. Side 55 W + Bottom 30 W	−2.98	0.097
Side 35 W + Bottom 20 W vs. Side 75 W + Bottom 40 W	−4.85	0.040*
Side 55 W + Bottom 30 W vs. Side 75 W + Bottom 40 W	−6.93	0.020*

* indicates a statistically significant difference ($p < 0.05$).

Table 9. Post-hoc test results for body part main effect.

Body Part Comparison	*t*-value	*p*-value
Sole vs. Leg	−0.89	0.437
Sole vs. Thigh	−2.38	0.097
Leg vs. Thigh	−4.47	0.021*

* indicates a statistically significant difference ($p < 0.05$).

### 3.3. The effect of enclosed system at room temperature of 8 ℃

Table 10 demonstrates that when the indoor temperature was 8 ℃, the surface temperatures of both the side and bottom heating films exhibited similar values across three different working conditions. Compared to the data in **Table 6**, where the indoor temperature was 10 ℃, there was a slight decrease in the surface temperatures of the heating films. **Table 11** reveals that the average temperatures of the heated box's wall were higher than the indoor air temperature.

Table 10. Surface temperature of heating film when indoor temperature was 8 ℃.

Working conditions	Bottom heating film temperature (℃)	Rear wall heating film temperature (℃)	Left wall heating film temperature (℃)	Average temperature of side heating film (℃)
Unheated	10.8	10.3	10.4	10.4
Side 35 W + Bottom 20 W	28.1	25.6	26.0	25.8
Side 55 W + Bottom 30 W	34.1	31.7	32.1	31.9
Side 75 W + Bottom 40 W	40.8	37.7	38.4	38.0

Table 11. The average temperature of the wall of heated box and the lower side wall of the seat higher than the indoor ambient temperature (about 8 ℃).

| Working conditions	No heating	Side 35 W + Bottom 20 W	Side 55 W + Bottom 30 W	Side 75 W + Bottom 40 W
The average temperature of the walls of the heating box	3.68	13.74	17.20	20.85
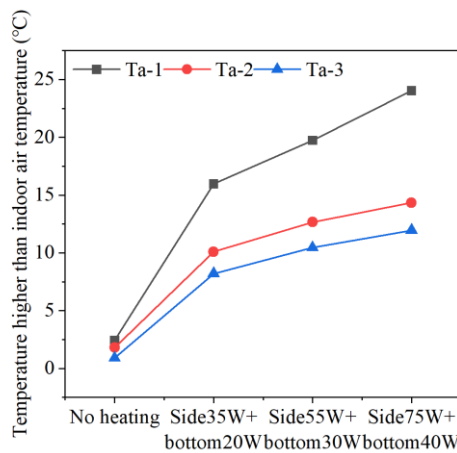
Figure 12. The air temperature inside the box when the indoor temperature was about 8 ℃.

Figure 12 displays the internal air temperatures (Ta-1, Ta-2) within the heated box and the air temperature under the seat (Ta-3), all of which were higher than the

indoor air temperature. When the heating was off, the three air temperatures were roughly the same. After turning on the heating, the temperature of Ta-1 rose rapidly, becoming significantly higher than Ta-2 and Ta-3, with Ta-2 slightly higher than Ta-3.
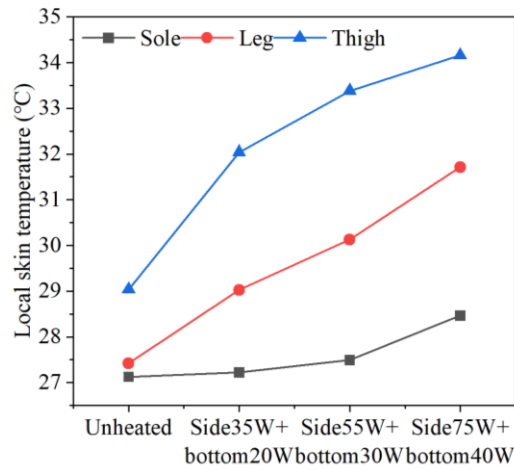
Figure 13. Local skin temperature of the lower body of the human body when the indoor temperature was about 8 °C.
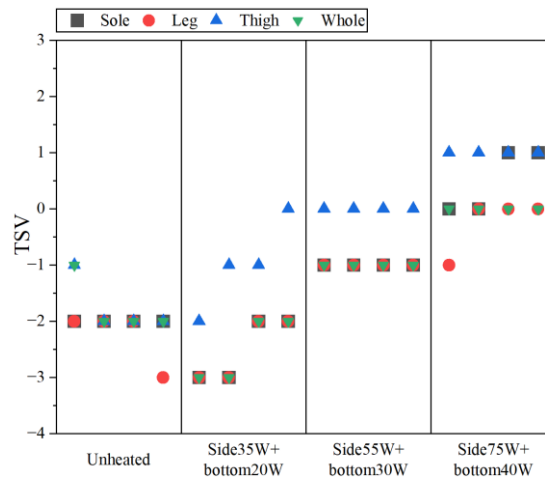
Figure 14. Local and overall thermal sensation of the human body at an indoor temperature of approximately 8 °C.

Figure 13 illustrates the temperature changes in the lower body's skin at an indoor temperature of 8 °C. The results of Mauchly's test for sphericity indicated that the assumption of sphericity was met ($p = 1.00 > 0.05$), confirming that the data satisfied the sphericity requirement for ANOVA. The two-factor repeated measures ANOVA showed that different working conditions had a near-significant effect on skin temperature response ($F = 7.46$, $p = 0.0189$), and there was a significant difference in skin temperature response across different body regions ($F = 22.82$, $p = 0.0016$). **Tables 12** and **13** present the post-hoc test results for the main effects. As shown in the tables, under the higher heating condition (Side 75 W + Bottom 40 W), the temperature was significantly higher than under lower heating power conditions (Side 35 W + Bottom 20 W and Side 55 W + Bottom 30 W). The temperature of the thigh was significantly higher than that of the sole and leg. **Figure 14** depicts the local

and overall thermal sensation of the human body when the indoor temperature was approximately 8 °C. As the heating power increased, the TSV value also rose. However, compared to the 10 °C room temperature condition, the heating effect was less pronounced in the last two conditions. Despite this, during the middle two conditions, the thermal sensation in the thigh remained higher than the overall thermal sensation.

Table 12. Post-hoc test results for heating condition main effect.

Heating Condition Comparison	*t*-value	*p*-value
Unheated vs. Side 35 W + Bottom 20 W	−1.87	0.202
Unheated vs. Side 55 W + Bottom 30 W	−2.14	0.165
Unheated vs. Side 75 W + Bottom 40 W	−3.13	0.089
Side 35 W + Bottom 20 W vs. Side 55 W + Bottom 30 W	−2.78	0.108
Side 35 W + Bottom 20 W vs. Side 75 W + Bottom 40 W	−4.80	0.041*
Side 55 W + Bottom 30 W vs. Side 75 W + Bottom 40 W	−4.55	0.045*

* indicates a statistically significant difference ($p < 0.05$).

Table 13. Post-hoc test results for body part main effect.

Body Part Comparison	*t*-value	*p*-value
Sole vs. Leg	−3.13	0.052
Sole vs. Thigh	−4.98	0.016*
Leg vs. Thigh	−7.07	0.006*

* indicates a statistically significant difference ($p < 0.05$).

4. Discussions

4.1. The enclosed system had a noticeably stronger heating effect on the thermal micro-environments compared to the semi-closed system

Table 4 indicate that the initial ambient temperature in the laboratory was similar under both the semi-closed and enclosed systems. The temperature difference on the heating film surface inside the heating box was approximately 1 °C, suggesting that the blanket's coverage reduced heat loss. **Figures 6** and **7** show that after the heating was turned on, the heating power gradually increased, and the temperatures of the heating films on the sides and bottom also rose. Although the heating power of the side films was higher than that of the bottom, their surface temperatures were consistently 5 °C lower. This discrepancy was due to the bottom heating films not only generating their heat but also being in direct contact with the sole, allowing heat from the human body to transfer to them through conduction, thereby raising their surface temperatures.

The internal air temperatures, Ta-1 being higher and Ta-3 lower, indicated that the heated air rose, causing warmer air to accumulate at the top. The enclosed system also prevented heat loss through gaps between the table and the person, significantly reducing heat loss. Under the enclosed system, the internal air temperature was much higher; with the heating power set to 75W on the sides and 40W at the bottom, the maximum temperature of Ta-1 reached 22.63 °C, which was 14.8 °C higher than under

the semi-closed system. These results clearly demonstrate that under the same heating conditions, the enclosed system significantly enhanced the heating effect of the air inside the enclosure.

4.2. The enclosed system provided a significantly stronger heating effect on the human body compared to the semi-closed system

Because the wall temperature of the enclose system and the film surface temperature are both higher than those of the semi-closed system, the air temperature inside the enclosed system is also higher. This results in greater heat convection and radiation to the human skin, thereby increasing skin temperature. **Table 5** shows that under the semi-closed system, the skin temperature of the soles first decreased and then increased. However, under the enclosed system, the temperature of the soles gradually increased. Initially, the skin temperature of the soles under the enclosed system was 1.8 °C lower than under the semi-closed system. Eventually, when the heating film's power reached 75W on the sides and 40W at the bottom, the skin temperature of the soles under the enclosed system was 3.10 °C higher than that under the semi-closed system. This occurred because, under the enclosed system, the ground temperature was lower, resulting in a lower initial temperature of the soles. With the increase in heating power, the heating effect of the enclosed system became more pronounced, thereby raising the skin temperature of the soles. The skin temperatures of the sole, leg, and thigh all increased progressively with the power of the heating films. At 75W on the side and 40W on the bottom, the temperatures reached 30.10 °C for the sole, 34.53 °C for the leg, and 34.05 °C for the thigh, showing improvements of 3.10 °C, 6.18 °C, and 5.48 °C, respectively.

4.3. The effect of enclosed system on thermal sensation on lower body at low temperatures (10 °C, 8 °C)

As shown in **Figures 11** and **14**, when the indoor temperature was 10 °C, thermal comfort was achieved in the final 10 min under the condition of Side 55W + Bottom 30W. At an indoor temperature of 8 °C, under the same condition, only the thigh reached thermal comfort. The leg and sole reached thermal neutrality and comfort at a heating power of 75W on the side and 40W on the bottom. The thigh's thermal sensation adjusted more noticeably, achieving a comfortable and thermally neutral state with just 35W on the side and 20W on the bottom.

Based on the results of the two-factor repeated measures analysis, the following observations were made: At an ambient temperature of 10 °C, the effects of different heating conditions on skin temperature approached significance. At 8 °C, the effects of different heating conditions on skin temperature were significant. In both cases, higher heating power had a more pronounced impact on skin temperature. Under the same heating conditions, the temperature differences among different body parts were significant. At 10 °C, the temperature response of the thigh was significantly higher than that of leg. At 8 °C, the thigh's temperature response was significantly higher than both leg and sole. As heating power increased, the differences in temperature responses among body parts became increasingly significant, particularly in the thigh, where the response to higher heating power was more pronounced. These findings

indicate that different body parts exhibit varying sensitivities to temperature, with the thigh demonstrating a notably higher response under high power conditions.

In the final heating stage, the sensation improved to slightly warm, suggesting a human preference for warmer conditions in colder environments. The overall thermal sensation closely aligned with the leg and sole's changes, indicating that the body's overall comfort level is largely influenced by its most uncomfortable parts [28,29].

4.4. The energy consumption of enclosed system

Previous studies have shown that the enclosed localized heating system provides superior heating effectiveness and insulation performance. However, the energy consumption of this system has not yet been thoroughly discussed. Some researchers have already proposed energy consumption metrics specifically for PCS. When the room temperature was 10 ℃, the value of CP was 14K. The subjects achieved a neutral thermal sensation within an enclosed system with a system power of 55W on the sides and 30W on the bottom, resulting in a CEP of 6.07 W/K. When the room temperature decreased to 8 ℃, the value of CP rose to 16K. At this lower temperature, the subjects maintained a neutral thermal sensation in the heating system with a power of 75W on the sides and 40W on the bottom, giving a CEP of 7.19 W/K.

At room temperatures of 8 ℃ and 10 ℃, the CEP values for the enclosed system were 6.07 W/K and 7.19 W/K, respectively. These values are lower compared to those of other semi-closed systems, indicating lower energy consumption. Moreover, the ambient temperatures discussed in this paper are lower than those in most studies on semi-closed systems, which typically feature ambient temperatures above 12 ℃. [26,27,30,31] Although the CEP of these semi-closed systems is lower than that in our study, it remains unknown whether these systems can provide thermal comfort in environments with temperatures below 12 ℃.

4.5. Limitations

This study analyzed the impact of personalized heating devices on skin temperature, heat flux, and thermal sensation by selecting only eight subjects, resulting in a small sample size. Future studies should increase the sample size to obtain more comprehensive data on local thermal sensations, skin temperatures, and heat flux. Additionally, the thermal sensation model in this study considered only the skin temperatures of three parts of the lower body. Future research should include testing the skin temperatures of more body parts.

5. Conclusions

In this study, a new enclosed system was introduced. The study compared the heating performance of semi-enclosed and enclosed systems, examined the enhanced thermal sensation provided by the enclosed system at lower indoor temperatures, and analyzed its energy-saving effects. Key findings include:

1) Due to the lower heat loss of the enclosed system compared to the semi-closed system, the thermal micro-environment temperature was higher. When the enclosed system was activated, the increase in air temperature inside the heating box was significantly higher than that of the semi-closed system, reaching up to

twice as much. Additionally, the surface temperature of the heating film in the enclosed system was higher than that in the semi-closed system, with a maximum temperature difference of 6.875 °C. Consequently, the enclosed system led to a substantial increase in the skin temperature of the lower body, with a maximum rise of 6.19 °C.

2) Given the elevated thermal micro-environment temperature provided by the enclosed system, participants maintained thermal neutrality even as indoor temperatures fell to 8 °C and 10 °C. At an indoor temperature of 10 °C, when the heating power reached Side 55W + Bottom 30W, the Thermal Sensation Vote (TSV) essentially reached 0, thus achieving thermal neutrality. When the room temperature was 8 °C, at a heating power of Side 75W + Bottom 40W, the TSV essentially reached 0.

3) The response of skin temperature to different working conditions approached a significant level ($F = 4.58$, $p = 0.0539$), while the response among different body parts showed a significant difference ($F = 5.85$, $p = 0.039$). As heating power increased, the temperature response differences between body parts became more pronounced, particularly in the thigh region, which exhibited a significantly stronger response to higher heating power. This indicates that body parts vary in their sensitivity to temperature, with the thigh showing a notably greater response under high-power heating conditions. Under identical personalized heating conditions, the thighs were the first to reach thermal comfort. In environments with lower room temperatures, the overall sensation of warmth corresponded with the least comfortable parts.

4) At a room temperature of 8 °C, the CEP of the enclosed system used by the subjects was 6.07 W/K. At a room temperature of 10 °C, the CEP was 7.19 W/K. Compared to semi-closed systems, this enclosed system is more energy-efficient.

This study provided a basis for the practical application of personalized heating in buildings, demonstrating that fully enclosed heating systems are better suited to meet heating demands under low ambient temperatures compared to open or semi-enclosed systems. Additionally, the superior energy efficiency of fully enclosed localized heating systems offers a promising direction for research on energy-saving strategies in building environments.

Conflict of interest: The authors declare no conflict of interest.

References

1. Ruan J, Liu J. Investigation into the thermal comfort and some passive strategies for traditional architecture of Li nationality in South China. Indoor and Built Environment. 2023; 32(7): 1349–1371. doi: 10.1177/1420326x231159888

2. Karjalainen S. Thermal comfort and gender: A literature review. Indoor Air. 2012; 22(2): 96–109. doi: 10.1111/j.1600-0668.2011.00747.x

3. Indraganti M, Rao KD. Effect of age, gender, economic group and tenure on thermal comfort: A field study in residential buildings in hot and dry climate with seasonal variations. Energy and Buildings. 2010; 42(3): 273–281. doi: 10.1016/j.enbuild.2009.09.003

4. Wu X, Liu G, Tian Z, et al. Occupant's thermal comfort in a radiant ceiling cooling room with hot wall surface. Indoor and Built Environment. 2022; 32(4): 699–718. doi: 10.1177/1420326x221135315

5. van Hoof J. Thermal comfort: research and practice. Frontiers in Bioscience. 2010; 15(1): 765.

6. Zheng J, Yu T, Lei B, et al. Experimental study on the thermal performance of radiant floor heating system with the influence of solar radiation on the local floor surface. Indoor and Built Environment. 2023; 32(5): 977–991. doi: 10.1177/1420326x221148729

7. Wang J, Yu CW, Cao S-J. Planning for sustainable and ecological urban environment: Current trends and future developments. Indoor and Built Environment. 2022; 32(4): 627–631. doi: 10.1177/1420326x221135758

8. Su W, Yang B, Zhou B, et al. A novel convection and radiation combined terminal device: Its impact on occupant thermal comfort and cognitive performance in winter indoor environments. Energy and Buildings. 2021; 246. doi: 10.1016/j.enbuild.2021.111123

9. Wang H, Wang J, Li W, et al. Experimental study on a radiant leg warmer to improve thermal comfort of office workers in winter. Building and Environment. 2022; 207. doi: 10.1016/j.buildenv.2021.108461

10. Liu B, Wang H, Ji K, et al. Using personal comfort systems during the post-heating season in a cold climate: A field study in offices. Case Studies in Thermal Engineering. 2023; 45. doi: 10.1016/j.csite.2023.102974

11. Luo W, Kramer R, de Kort Y, et al. Personal comfort systems and cognitive performance: Effects on subjective measures, cognitive performance, and heart rate measures. Energy and Buildings. 2023; 278. doi: 10.1016/j.enbuild.2022.112617

12. Zhang H, Arens E, Taub M, et al. Using footwarmers in offices for thermal comfort and energy savings. Energy and Buildings. 2015; 104: 233–243. doi: 10.1016/j.enbuild.2015.06.086

13. Yang Z, Zhang W, Liu H, et al. Field study of meeting thermal needs of occupants in old residential buildings in low-temperature environments using personalized local heating. Building and Environment. 2024; 247. doi: 10.1016/j.buildenv.2023.111004

14. Yu G, Gu Z, Yan Z, et al. Investigation and comparison on thermal comfort and energy consumption of four personalized seat heating systems based on heated floor panels. Indoor and Built Environment. 2020; 30(8): 1252–1267. doi: 10.1177/1420326x20939145

15. Ren Z, Gao X, Xiao Y, et al. Thermal comfort and energy conservation of a four-sided enclosed local heating device in a cold environment. Building and Environment. 2023; 228. doi: 10.1016/j.buildenv.2022.109837

16. He Y, Li N, Lu J, et al. Meeting thermal needs of occupants in shared space with an adjustable thermostat and local heating in winter: An experimental study. Energy and Buildings. 2021; 236. doi: 10.1016/j.enbuild.2021.110776

17. Yang B, Wu M, Li Z, et al. Thermal comfort and energy savings of personal comfort systems in low temperature office: A field study. Energy and Buildings. 2022; 270. doi: 10.1016/j.enbuild.2022.112276

18. He Y, Parkinson T, Arens E, et al. Creating alliesthesia in cool environments using personal comfort systems. Building and Environment. 2022; 209. doi: 10.1016/j.buildenv.2021.108642

19. Zhang J, Zhou X, Lei S, et al. Energy and comfort performance of occupant-centric air conditioning strategy in office buildings with personal comfort devices. Building Simulation. 2021; 15(5): 899–911. doi: 10.1007/s12273-021-0852-1

20. Zhou L, Li N, He Y, et al. A field survey on thermal comfort and energy consumption of traditional electric heating devices (Huo Xiang) for residents in regions without central heating systems in China. Energy and Buildings. 2019; 196: 134–144. doi: 10.1016/j.enbuild.2019.05.013

21. Loy NV, Verbeeck G, Knapen E. Passive and active personalized heating systems at a lower indoor ambient temperature. IOP Conference Series: Earth and Environmental Science. 2020; 588(2). doi: 10.1088/1755-1315/588/2/022042

22. Hooshmand SM, Zhang H, Javidanfar H, et al. A review of local radiant heating systems and their effects on thermal comfort and sensation. Energy and Buildings. 2023; 296. doi: 10.1016/j.enbuild.2023.113331

23. WuJ, Liu J, Zhao J, et al. Influencing assessment of different heating modes on thermal comfort in electric vehicle cabin. Energy and Built Environment. 2024; 5(4): 556–567. doi.org/10.1016/j.enbenv.2023.04.005

24. Ali AHH, Morsy MG. Energy efficiency and indoor thermal perception: a comparative study between radiant panel and portable convective heaters. Energy Efficiency. 2010; 3(4): 283–301. doi: 10.1007/s12053-010-9077-3

25. American Society of Heating, Inc. ANSI/ASHRAE Standard 55–2017: Thermal Environmental Conditions for Human Occupancy. ASHRAE Publishing; 2017.

26. Zhang H, Arens E, Zhai Y. A review of the corrective power of personal comfort systems in non-neutral ambient environments. Building and Environment. 2015; 91: 15–41. doi: 10.1016/j.buildenv.2015.03.013

27. He Y, Li N, Zhou L, et al. Thermal comfort and energy consumption in cold environment with retrofitted Huotong (warm-barrel). Building and Environment. 2017; 112: 285–295. doi: 10.1016/j.buildenv.2016.11.044

28. Arens E, Zhang H, Huizenga C. Partial- and whole-body thermal sensation and comfort—Part I: Uniform environmental conditions. Journal of Thermal Biology. 2006; 31(1–2): 53–59. doi: 10.1016/j.jtherbio.2005.11.028

29. Melikov A, Pitchurov G, Naydenov K, et al. Field study on occupant comfort and the office thermal environment in rooms with displacement ventilation. Indoor Air. 2005; 15(3): 205–214. doi: 10.1111/j.1600-0668.2005.00337.x

30. Pasut W, Zhang H, Arens E, et al. Energy-efficient comfort with a heated/cooled chair: Results from human subject tests. Building and Environment. 2015; 84: 10–21. doi: 10.1016/j.buildenv.2014.10.026

31. Deng Q, Wang R, Li Y, et al. Human thermal sensation and comfort in a non-uniform environment with personalized heating. Science of The Total Environment. 2017; 578 :242–248. doi: 10.1016/j.scitotenv.2016.05.172

Article

Initial analysis and improvements to a stepped piston segregated scavenge engine for ultra-low emission range extender and hybrid electric vehicles

Peter Hooper

Bernard Hooper Engineering Ltd, Wolverhampton WV3 9BU, UK; peter.hooper@bernardhooperengineering.co.uk

Abstract: Segregating the scavenging processes from the lubrication methodology is a very effective way of improving two-stroke cycle engine durability. The application of stepped or twin diameter pistons is one such method that has repeatedly shown significantly greater durability over comparable crankcase scavenged engines together with an ability to operate on neat fuel without any added oil. This research study presents the initial results observed from a gasoline/indolene fuelled stepped piston engine ultimately intended for Hybrid Electric Vehicle and/or Range Extender Electric Vehicle application using hydrogen fuelling. Hydrogen fuelling offers the potential to significantly reduce emissions, with near zero emission operation possible, and overcoming the serious issues of range anxiety in modern transport solutions. The low environmental impact is discussed along with results from 1-d Computational Fluid Dynamic modelling. The engine type is a low-cost solution countering the financial challenges of powertrain duplication evident with Hybrid Electric and Range Extender Electric Vehicles.

Keywords: hydrogen vehicle; hybrid electric vehicle; range extender; stepped piston engine; two-stroke cycle

1. Introduction

Battery Electric Vehicles (BEVs) are perceived to be the solution for future low environmental impact transport. However serious problems and challenges remain for BEVs. Range anxiety is a particular problem for adoption of potential new BEV owners as has been discussed by Rauh et al. [1], Reitz et al. [2] and Pevec et al. [3]. The impact on battery life when deep discharge of the vehicle battery system occurs also compounds this problem. Whilst a BEV may have a claimed range, repeated extreme depletion of the state of charge will cause rapid need for replacement of the battery. Furthermore, extreme ambient weather conditions have serious effects on a BEVs useful range adding to the anxiety of BEV users.

BEVs are ideally suited to inner city use and short-range journeys. Development of new battery storage systems is of course a major focus for new BEVs but currently the available range is insufficient for long distance travel. The replacement of EV battery systems is often down played and the fact that the battery pack is a complex device containing rare earth materials means that the cost of changing the battery is prohibitive. The battery system in a 100% electric EV is a large volume unit containing harmful materials as discussed by Sobianowska-Turek et al. [4]. It is not uncommon for EV Batteries to contain, Lithium, Cobalt, Nickel, Manganese and Rare Earth materials as reported by Lipman and Maier [5]. Careful recycling is therefore essential with such materials, not least care in the mining processes to acquire the original raw elements.

A challenging but solvable problem for EV adoption is to use cleaner energy sources. Unfortunately, much of the electricity generated is from fuels that are still carbon based. Coal and gas fired power stations are still predominant in many parts of the World. Essentially, until the transition to clean energy production is achieved, the only thing that EV adoption has achieved is removal of localized tailpipe emissions. The harmful emissions have simply been transferred to the area where the power stations are cited. Unfortunately, the transfer of Oxides of nitrogen (NOx) emission to the coal fired power stations, even with the latest combined cycle technology, is predicted to be higher than can currently be achieved with the latest internal combustion engines as researched by Kalghatgi [6]. It should be stated that some localized harmful emissions do unfortunately still exist with a BEV. The mass of a BEV is appreciably higher than conventional vehicles due to the battery systems. Particulate emissions from BEV tyres and braking systems have been shown to be consequentially higher for BEVs as discussed by Requia et al. [7], Reitz et al. [2] and Klimenko [8]. The new legislation covered by the European Union [9] has imposed regulation of particulate emissions from tyre and braking systems as a source for this very reason.

Smarter thinking is required to transition the World into a cleaner future. Considering BEVs as the only answer is unwise at the present time. Range Extender Electric Vehicles (RE-EVs) and Hybrid Electric Vehicles (HEVs) have a strong part to play as the cleaner energy future develops. RE-EVs and HEVs require smaller batteries than comparable 100% electric BEVs. This means that less material and battery volume is required. There are challenges due to powertrain duplication but if low-cost engine technology can be successfully applied then the increased cost caused by the duplicity can be countered. Furthermore, if clean fuels such as hydrogen [10] or e-fuels as discussed by Ravi et al. [11,12] are available for the onboard combustion engine of the HEV or RE-EV then any negative environmental impact from that source of the vehicle can be minimized or in some cases even eliminated.

If the negative impact of increased vehicle mass is to be addressed by the use of HEVs and RE-EVs then the engine system providing the recharging facility needs to be ideally of minimum mass. Dedicated spark ignition gasoline power plants have been considered for RE-EVs as evidenced by the research of Bassett et al. [13]. Advanced methodologies have also been explored for compression ignition diesel engines for HEVs in terms of engine operational parameters (variable compression ratio and injection timing), material tribological considerations [14–16] and use of lubricant nanoparticles to reduce friction and emissions [17]. Research has also focused on improving the emissions of compression ignition engines via natural gas operation [18]. In order to minimize internal combustion engine mass, the two-stroke cycle engine offers significant advantages over the four-stroke engine. Two-stroke engines have been developed to operate on hydrogen. The first engine to be developed for hydrogen fuel in 1860 was a two-stroke engine, based on the research of Etienne Lenoir [19], who generated the fuel by water electrolysis. More recent hydrogen two-stroke engine developments are exampled by the research of Furuhama and Kobayashi [20] and via the work of Caprioli et al. [21], Mattarelli et al. [22] and Volza et al. [23].

Hydrogen offers significant advantages over conventional fuels used within internal combustion engines. Notwithstanding the fact that hydrogen has to be created if it is to be used as a fuel, the fact that it contains no carbon means that the historic problematic emissions of unburned hydrocarbons, carbon monoxide and carbon dioxide are removed from the combustion challenge. The range of flammability of hydrogen is wider than that achievable with gasoline fuel as discussed by Karim [24]. This essentially means that lean air: fuel mixture operation is possible with hydrogen. Furthermore, hydrogen flame speeds are faster than those observed with gasoline as has been discussed by Verhelst and Turner [25], Shinde and Karunamurthy [26], Cracknell et al. [27] and Onorati et al. [28].

Oxides of nitrogen (NOx) form the significant noxious gas emission that still remains with internal combustion of hydrogen. Two-stroke engines have repeatedly demonstrated low NOx emissions on gasoline [29,30] and diesel fuels when compared with comparable four-stroke engines and therefore present an attractive starting place in order to minimize this remaining emission group. Indeed, taking advantage of the wide flammability range of hydrogen and hence possibilities for lean air: fuel mixture operation means that the NOx levels can be reduced to very low levels. Unfortunately, conventional crankcase scavenged two-stroke engines suffer from relatively low durability due to their inherent design configuration and construction. The simplest forms of the crankcase scavenged two-stroke engine mix oil with the fuel or use a precision metering pump to supply the lubricant. All of this supplied oil is consumed on a total loss basis, creating significant negative impact on their emissions characteristics. However, a two-stroke engine that has repeatedly shown significantly higher durability, comparable with four-stroke engine standards, is offered by the stepped piston engine. This engine design operates on neat fuel with no added oil completely separating the lubrication system from the air scavenging path, thereby overcoming the problems of conventional crankcase scavenged two-stroke engines. The critical areas of the engine requiring lubrication such as the piston and rings are lubricated discretely with metering holes allowing oil from the sump to reach the crucial areas strategically. This has resulted in significant reductions in oil consumption when compared with conventional crankcase scavenged engines [31].

Historically achieving low emission levels with conventional two-stroke engines has been difficult. This is due to the relatively high oil consumption of conventional engines and the fact that short-circuiting of the incoming air: fuel charge into the exhaust can occur during the open port phase of the cycle around bottom dead centre. However, the advent of fuel injection directly into the combustion chamber has shown significant improvements in emissions reduction as demonstrated by the research of Duret et al. [32], Schlunke [33], Shawcross et al. [34] and more recently via the research of Turner et al. [29] and Blundell et al. [30]. Essentially direct injection (DI) allows fuel delivery to be achieved without short-circuiting, thereby greatly reducing emissions. Two-stroke engines have always exhibited low NOx emission even without DI due to the low temperature and pressure of two-stroke combustion when compared with four-stroke engines. The stepped piston engine also retains the two-stroke cycle characteristic of emitting low NOx emission [35,36].

Hydrogen fuel operation of engines has been reported to create corrosion problems as discussed by Stępień [37]. Crankcase scavenged two-stroke engines utilize the underside of the piston as a scavenge pump. Corrosion issues would be very problematic to such engines due to the fact that the crankcase houses crucial bearings and other components that could suffer from exposure. Furthermore, crankcase scavenged engines are not ideally suited to gaseous fuel operation. For this research study a segregated scavenge two-stroke engine is required and the proposed solution is offered by an engine using two diameter or stepped pistons [35]. Stepped piston engines have previously shown good results operating on gaseous fuels as indicated from a 500 cm^3 stepped piston engine loaned to British Gas in the UK for experimentation using natural gas as a fuel. Conclusions from that work suggested that future hydrogen operation could be beneficial.

This paper builds upon prior experimental and 1-d computational fluid dynamic (CFD) work, investigating improvements to the CFD models to better correlate with the experimental stepped piston engines and initial consideration of the possible benefits of hydrogen fuel operation.

2. Materials and methods

2.1. Fuel properties

Properties for the fuels relevant to this research study are presented for reference in **Table 1**.

Table 1. Physical and chemical fuel properties.

| Property		Hydrogen	Indolene	95RON Gasoline
Research octane number		130	96.7	95.6
Lower heat value	(MJ/kg)	121	43.1	43.2
Flammability limits	(% by vol)	4–75	1.1–6.0	1.2–6.0
Stoichiometric air: fuel ratio AFRs		34.3	14.7	14.7
Composition (atoms per molecule)				
Carbon		0	7.8	~8
Hydrogen		2	13.2	~15
Oxygen		0	-	-
Nitrogen		0	-	-

2.2. Stepped piston segregated scavenge engines

The engine used as the basis of the study is a twin cylinder engine of 290 cm^3 swept volume, manufactured by Bernard Hooper Engineering Ltd, UK. The engine is effectively half of a SPV580 unmanned aerial vehicle (UAV) engine [35,38] using two cylinders instead of the four employed in the larger engine. The two-cylinder engine is designated UMA290 [39]. The V-4-cylinder SPV580 UAV engine has been developed to produce in excess of 61 kW/litre at 5250 rpm (gasoline version) to date [36,40]. For reference a production version of the parallel twin cylinder UMA290 engine can be seen in **Figure 1**.
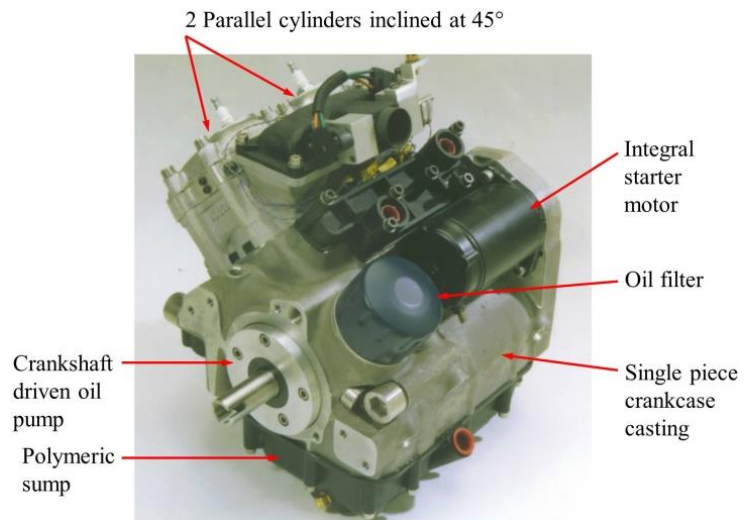
Figure 1. UMA290 290 cm³ twin cylinder stepped piston engine.

The method of operation of the UMA290 is described by the operating principle of the stepped piston crossover system (SPX system) in **Figure 2**.
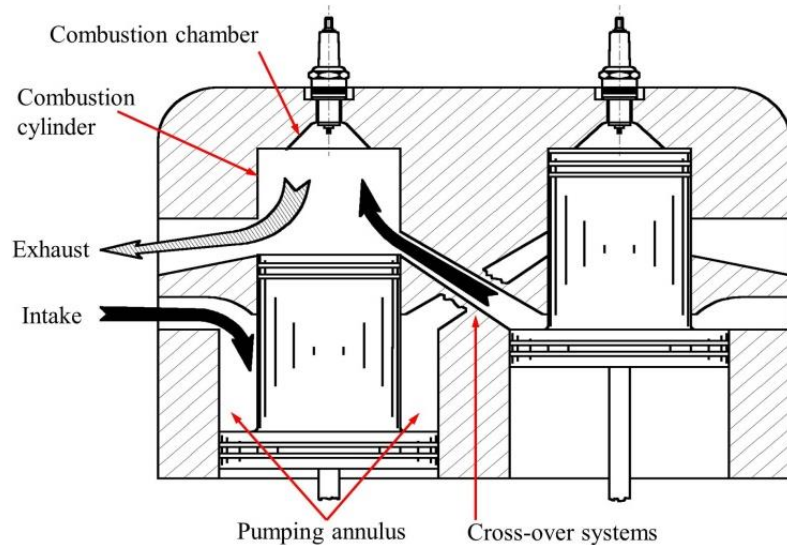

Figure 2. SPX engine operating principle (schematic representation of cross-over).

The SPX crossover system is employed on the majority of the multi-cylinder stepped piston engines such as the SPV580 and UMA290. It is however quite possible for single- and three-cylinder configurations to function. As can be observed from **Figure 2**, the cylinders of the UMA290 function in pairs. The air charge is inducted by the larger diameter or pumping part of the one-piece piston via a non-return or reed valve as are commonly employed on crankcase scavenged two-stroke engines. With reverse flow prevented the charge passes into the crossover system, allowing transfer of the charge to pass to the relevant paired cylinder. The charge enters the combustion cylinders via transfer ports. Combustion is similar in many ways to Schnürle loop scavenged engines. After combustion the spent gases are scavenged from the upper cylinders via exhaust ports. It is possible to design stepped

piston engines as uni-flow configurations, using exhaust poppet valves in the cylinder head, however this naturally compromises the compactness of the power plant.

The stepped piston engine offers key advantages over normal two-stroke and four-stroke engines. A significant advantage when compared with conventional crankcase scavenged two-stroke engines lies in the provision of total separation of the lubrication and charge air induction processes. The lubrication system is very similar to that commonly found in four-stroke engines, being completely filtered and recirculatory, using plain hydrodynamic shell bearings. Two-stroke engines that use crankcase scavenging typically use rolling element bearings which are a significant cost and noise source giving detrimental NVH issues. Furthermore, when considering gaseous fuel operation more specifically, the isolation of combustion blow-by gases from the crankcase and therefore contamination of bearings, surfaces and lubricant, that create problems in conventional two and four-stroke engines is eliminated. Hydrogen fuelled engines have been reported to cause internal corrosion issues within engines as discussed by Stępień [37]. The isolation methods available within the segregated design of the stepped piston engine could offer significant advantage with respect to such corrosion problems.

A partial cross-sectional general arrangement of the UMA290 engine is presented in **Figure 3**.
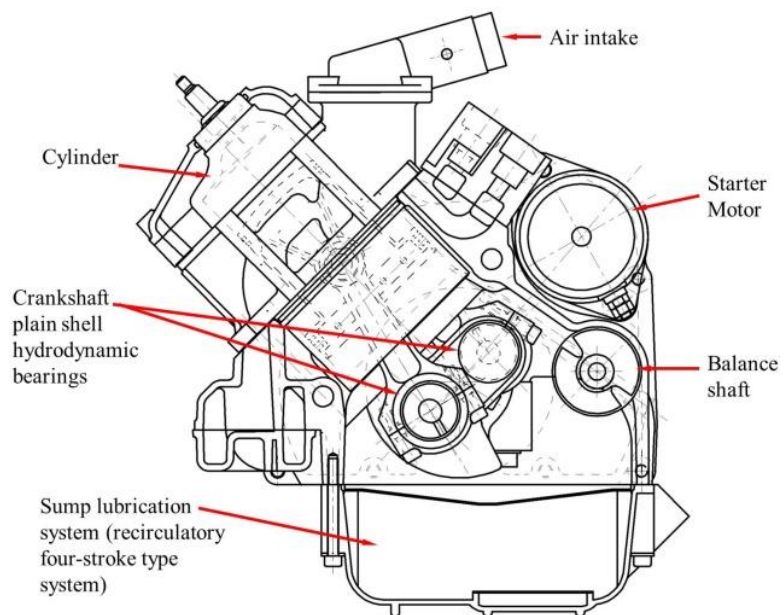
Figure 3. General arrangement of the UMA290 twin cylinder stepped piston engine.

The combustion cylinders of the engine shown in **Figure 3** each have a swept volume of 145 cm^3. The cylinders are of individual unit design with the pumping cylinders housed inside the crankcase. The crossover systems also form part of the crankcase. **Figure 4** displays a comparison of the port belt area of a conventional Schnürle loop scavenged engine and the same swept volume unit if scavenged by stepped pistons.

The cylinders are aluminium (Al Si7 Mg0.5) with both bores coated with a nickel silicon carbide coating (GILNISIL) applied by Gilardoni Vittorio S.r.l., Italy.

The pistons are low pressure die-cast using a high silicon aluminium alloy (Al Si18 Cu Mg Ni).
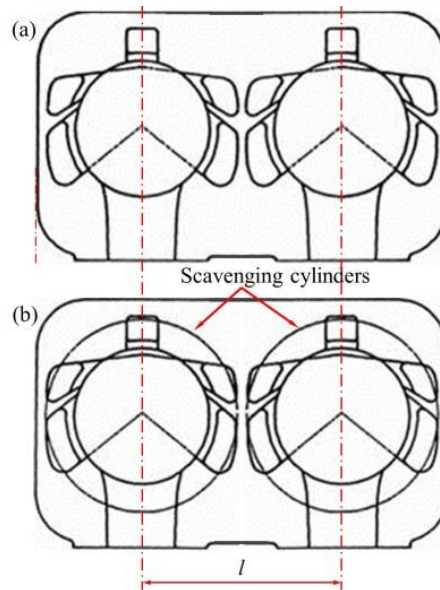
Figure 4. Two-stroke engine port layout comparison using identical bore diameter and swept volume **(a)** Schnürle loop scavenge; **(b)** Schnürle loop stepped piston segregated scavenge engine.

Naturally a stepped piston, by virtue of its design, will possess a greater plan profile than a conventional single diameter piston displacing the same swept volume. However, if we consider cylinder centre distance, *l*, it can be seen from close examination of **Figure 4** that the larger diameter pumping piston does not actually increase the engine cylinder spacing when compared with a conventional loop scavenged engine. The space required for the conventional engine's transfer ports typically expands the cylinder centre distance, *l*.
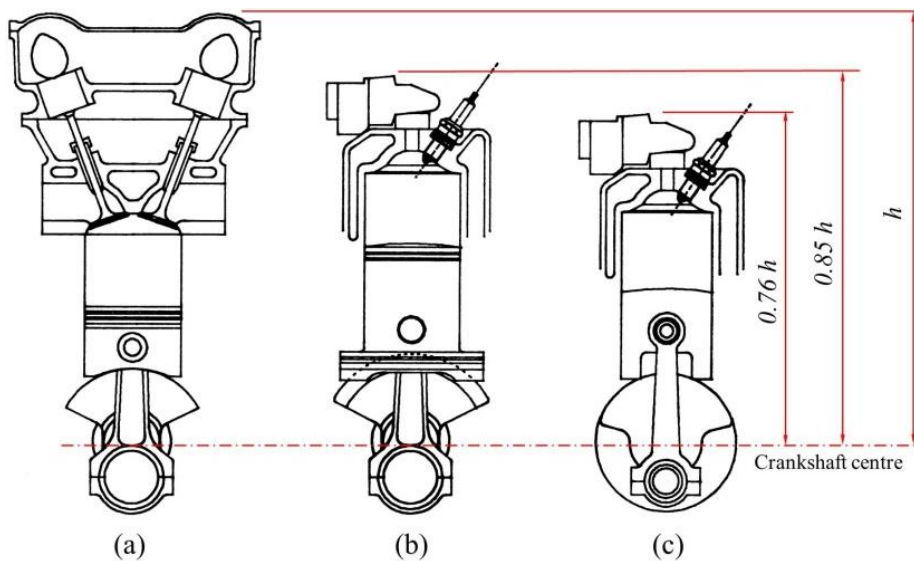
Figure 5. Engine height comparisons with identical swept volumes **(a)** DOHC four-stroke; **(b)** stepped piston; **(c)** conventional crankcase scavenged two-stroke engines.

The analysis shown in **Figure 5** is based upon identical cylinder swept volumes for each engine type. If the operational maximum power speed is also set as a constraint, the four-stroke engine would have to be larger to achieve the same power output. From **Figure 5** it can be seen that the stepped piston engine is smaller than the four-stroke engine but not quite as compact as a conventional crankcase scavenged two-stroke engine in terms of engine height.

The UMA290 engine was mounted on a dynamometer to establish baseline experimental data using 95RON gasoline as shown in **Figure 6**.
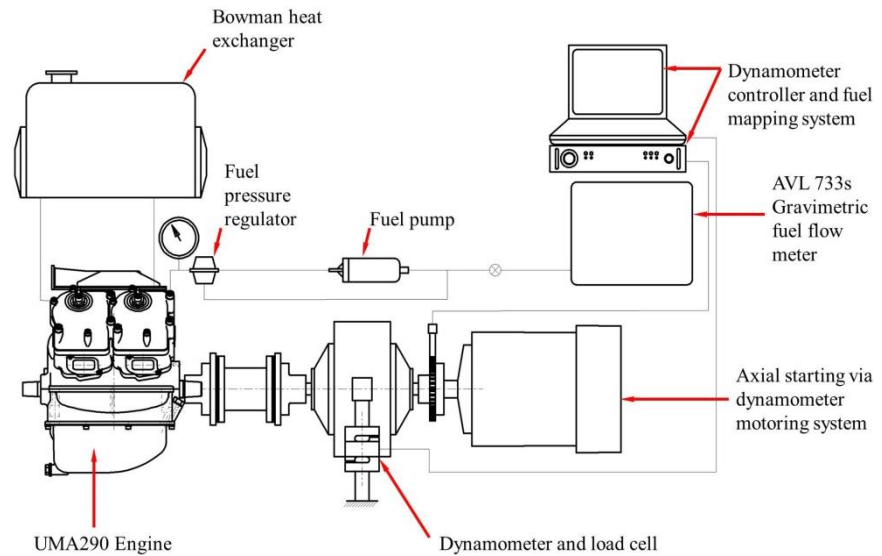
Figure 6. Schematic of UMA290 engine dynamometer test facility.

Experimental test results secured from the UMA290 engine were recorded using a Froude eddy current dynamometer equipped with a load cell. Fuel injector pulse width and ignition timing was mapped using a computer driven interface linked to the writable engine electronic control unit. A Hall effect sensor provides timing reference from the engine crankshaft and subsequent injector sequencing with timing variable via the PC interface. The system also has air temperature, coolant temperature, barometric pressure, throttle position and air mass flow sensors. The fuel flow was monitored using an AVL 733s gravimetric fuel balance. All test data reported in this paper was recorded at full load wide open throttle operating conditions at stoichiometric air: fuel ratio.

2.3. Modelling methodology

Details of the design of the UMA290 and a comparable four-stroke engine of 374 cm^3 capacity are listed for reference in **Table 2**.

Table 2. Engine design specification.

Engine		UMA290	4s 374
Operating cycle		2-stroke	4-stroke
Swept volume	(cm^3)	290	374
Scavenging system		Stepped piston	Naturally aspirated
Pump compression ratio		1.5	-

Table 2. (*Continued*).

| Engine		UMA290	4s 374
Cylinders		2	2
Bore	(mm)	62	62
Stroke	(mm)	48	62
BMEP	(bar)	7.3	12.1
Maximum BMEP speed	(rpm)	4500	4000
Compression ratio		6.2:1	10:1
Specific power	(kW/l)	58.4	60.7
Maximum power speed	(rpm)	5000	6000

(All performance data is at full load stoichiometric wide open throttle operating conditions)

2.3.1. Computational engine modelling

The Computational fluid dynamics (CFD) models adopted a parent-child simulation where the boundary conditions and flow data are exchanged between the models. The pumping cylinders and associated inlet passageways form the basis of the parent model. The child model comprises the crossover systems, combustion cylinders and exhaust system of the UMA290 engine. The 1-d CFD code, WAVE (version 2023.1), developed by Realis Simulation/Ricardo [41] was used for all simulations reported in this research study. Statistical methods developed by Gajević et al. [42] were used in order to process test results. The UMA290 parent and child stepped piston model layouts are shown in **Figures 7** and **8** respectively.
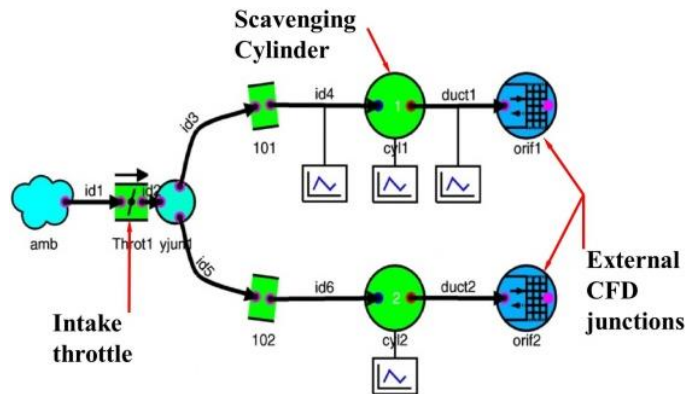

Figure 7. UMA290 Engine 1-d CFD model (parent model).
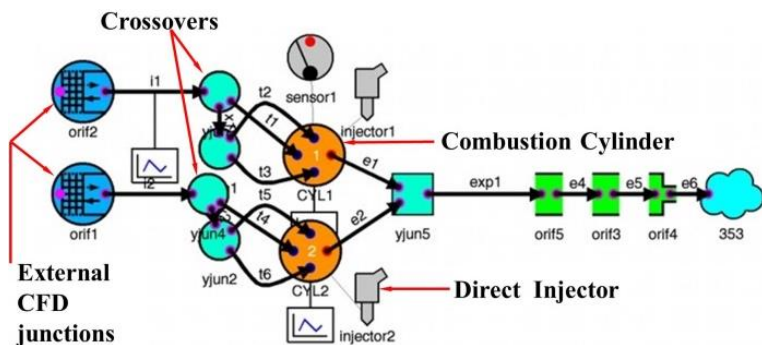
Figure 8. UMA290 Engine 1-d CFD model (child model).

Boundary conditions and mass flow data is exchanged between the parent and child models via the external CFD junction.

The WAVE model built to establish data from a comparative 374 cm^3 twin cylinder four-stroke engine, reflecting the data shown in **Table 2**, is displayed in **Figure 9**.
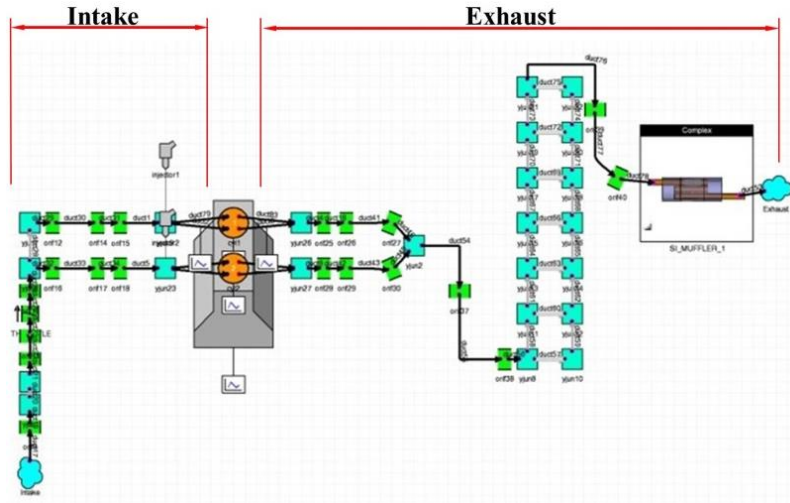
Figure 9. 374 cm^3 Four-stroke cycle engine 1-d CFD model.

2.3.2. Model theory

The construction of the WAVE models is essentially a collection of interconnected pre-defined elements of ambients, throttles, ducts, junctions and valves ultimately linking to combustion cylinders, and in the case of the UMA290, pumping cylinders. Each element is user defined in terms of dimensions, surface roughness and thermodynamic/heat transfer properties. The engine passageways are represented by ducts and are discretized as predefined elemental cells. At the centre of each individual cell calculations of instantaneous pressure and temperature are made whilst at the boundary points of each cell flow velocity and mass flowrate are computed. Equations (1)–(3) are used to compute conservation of mass, energy and momentum respectively:

$$\frac{\partial \rho}{\partial t} + \frac{\partial (\rho u)}{\partial x} = 0 \tag{1}$$

$$\frac{\partial (\rho u)}{\partial t} + \frac{\partial (\rho u^2 + P)}{\partial x} = \frac{\partial}{\partial x}\left(\frac{4\mu}{3}\frac{\partial}{\partial x}\right) \tag{2}$$

$$\frac{\partial (\rho e_T)}{\partial t} + \frac{\partial (\rho u e_T + Pu)}{\partial x} = \frac{\partial}{\partial x}\left(\frac{4}{3}\mu u \frac{\partial u}{\partial x} + k \frac{\partial T}{\partial x}\right) \tag{3}$$

Two-stroke engines require a means of inlet flow control. These can be one or more of the following:
1) Piston-port control
2) Rotary valve
3) Reed valve

Piston-porting is essentially control of the inlet flow via the engine's piston

passing over the inlet ports at the correct required time. Rotary valves can be disc or cylindrical elements driven by the engine allowing synchronized opening and closing of the inlet passages supplying the engine. The final choice is the reed valve. This is an automatic non-return valve designed with petals or reeds that are light enough to respond to the pressure drop across the valve block. Combinations of the above have been successfully applied such as the application of reed valves and piston-port control by Yamaha via the research of Hata et al. [43].

The UMA290 engine uses two individual reed valve blocks located within the inlet tract of each pump cylinder. However stepped piston engines, developed to date, have employed each of the three possible forms of inlet control. The reed valves employed comprise two sets of interconnected phenolic resin petals located on each side of a triangular prism shaped reed block. Within WAVE the reeds of the reed valves are modelled as light cantilevers based upon the reed's natural frequency and fundamental modes of vibration (lower order modes). The theory can be examined for reference via the research of Hinds [44] and Morrison and Crossland [45].

After passing through the reed valves the air is drawn into the individual pumping cylinders. The reed valves prevent reverse flow and the charge is passed to the external CFD junctions shown in **Figure 7** for exchange to the relevant linked junction in **Figure 8**. The crossover is represented by defined ducts replicating the passageways used that link to the cylinder transfer ports. Once within the cylinder the combustion is modelled using a Wiebe function as defined by the formula shown in Equation (4).

$$x(\theta) = 1 - exp\left[-\left[\frac{c(\theta - \theta_0)}{\Delta\theta_b}\right]^{-b}\right] \tag{4}$$

Equation (4), was developed by Wiebe [46] to compute the mass fraction burned, $x(\theta)$, as the combustion process incrementally progresses. Constants, b and c, are selected in order to replicate the actual combustion profile. It is possible to generate a representative Wiebe function from actual engine cylinder pressure data. However, in the absence of any available data for the UMA290 the prior research of Heywood and Sher [47] was explored. Above the crown of the combustion piston, the stepped piston engine is similar in many ways to the environment found above the piston crown of a crankcase scavenged two-stroke engine. Through analysis of crankcase scavenged two-stroke engines, values of $b = 5$ and $c = 3$ to 3.2 were derived by Sher [48]. These values have been used in order to generate the Wiebe function within the WAVE models developed within this research study. The prior research of Heywood and Sher [47] and Sher [48] considered gasoline fuel. This has been used to try to improve the correlation of the indolene fuelled stepped piston two-stroke models.

One of the biggest variables in engine modelling is often found in the representation of how heat transfer occurs within the actual engine and its representative model. Away from the cylinder the Colburn analogy [49] is used to compute the coefficient of heat transfer, h, as defined by Equation (5).

$$h = \frac{C_f}{2}\rho U c_p Pr^{-\frac{2}{3}} \tag{5}$$

In the area of the combustion cylinder the well-established analysis developed by Woschni [50] was used where the coefficient of heat transfer, *h*, is computed from Equation (6).

$$h = 0.0128\, D^{-0.2} P^{0.8} T^{-0.53} v_{ch}{}^{0.8} C_m \tag{6}$$

A key input to Equation (6) is the scaling factor, C_m. This value defines the surface area ratio of the piston crown and combustion chamber profile. A value of $C_m = 1$ defines the piston as a flat top or a flat combustion chamber. C_m is therefore set to reflect the increased surface area of the actual piston and/or cylinder head profile. For the UMA290 $C_m = 1.267$. The characteristic gas speed, v_{ch}, equates to the engine mean piston speed. *P* and *T* are the instantaneous cylinder pressure and temperatures respectively.

Engine friction is accounted for in the WAVE models via inputs to the correlation developed by Chen and Flynn [51] and reproduced for reference in Equation (7).

$$p_f = c_1 + c_2(p_{max}) + c_3\left(N\frac{s}{2}\right) + c_4\left(N\frac{s}{2}\right)^2 \tag{7}$$

Data from motored friction tests or Morse tests (in the case of the UMA290) can be used as input values influencing the computation of friction mean effective pressure, p_f, in Equation (7). Essentially the values of constants, c_1 to c_4, are adjusted until the FMEP replicates the data recorded from the real engine. The engine stroke is defined by the variable, s, in Equation (7), the engine speed is represented by *N* and p_{max} is the maximum cylinder pressure.

In order to predict the onset of combustion knock within the models, the induction time correlation developed by Douaud and Eyzat [52] is used. At each time step the knock intensity is reported, flagging that knock is occurring during the model runs. The induction time or ignition delay, τ, is computed at each time step in accordance with the formula shown in Equation (8).

$$\tau = 0.01869 A_p \left(\frac{O_N}{100}\right)^{3.4017} p_{cyl}{}^{-1.7} exp\left(\frac{3800/A_T}{T_{unb}}\right) \tag{8}$$

The octane number of the fuel, O_N, is a critical input value for Equation (8) and is defined for the fuel selection within the WAVE model. The variables A_p and A_T are user defined in relation to activation temperature. The cylinder pressure at the relevant point in the cycle is defined by p_{cyl} and the temperature of the unburned gas fraction within the cylinder is defined by T_{unb}. The user is informed when knock is detected within the model. The induction time, τ, reduces as the cycle progresses with a corresponding increase in temperature within the unburnt fuel mixture. Auto ignition within the model will be evident when the condition of Equation (9) reaches unity.

$$\int_{t_0}^{t_i} \frac{d\tau}{\tau} = 1 \tag{9}$$

3. Results and discussion

Results

All experimental test data was corrected for standard atmospheric conditions to SAE Standard J1349 [53]. Dynamometer tests were all performed with 95RON gasoline. WAVE modelling was performed via optimisation methods for both the stepped piston engine (UMA290) and four-stroke engine (4s 374) models. The UMA290 models are further developments of prior work [36]. This development work focused on indolene fuel. Indolene is a reference fuel similar to gasoline. Gasoline varies around the world, and indeed from state to state in the USA. Indolene is a reformulated form of gasoline with additives to stabilize the fuel, thereby providing better repeatability than standard pump gasoline.

Engine performance data is compared for UMA290 engine and four-stroke engine models in **Figures 10** and **11**. No combustion knock was observed for any of the model runs using indolene presented within this paper. For reference in **Figures 10** and **11**, dynamometer 95RON gasoline test data from an experimental UMA290 engine is shown.
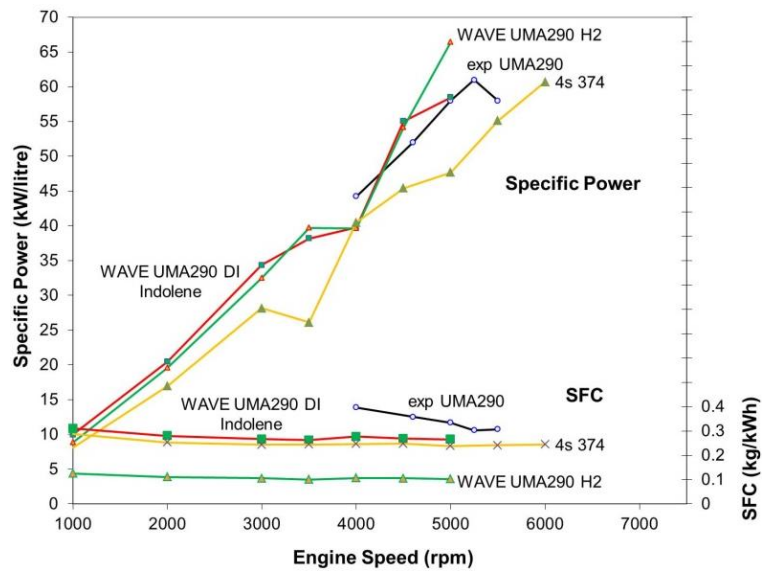

Figure 10. Comparison of specific power and specific fuel consumption using 95RON Gasoline or Indolene as a fuel.

The WAVE modelling so far has indicated an improved maximum specific power for the UMA290 stepped piston engine of 58.4 kW/litre at 5000 rpm. The equivalent experimental stepped piston engine output is currently up to 61.1 kW/litre at 5250 rpm [35] operating on 95RON gasoline. The improvement in the models using indolene can now be seen to be providing closer correlation than was achieved in previous modelling results. The four-stroke 374 cm^3 engine (designated 4s 374 in **Figure 10**) was modelled to achieve a specific output of 60.7 kW/litre at 6000 rpm.

The specific fuel consumption results have indicated a minimum SFC of 0.262 kg/kWh at 3500 rpm and 0.265 kg/kWh at 5000 rpm. The experimental UMA290 engine achieved 0.303 kg/kWh during dynamometer tests at 5250 rpm. Modelling of the four-stroke comparator 4s 374 engines indicated a minimum of 0.240 kg/kWh at

5000 rpm.
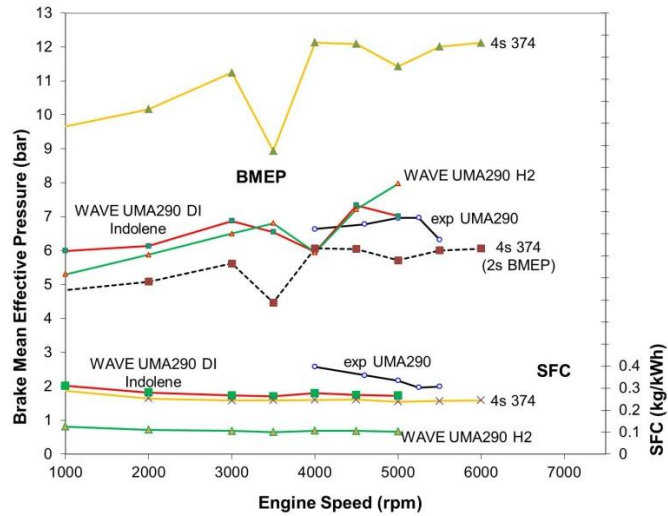
Figure 11. Comparison of modelled brake mean effective pressures using 95RON gasoline or indolene fuel.

In terms of brake mean effective pressure, the four-stroke engine maximum performance equates to a BMEP of 12.13 bar at 4000 rpm using indolene fuel. The UMA290 engine's maximum BMEP can be seen to occur at 4500 rpm with a magnitude of 7.34 bar. During dynamometer testing the experimental UMA290 achieved a level of 6.97 bar at 5250 rpm.

The dashed line shown in **Figure 11** shows the equivalent two-stroke BMEP levels for the 4s 374 engine. Inflection points can be observed for both engine models in **Figures 10** and **11**. These appear at 3000 rpm for the four-stroke 4s 374 engine and at 4000 rpm for the UMA290 engine. Both models were subject to optimisation efforts in order to try to investigate these inflections. This work resulted in making them less pronounced but it was not possible to remove them without significant effect on the maximum power level.

In **Figure 12** modelled cylinder pressure for the indolene fuelled WAVE models are displayed at 3000 rpm.
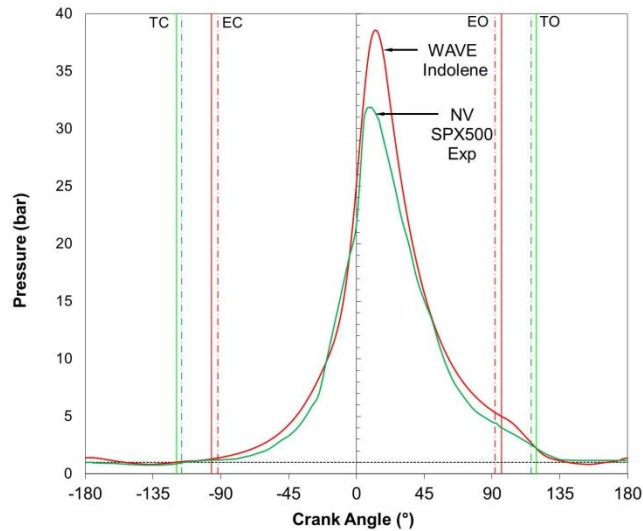
Figure 12. Comparison of modelled cylinder pressures using gasoline and indolene fuels.

A stepped piston motorcycle and single cylinder industrial engines were developed at Norton Villiers via the research of Hooper and Favill [54]. The NV SPX500 Exp curve presented in **Figure 12** is taken from experimental test engine data from that research. Added data shown in **Figure 12** has been taken from the WAVE models created during the more recent research study. The port timings are indicated by the vertical TC, EC, TO and EO lines, denoting the exhaust (E) and transfer (T) port closure (C) and opening (O) points.

Figures 13 and **14** display gas dynamic and mass flow computations for the UMA290 engine models. In each case data from the current study are compared with earlier research data.
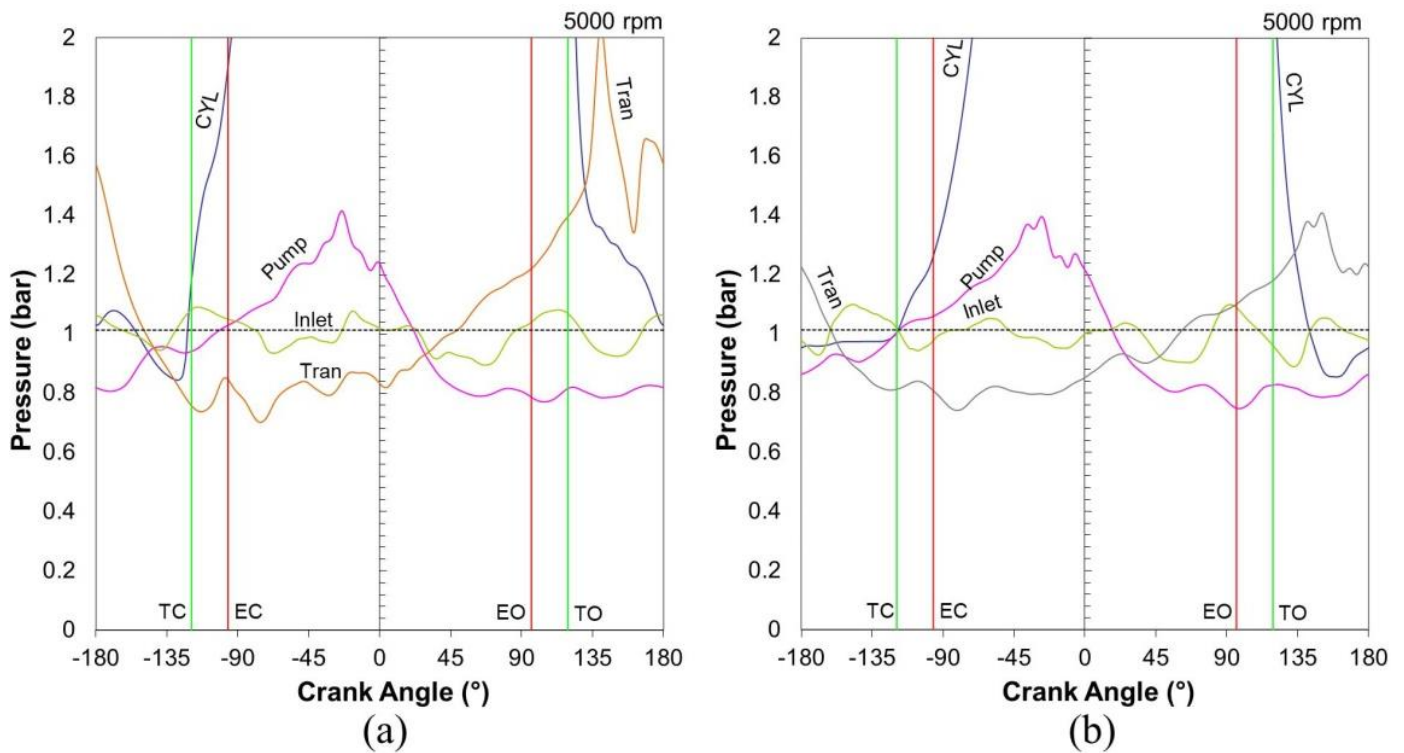
Figure 13. Gas dynamic analysis of UMA290 engine operating on indolene **(a)** UMA290 (2024); **(b)** UMA290 (2017) [36]–5000 rpm.

Data from the recent research study is shown in **Figure 13a** with the model data from prior work shown for comparison in **Figure 13b**. The higher rate of cylinder pressure rise can be seen in **Figure 13a**. Also, the greater transfer port pressure can also be seen as a significant improvement over **Figure 13b**. This higher pressure is evident in the indolene fuelled models and explains the increased performance achieved since the earlier research reported.
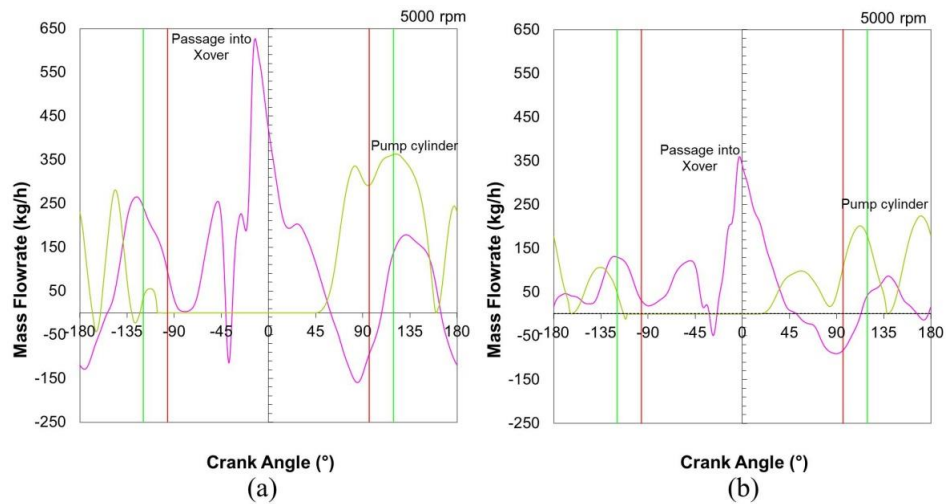
Figure 14. Mass flow through inlet and crossover systems of UMA290 **(a)** UMA290 (2024); **(b)** UMA290 (2017) [36]–5000 rpm.

The mass flow data shown in **Figure 14a** relates to the most recent research with the earlier model data being displayed in **Figure 14b**. Whilst a greater level of negative flow can be seen in **Figure 14a** when compared with **Figure 14b**, the overall increase in positive mass flow towards the combustion cylinders is also clearly evident. As for the increased pressures seen in **Figure 13a**, the improvement in mass flow of the air charge supports the observed performance improvements achieved in the current research using indolene fuels.

Actual pumping cylinder pressure data from other stepped piston engines is presented in **Figure 15** to provide a cross comparison with the WAVE model data recorded from the indolene fuelled models.
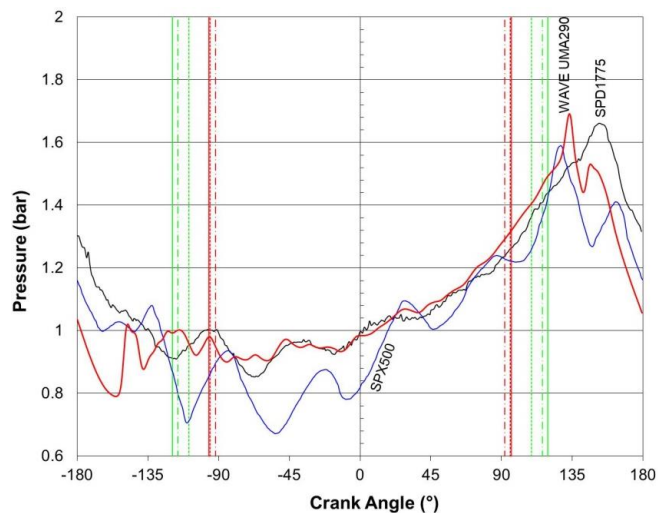
Figure 15. Pumping cylinder pressure for stepped piston prototype engines and WAVE model data.

The experimental engine data shown in **Figure 15** was recorded from an SPX500 engine and an SPD1775 engine. The SPX500 was the engine developed for the Norton Wulf motorcycle. The data was recorded at Norton Villiers during development of the engine. The SPD1775 is a 4-cylinder compression ignition

stepped piston engine of 1775 cm^3 swept volume. This engine data, recorded at 3000 RPM, is included purely for comparative purposes. All of the engines shown in **Figure 15** use reed valve-controlled induction systems. The transfer and exhaust port timings are shown for reference in **Figure 15** for the UMA290 (solid lines), SPX500 (chain dash lines) and SPD1775 (dashed lines).

4. Discussion

The UMA290 has been the subject of previous research studies [36]. The work in this phase of research has improved the performance of the original indolene models, improving the correlation with the real engine prior to future planned work using hydrogen fuel. The maximum specific power at 5500 rpm was 49 kW/litre which was below the performance levels observed during dynamometer testing of the experimental UMA290 engine using 95RON gasoline. Observations from the latest research reported here has achieved a higher maximum specific power level at 5000 rpm of 58.4 kW/litre. Despite this 24.3% performance improvement the results are still lagging the experimental engines (achieving 61.1 kW/litre at 5250 rpm) by 4.6%. The 374 cm^3 twin cylinder four-stroke engine achieved a modelled output at 6000 rpm equating to 60.7 kW/litre.

The comparative brake mean effective pressures showed a maximum BMEP of 12.13 bar at 4000 rpm for the 374 cm^3 four-stroke engine, whilst the UMA290 maximum BMEP was observed at 4500 rpm with a level of 7.34 bar using indolene. It should of course be remembered that the UMA290 is a two-stroke cycle engine. The SPV580 stepped piston engine which is in simple terms two UMA290 units has been tested on 95 RON gasoline to a maximum BMEP of 6.97 bar at 5250 rpm.

Specific fuel consumption data recorded during the current research has indicated a minimum WAVE modelled full load SFC of 0.262 kg/kWh at 3500 rpm using indolene WAVE models. Closer correlation with the experimental results has been observed in terms of SFC. The experimental UMA290 operating on 95RON gasoline returns 0.303 kg/kWh at 5250 rpm. This compares more closely than in prior studies with WAVE modelled values of 0.298 kg/kWh at 5500 rpm and 0.265 kg/kWh at 5000 rpm. The minimum modelled indolene SFC observed for the four-stroke 374 cm^3 engine was 0.240 kg/kWh at 5000 rpm.

With the ultimate objective of development of a HEV or RE-EV achieving ultra-low environmental impact initial modelling studies have explored lean operation on hydrogen. Indications are that almost zero emission operation may be possible. If possible, to be sustained, with such high air: fuel ratio operation, the engine could operate with extremely low environmental impact and maintain the state of charge of the vehicle battery system thereby countering the range anxiety problems still causing concern for BEVs. The low noise, vibration and harshness characteristics of stepped piston engines have already been presented [36]. Containment of a compact engine system within a semi-anechoic chamber would further reduce any remaining NVH challenges.

Engine production costs against comparable competing engines, whether of conventional two or four-stroke type, have consistently indicated significant savings. Studies against a direct injection four-stroke engine concluded that, on top of a 40%

investment cost reduction, a unit cost saving of 22% should be evident. Both the stepped piston and four-stroke engines were inline three-cylinder examples. The duplication of powertrain systems evident in HEVs and RE-EVs presents a serious challenge to product viability. Such significant engine cost reductions will naturally assist in overcoming this challenge.

Hydrogen fuelled engines have been shown to suffer from corrosion problems as has been discussed by Stępień [37] and Liu et al. [55]. The crossover system designed into stepped piston engines, to enable operation, is expected to offer advantage in countering the potential corrosion issues. The crossover essentially provides charge isolation from the moving mechanical components. The passageways forming the crossover systems are typically located within the crankcase casting and are completely separated from any other parts of the engine. This should provide additional protection from corrosion issues. Furthermore blow-by gases bypassing the combustion piston rings will only pass into the chamber system of the crossover rather than contaminating the areas of the engine that would suffer in conventional engines. Corrosion observed in other conventional hydrogen fuelled engines is not expected to present such problems with a stepped piston engine solution. The added advantages of two-stroke cycle operation, together with the complete separation of the lubrication methodology from the scavenging processes offers significant benefits in terms of durability, especially when compared with conventional two-stroke engines. Durability characteristics more typically associated with four-stroke engines has been regularly observed with stepped piston charged engines.

Exhaust gas recirculation (EGR) is inherent in two-stroke engines by virtue of their operating cycle. This occurs internally within the cylinder. External EGR could also be readily applied to the engine but has not yet been considered in the current research study.

Variable compression ratio technology, as demonstrated by the research of Turner et al. [29] and Blundell et al. [30] has been shown to offer further benefits in terms of performance and emissions reduction. This VCR technology could relatively easily be applied to the stepped piston engine due to the simplicity of the cylinder head and combustion chamber. Variable port timing methods could also provide further improvement, particularly away from the maximum power full load conditions. Variable port timing is also an effective method for providing an element of EGR control. No experimentation with VCR or variable port timing has been explored within this study but could provide a focus for further research.

5. Conclusion

Significant improvements to the simulated specific power and fuel consumption of the UMA290 stepped piston segregated scavenge engine have been presented operating on indolene/gasoline fuels. This research has been performed prior to planned hydrogen fuel modelling and operation to explore potential benefits of the engine type on low emission fuels for future HEVs or RE-EVs. Model predictions have indicated specific power output to date of 58.4 kW/litre using indolene compared with 61.1 kW/litre for the gasoline engine. The potential benefits, with

near zero emission operation possible, could counter the range anxiety still causing problems for electric vehicles. The approach should also counter the negative environmental impact that still exists for BEVs.

Conflict of interest: The author declares no conflict of interest.

Notation

A_p	Knock multiplier
A_T	Activation temperature multiplier
B	Constant
C_m	Relative area scaling factor for heat transfer
C	Constant
c_1, c_2, c_3, c_4	FMEP constants
D	Cylinder bore diameter
e_T	Internal energy
h	Coefficient of heat transfer
k	Coefficient of thermal conductivity
l	Cylinder centre distance
N	Engine speed
O_N	Fuel research octane number
P	Instantaneous gas pressure
p	Pressure
p_{cyl}	Cylinder pressure
p_f	Friction means effective pressure
p_{max}	Maximum cylinder pressure
S	Stroke
t_i	Auto ignition start time
t_i	Time at commencement of end gas compression
t	Time
T	Instantaneous gas temperature
T_{unb}	Unburned gas temperature
U	Velocity
v_{ch}	Characteristic gas velocity
$x(\theta)$	Mass fraction burned at crank angle θ
θ	Crank angle
θ_0	Crank angle at the start of combustion
$\Delta\theta_b$	Duration of combustion
ρ	Density
μ	Dynamic viscosity
τ	Induction time

Abbreviations

1-d CFD	One dimensional computational fluid dynamic
4s 374	Four-stroke twin cylinder 374 cm^3 engine
BEV	Battery electric vehicle
BMEP	Brake mean effective pressure
CA50	Crank angle position for 50% of mass fraction burned
DI	Direct injection
DOHC	Double overhead cam
EC	Exhaust port closure
EO	Exhaust port opening
FMEP	Friction mean effective pressure
HEV	Hybrid electric vehicle
IC	Internal combustion
NO_x	Oxides of nitrogen
NVH	Noise vibration and harshness
PPM	Parts per million
RE-EV	Range extender electric vehicle
SPV580	Stepped piston V-4 580 cm^3 engine
SPX	Stepped piston crossover system
TC	Transfer port closure
TDC	Top dead centre
TO	Transfer port opening
UMA290	Stepped piston twin cylinder 290 cm^3 engine

References

1. Rauh N, Franke T, Krems JF. Understanding the Impact of Electric Vehicle Driving Experience on Range Anxiety. Human Factors: The Journal of the Human Factors and Ergonomics Society. 2014; 57(1): 177–187. doi: 10.1177/0018720814546372

2. Reitz RD, Ogawa H, Payri R, et al. IJER editorial: The future of the internal combustion engine. International Journal of Engine Research. 2019; 21(1): 3–10. doi: 10.1177/1468087419877990

3. Pevec D, Babic J, Carvalho A, et al. A survey-based assessment of how existing and potential electric vehicle owners perceive range anxiety. Journal of Cleaner Production. 2020; 276: 122779. doi: 10.1016/j.jclepro.2020.122779

4. Sobianowska-Turek A, Urbańska W, Janicka A, et al. The Necessity of Recycling of Waste Li-Ion Batteries Used in Electric Vehicles as Objects Posing a Threat to Human Health and the Environment. Recycling. 2021; 6(2): 35. doi: 10.3390/recycling6020035

5. Lipman TE, Maier P. Advanced materials supply considerations for electric vehicle applications. MRS Bulletin. 2021; 46(12): 1164–1175. doi: 10.1557/s43577-022-00263-z

6. Kalghatgi G. Is it the end of combustion and engine combustion research? Should it be? Transportation Engineering. 2022; 10: 100142. doi: 10.1016/j.treng.2022.100142

7. Requia WJ, Mohamed M, Higgins CD, et al. How clean are electric vehicles? Evidence-based review of the effects of electric mobility on air pollutants, greenhouse gas emissions and human health. Atmospheric Environment. 2018; 185: 64–77. doi: 10.1016/j.atmosenv.2018.04.040

8. Klimenko A. Aggregated toxicity of road vehicles as basis for future regulation in the field of atmospheric air protection. SN Applied Sciences. 2020; 2(12). doi: 10.1007/s42452-020-03874-w

9. European Union. Available online: https://www.consilium.europa.eu/en/press/press-releases/2023/12/18/euro-7-council-and-parliament-strike-provisional-deal-on-emissions-limits-for-road-vehicles/ (accessed on 19 August 2024).

10. Sterlepper S, Fischer M, Claßen J, et al. Concepts for Hydrogen Internal Combustion Engines and Their Implications on the Exhaust Gas Aftertreatment System. Energies. 2021; 14(23): 8166. doi: 10.3390/en14238166

11. Ravi SS, Osipov S, Turner JWG. Impact of Modern Vehicular Technologies and Emission Regulations on Improving Global Air Quality. Atmosphere. 2023; 14(7): 1164. doi: 10.3390/atmos14071164

12. Ravi SS, Brace C, Larkin C, et al. On the pursuit of emissions-free clean mobility—Electric vehicles versus e-fuels. Science of The Total Environment. 2023; 875: 162688. doi: 10.1016/j.scitotenv.2023.162688

13. Bassett M, Hall J, Kennedy G, et al. The Development of a Range Extender Electric Vehicle Demonstrator. SAE Technical Paper Series. 2013. doi: 10.4271/2013-01-1469

14. Milojević, S., Savić, S., Mitrović, S., et al. Solving the Problem of Friction and Wear in Auxiliary Devices of Internal Combustion Engines on the Example of Reciprocating Air Compressor for Vehicles. Tehnicki vjesnik—Technical Gazette. 2023; 30(1): 122–130. doi: 10.17559/tv-20220414105757

15. Milojević, S., Savić, S., Marić, D., et al. Correlation between Emission and Combustion Characteristics with the Compression Ratio and Fuel Injection Timing in Tribologically Optimized Diesel Engine. Tehnicki vjesnik—Technical Gazette. 2022; 29(4): 1210–1219. doi: 10.17559/tv-20211220232130

16. Milojević S, Glišović J, Savić S, et al. Particulate Matter Emission and Air Pollution Reduction by Applying Variable Systems in Tribologically Optimized Diesel Engines for Vehicles in Road Traffic. Atmosphere. 2024; 15(2): 184. doi: 10.3390/atmos15020184

17. Bukvić M, Gajević S, Skulić A, et al. Tribological Application of Nanocomposite Additives in Industrial Oils. Lubricants. 2023; 12(1): 6. doi: 10.3390/lubricants12010006

18. Milojevic S. Sustainable application of natural gas as engine fuel in city buses: Benefit and restrictions. Istrazivanja i projektovanja za privredu. 2017; 15(1): 81–88. doi: 10.5937/jaes15-12268

19. Wróbel K, Wróbel J, Tokarz W, et al. Hydrogen Internal Combustion Engine Vehicles: A Review. Energies. 2022; 15(23): 8937. doi: 10.3390/en15238937

20. Furuhama S, Kobayashi Y. Hydrogen Cars with LH2-Tank, LH2-Pump and Cold GH2-lnjection Two-Stroke Engine. SAE transactions; 1982. pp. 1371–1383.

21. Caprioli S, Volza A, Mattarelli E, Rinaldini CA. High Performance and Near Zero Emissions 2-Stroke H2 Engine. SAE Technical Paper. 2023; 24: 0068.

22. Mattarelli E, Rinaldini CA, Marmorini L, et al. 2-Stroke RCCI Engines for Passenger Cars. Energies. 2022; 15(3): 1173. doi: 10.3390/en15031173

23. Volza A, Scrignoli F, Caprioli S, et al. Exploring the Potential of Hydrogen Opposed Piston Engines for Single-Cylinder Electric Generators: A Computational Study. SAE Technical Paper Series. 2023; 24: 128. doi: 10.4271/2023-24-0128

24. Karim GA. Hydrogen as a spark ignition engine fuel" (International Journal of Hydrogen Energy. 2023; 28(5): 569–577. doi: 10.1016/S0360-3199(02)00150-7

25. Verhelst S, Turner JWG. Hydrogen-Fueled Spark Ignition Engines. In: Tingas EA. (editor). Hydrogen for Future Thermal Engines. Green Energy and Technology. Springer, Cham; 2023.

26. Shinde BJ, Karunamurthy K. Recent progress in hydrogen fuelled internal combustion engine (H2ICE)—A comprehensive outlook. Materials Today: Proceedings. 2022; 51: 1568–1579. doi: 10.1016/j.matpr.2021.10.378

27. Cracknell R, Ciatti S, Dorofeev S, et al. Decarbonization of mobility, including transportation and renewable fuels. In: Proceedings of the Combustion Institute; 2023. pp.1–9.

28. Onorati A, Payri R, Vaglieco BM, et al. The role of hydrogen for future internal combustion engines. International Journal of Engine Research. 2022; 23(4): 529–540. doi: 10.1177/14680874221081947

29. Turner, J., Blundell, D., Pearson, R., et al. Project Omnivore: A Variable Compression Ratio ATAC 2-Stroke Engine for Ultra-Wide-Range HCCI Operation on a Variety of Fuels. SAE Paper. 2010; 1: 1249.

30. Blundell DW, Turner J, Pearson R, et al. The Omnivore Wide-range Auto-Ignition Engine: Results to Date using 98RON Unleaded Gasoline and E85 Fuels. SAE Technical Paper Series. 2010; 1: 0846. doi: 10.4271/2010-01-0846

31. Hooper PR. Low emission stepped piston engine for marine outboard motor application. In: Proceedings of the Institution of Mechanical Engineers; 2024.

32. Duret P, Ecomard A, Audinet M. A New Two-Stroke Engine with Compressed-Air Assisted Fuel Injection for High Efficiency low Emissions Applications. SAE Technical Paper Series. 1988

33. Schlunke K. (1989). The orbital combustion process engine. 10th Vienna Motorsymposium. VDI. 1989; 122: 63–68.

34. Shawcross D, Pumphrey C, Arnall D. A Five-Million Kilometre, 100-Vehicle Fleet Trial, of an Air-Assist Direct Fuel Injected, Automotive 2-Stroke Engine. SAE Technical Paper Series. 2000. doi: 10.4271/2000-01-0898

35. Hooper PR, Al-Shemmeri T, Goodwin MJ. Advanced modern low-emission two-stroke cycle engines. In: Proceedings of the Institution of Mechanical Engineers; 2011. pp. 1531–1543.

36. Hooper PR. Investigation into a stepped-piston engine solution for automotive range-extender vehicles and hybrid electric vehicles to meet future green transportation objectives. In: Proceedings of the Institution of Mechanical Engineers; 2017. pp. 305–317.

37. Stępień Z. A Comprehensive Overview of Hydrogen-Fueled Internal Combustion Engines: Achievements and Future Challenges. Energies. 2021; 14(20): 6504. doi: 10.3390/en14206504

38. Bernard Hooper Engineering Ltd. SPV580 engine data sheet. Available online: http://www.bernardhooperengineering.co.uk/spv580ds.htm (accessed on 28 September 2024).

39. Bernard Hooper Engineering Ltd. G290 engine data sheet. Available online: http://www.bernardhooperengineering.co.uk/g290ds.htm (accessed 28 September 2024).

40. Stone R. Introduction to Internal Combustion Engines, 4th ed. Macmillan Education UK; 2012.

41. Realis Simulation/Ricardo PLC. Available online: https://www.realis-simulation.com/products/wave/ (accessed on 20 August 2024).

42. Gajević S, Marković A, Milojević S, et al. Multi-Objective Optimization of Tribological Characteristics for Aluminum Composite Using Taguchi Grey and TOPSIS Approaches. Lubricants. 2024; 12(5): 171. doi: 10.3390/lubricants12050171

43. Hata N, Fujita T, Matsuo N. Modification of Two-Stroke Engine Intake System for Improvements of Fuel Consumption and Performance through the Yamaha Energy Induction System (YEIS). SAE Technical Paper Series. 1981. doi: 10.4271/810923

44. Hinds ET. Intake flow characteristics of a two-stroke cycle engine fitted with reed valves [PhD thesis]. Queen's University of Belfast; 1978.

45. Morrison JLM, Crossland B. An Introduction to the Mechanics of Machines, 2nd ed. Longman; 1971.

46. Wiebe I. Semi-empirical formula for combustion speed (German). In: Verlag der Akademie der Wissenschaften der UdSSR, Moscow; 1967.

47. Heywood JB, Sher E. The Two-Stroke Cycle Engine. Routledge; 2017.

48. Sher E. (1984) The Effect of Atmospheric Conditions on the Performance of an Airborne Two-Stroke Spark Ignition Engine. Proc. Inst. Mech. Eng. 1984; 198(15): 239–251.

49. Bird RB, Stewart WE, Lightfoot EN. Transport Phenomena, 2nd ed. Wiley; 2022.

50. Woschni G. A Universally Applicable Equation for the Instantaneous Heat Transfer Coefficient in the Internal Combustion Engine. SAE Technical Paper Series. 1967. doi: 10.4271/670931

51. Chen SK, Flynn PF. Development of a Single Cylinder Compression Ignition Research Engine. SAE Technical Paper Series. 1965. doi: 10.4271/650733

52. Douaud AM, Eyzat P. Four-Octane-Number Method for Predicting the Anti-Knock Behavior of Fuels and Engines. SAE Technical Paper Series. 1978. doi: 10.4271/780080

53. SAE Standard J1349. Engine Power Test Code—Spark Ignition and Compression Ignition—Net Power Rating. SAE International, Warrendale, PA; 1995.

54. Hooper B, Favill JE. Modern Stepped Piston Engines. In: Proceedings of Design and Development of Small IC Engines Conference; 31 May–2 June 1978. IMechE paper C133/78.

55. Liu Z, Guo Z, Rao X, et al. A comprehensive review on the material performance affected by gaseous alternative fuels in internal combustion engines. Engineering Failure Analysis. 2022; 139: 106507. doi: 10.1016/j.engfailanal.2022.106507.

Article

Implementation of a solar-thermal hybrid air conditioning system in Muscat for energy conservation

Muthuraman Subbiah[1,*], Saravanan Natarajan[1], Sivaraj Murugan[2], Kumar Ayyappan[3]

[1] Department of Engineering, University of Technology and Applied Sciences, Muscat 133, Oman

[2] Department of Mechanical Engineering, Rohini College of Engineering and Technology, Tamilnadu 629401, India

[3] Department of Applied Sciences, Amrita College of Engineering and Technology, Tamilnadu 629901, India

* Corresponding author: Muthuraman Subbiah, muthu9678@gmail.com

Abstract: The need for global energy conservation has become more urgent because of the negative effects of excessive energy use, such as higher fuel consumption, greater environmental pollution, and depletion of the ozone layer. There has been a significant increase in the demand for central and high-capacity household air conditioning systems in Muscat in recent years. The need for this is influenced by factors such as arid climate, increasing temperatures, air pollution, and population increase. As a result, there has been a significant increase in electricity use, putting a strain on power resources. To tackle this difficulty, the incorporation of solar collectors as supplementary thermal compressors in air conditioning systems offers a chance to utilise renewable energy sources. The objective of this hybrid technique is to enhance the effectiveness of cooling systems, hence minimising the need for electricity and lowering the release of environmental pollutants.

Keywords: solar energy; energy conservation; radiation; hybrid air conditioning; thermal energy

1. Introduction

The increasing need for air conditioning in Muscat is a result of the climate and fast urbanisation issues faced in the region. Elevated temperatures and atmospheric pollution require widespread reliance on air conditioning, resulting in heightened energy usage. This research suggests using solar-thermal technology in air conditioning systems as a solution to address these difficulties and improve energy efficiency. Muscat has consistently high temperatures throughout most of the year, resulting in a significant need for cooling and, thus, a huge need for energy [1]. Elevated temperatures and atmospheric pollution need the greater utilisation of air conditioning systems, resulting in heightened energy usage. Conventional air conditioning systems that rely only on electricity from the power grid make a substantial contribution to energy consumption and the resulting environmental effects.

Air conditioning (AC) is the process of regulating air properties, such as temperature, humidity, cleanliness, and distribution technique, to meet certain requirements [2]. Air conditioning, also referred to as the cooling of air, involves the removal of heat, which is usually accomplished using electricity. The installation of a solar energy system becomes appealing due to the rise in electricity consumption [3]. The renewable nature of solar energy makes it highly suitable for utilisation in sub-tropical nations. To tackle these difficulties, the suggested system combines solar collectors with air conditioning units to utilise renewable energy for the purpose of

cooling. Solar collectors capture thermal energy to enhance the compression process of the system. This strategy enhances cooling efficiency and minimises dependence on traditional electricity. The system, which provides comprehensive control over capacity, mechanism, ease of implementation, high reliability, silent operation, long lifespan, and low maintenance costs, is an excellent choice for using solar energy efficiently and cost-effectively in cooling applications [4].

The main objective of this project is to enhance and optimise the conventional air conditioning unit to function alongside solar energy as an auxiliary system, with the purpose of decreasing energy usage, environmental contamination, and noise levels [5]. Deploying a solar-thermal hybrid system provides numerous advantages:

- Energy conservation: Decreases electricity usage, alleviating pressure on power infrastructure.
- Environmental impacts: Reduces emissions linked to traditional cooling systems.
- Resource efficiency: Harnesses sustainable energy sources, diminishing dependence on non-renewable fossil resources.

Implementing solar-thermal technology in the air conditioning system in Muscat is a practical approach to saving energy and reducing the negative environmental effects caused by high cooling requirements. This strategy is in line with worldwide initiatives promoting sustainable energy practices and tackles the specific issues of energy use in fast growing urban regions [6]. The system's performance is evaluated by analysing its operational viewpoint and commercial applications.

2. Background

Muscat endures extended periods of elevated temperatures year-round, leading to a significant increase in the need for electricity to power cooling systems. The use of conventional air conditioning systems worsens energy usage and adds to environmental consequences, such as heightened carbon emissions [7]. It is crucial to implement sustainable cooling solutions, especially in residential buildings, to address these difficulties and encourage energy conservation.

2.1. Hybrid solar-thermal air conditioning system for Muscat

The solar-thermal hybrid air conditioning system combines solar thermal technology with traditional air conditioning systems to enhance cooling efficiency and decrease reliance on grid electricity [8]. This technology provides numerous benefits in Muscat's residential buildings:

Energy conservation is achieved by utilising solar energy for cooling, which reduces the need for traditional electricity. This helps to relieve pressure on the power infrastructure and decreases operational expenses for households.

The utilisation of renewable solar energy reduces carbon emissions linked to cooling operations, so supporting Muscat's sustainability objectives.

The system is specifically engineered to endure the climatic conditions of Muscat, guaranteeing dependable and effective operation even in extreme temperatures.

2.2. Application in residential buildings

To effectively deploy the solar-thermal hybrid AC system in residential buildings in Muscat, it is essential to evaluate the following factors [9]:

Roof space utilisation: Solar collectors can be placed on rooftops to maximise access to sunlight and enhance energy production.

System integration: The hybrid system must smoothly and effectively combine with the current air conditioning infrastructure, reducing the need for extensive modifications and minimising any inconvenience to inhabitants.

User education and engagement: It is essential to educate inhabitants about the advantages and functioning of the hybrid system to ensure its effective adoption and long-term sustainability.

3. Methodology

The approach employed in this study strictly follows established research protocols as mentioned in the study of Li et al. [10]. The primary objective is to design and refine a solar-thermal hybrid AC system that is specifically tailored for implementation in Muscat. The research process is outlined below:

a) Aggregation of meteorological data

Goal: Collect crucial meteorological information to guide the development of the system.

Data pertaining to the weather conditions in Muscat was gathered. A meteorological year was created by analysing solar radiation parameters on an hourly, monthly, and annual basis.

b) Calculation of cooling load

Goal: Calculate the necessary capacity of the cooling system.

Procedure: The calculation of the cooling load was performed to determine the necessary amount of cooling, which is crucial for accurately determining the system size.

c) System design and dimensioning

Goal: Develop and determine the specifications of the various components of the AC system.

The size and specifications for the system components were derived based on the collected meteorological data and established design criteria.

d) System optimization

Objective: Improve system efficiency to reduce energy expenses.

Methodology: The suggested system was enhanced to achieve maximum energy efficiency by utilising simulations to fine-tune component settings and system configurations for optimal performance.

e) Acquisition and construction

Objective: Obtain materials and build the experimental prototype.

Procedure: After optimising the system, the required components were acquired. Subsequently, the system was constructed and deployed to undergo testing.

f) System testing and life cycle assessment

Objective: Assess the performance and economic feasibility of the system.

Procedure: The assembled system underwent thorough testing. Life cycle costs

were determined by evaluating the system's price competitiveness and thermal efficiency for residential applications.

g)   Recommendations and analysis

Goal: Examine findings and suggest improvements.

Analysis: The data were examined to pinpoint areas where technological advancements and efficiency enhancements may be made.

Figure 1 illustrates the complete setup of the proposed hybrid solar-thermal air conditioning system, highlighting the integration of solar collectors with conventional cooling components [11]. Recommendations were made to enhance both the economic and technical performance of the system. Additionally, strategies for advancing research and development in solar cooling technologies were explored.
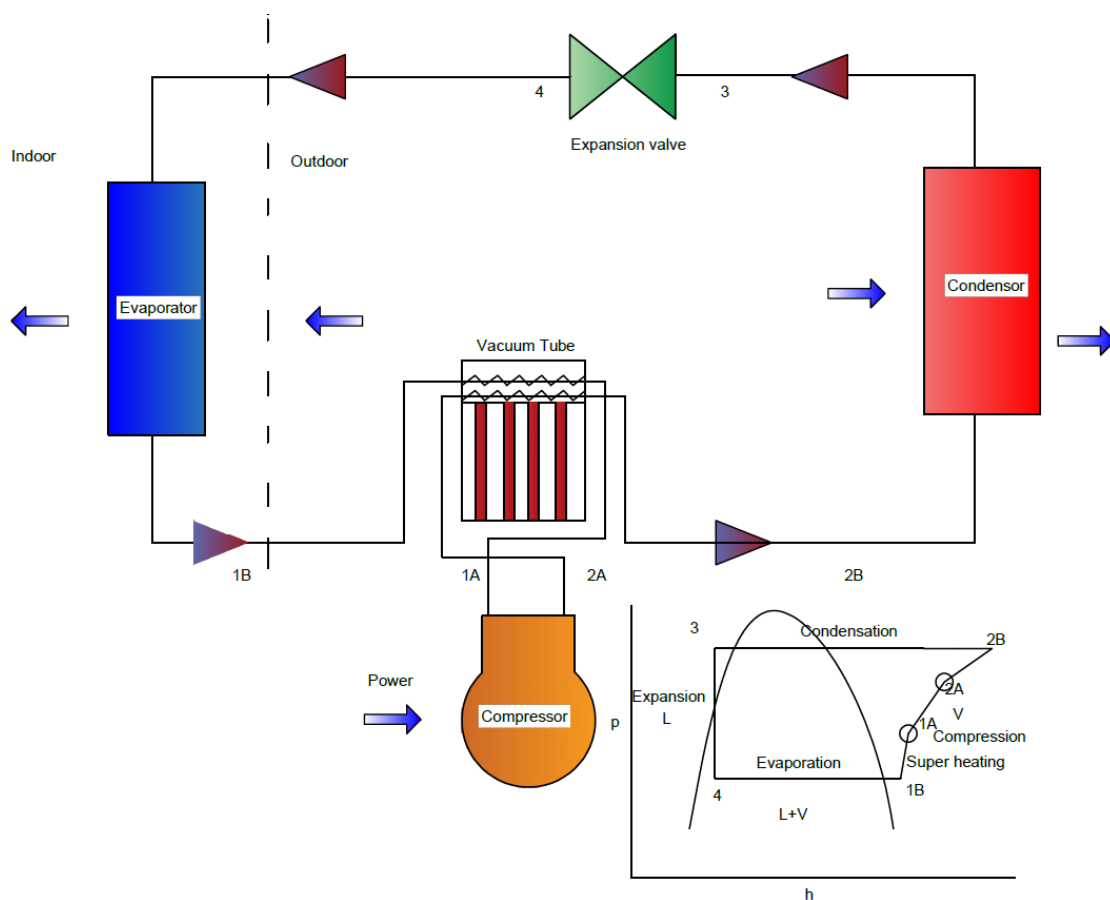
Figure 1. Proposed schematic diagram for hybrid solar-thermal air conditioner.

4. System design and description

The suggested system incorporates a direct current (DC) air conditioner with a vacuum tube solar collector, as depicted in **Figure 1**. The objective of this system is to achieve the same level of efficiency as conventional AC systems by harnessing renewable energy sources. Every element within the system is assessed separately to guarantee the best possible performance and compatibility [12]. The system is engineered to function reliably in different circumstances, aiming to achieve cooling efficiency that is on par with traditional air conditioning equipment.

## 4.1. Calculation of refrigeration load

Refrigeration load is the quantity of thermal energy that needs to be removed from a given area to reach and sustain a desired temperature. Thermal energy naturally transfers from regions with higher temperatures to regions with lower temperatures. In the realm of air conditioning, this process entails the movement of heat from the interior of a structure to the external surroundings [13].

The refrigeration load entails determining the rate at which thermal energy needs to be extracted from an indoor space. Thermal transfer occurs through walls, windows, and doors as a result of variations in temperature between the inside and outside environments [14]. The cooling demands of a location are affected by variables such as the size of the area and the composition of the building components. Furthermore, the presence of humans in the area results in the generation of heat due to metabolic processes. The metabolic heat output fluctuates considerably depending on the specific activities performed in the room, such as sleeping or dancing. In addition, electronic gadgets, and other appliances, such as printers and laptops, produce extra heat that needs to be considered when calculating the overall cooling requirement.

By precisely evaluating these elements, the system can be customised to effectively extract the necessary quantity of heat from the indoor environment, ensuring comfort while maximising energy efficiency.

4.2. The air conditioning system

Both building and vehicle air conditioning systems rely on five crucial components: the compressor, refrigerant, expansion device, evaporator, and condenser [15]. Each component is detailed in depth below, accompanied by diagrams that demonstrate their roles within the system. **Figure 2** depicts the compressor, which plays a vital role as the central component of the AC system, responsible for circulating refrigerant throughout the entire system.
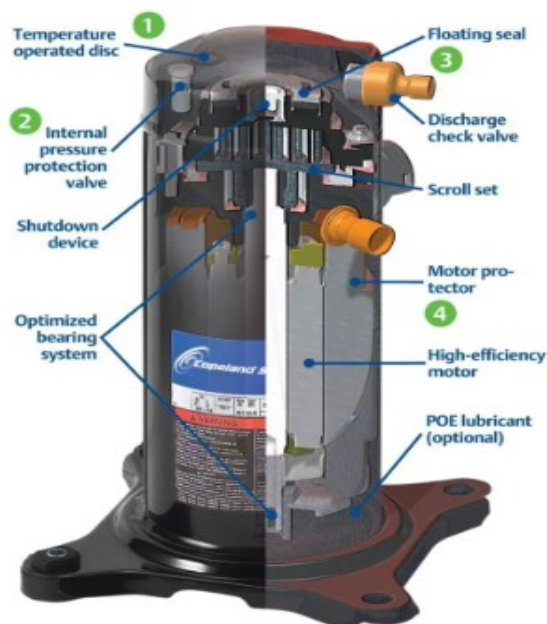
Figure 2. Compressor in air conditioning system.

The process involves compressing the refrigerant vapour, which results in an increase in both its pressure and temperature. This allows for easier circulation of the refrigerant throughout the system. The compressor is usually operated by electricity and plays a crucial role in sustaining the refrigeration process. A refrigerant is a chemical substance that functions as a coolant by collecting heat from the surrounding environment and circulating within the circuits of an air conditioning system [16]. The expansion device is located between the condenser and evaporator and is responsible for controlling the flow of refrigerant. It regulates the conversion of the refrigerant from a high-pressure (HP) liquid to a low-pressure (LP) liquid, which initiates the cooling process in the evaporator [17].

Figure 3 depicts the expansion device employed in an AC system. During the process of refrigerant circulation, the evaporator uses the refrigerant in its liquid condition to absorb heat from the cooling space and transfer it into the system [18].

Figure 3. Expansion device in air conditioning system.

The evaporator, situated in the indoor unit of the air conditioning system, has a crucial function in regulating the indoor air, as depicted in **Figure 4**. The process involves the absorption of heat from the indoor air into the liquid refrigerant, which leads to the evaporation of the refrigerant and efficiently cools the surrounding space [19].

Figure 4. Evaporator in air conditioning system.

The condenser, located adjacent to the compressor in the outside unit (as shown in **Figure 5**), is responsible for releasing the absorbed heat to the surrounding environment. The function of this process is to lower the temperature and pressure of the vapour refrigerant produced by the compressor, causing it to condense into a liquid state again [20].

Figure 5. Condenser in air conditioning system.

The combination of these components creates a seamless cycle that is crucial for the air conditioning system to effectively extract heat from the inside of a building or vehicle and expel it outside, resulting in efficient cooling of the indoor area [21].

4.3. Vacuum tube collector (VTC) system

The VTC system utilises cutting-edge solar technology, incorporating a sequence of evacuated tubes engineered to optimise the absorption and conversion of solar radiation into amounts of heat energy. These systems are mostly used in active solar heating applications, specifically for water heating in residential and commercial settings.

Usually installed on rooftops, these collectors are designed to endure various weather conditions, guaranteeing robustness and longevity. Their design and construction are vital for uninterrupted operation under different climatic conditions. The vacuum tube collector system (**Figure 6**) consists of individual tubes made of durable, airtight glass that enclose an inner metal tube called the absorber tube. This configuration reduces thermal loss by creating a vacuum between the two tubes, hence improving the efficiency of the device in capturing solar radiation.
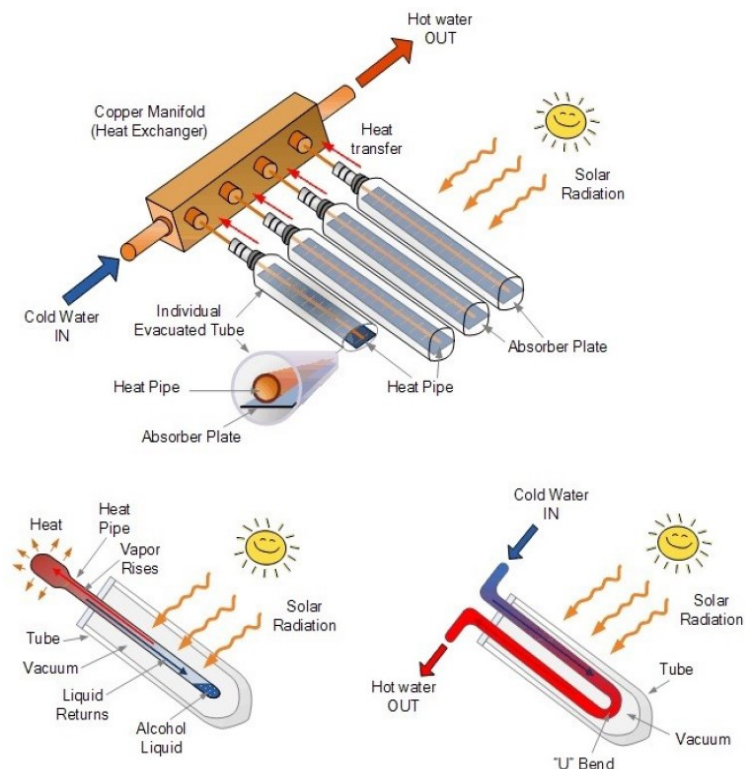
Figure 6. Vacuum tube collector solar system.

The heat pipe, a crucial element, efficiently conducts the absorbed heat upwards into the inner metal tube. The heat pipe functions within defined pressure parameters, as specified in references [22], generating a dynamic setting in which the lower end of the pipe reaches the boiling point while the higher end undergoes condensation. This mechanism leads to an effective heat transfer driven by a phase transition from the "hot" end to the "cold" end of the pipe.

The evacuated tube design enables efficient solar energy collection while minimising heat loss to the surroundings. At the high temperature region, the liquid contained within the heat pipe undergoes boiling, effectively absorbing thermal energy from the sun. The vapour produced moves upwards to the colder part, where it undergoes condensation, transferring the heat to the water or another heated fluid. The process of boiling and condensing in the vacuum tube system effectively transfers thermal energy, making it very efficient for solar thermal applications. Vacuum tube collector systems utilise advanced technology to harness the sun's energy, making them a dependable and sustainable method for heating water. These systems make a substantial contribution to energy conservation initiatives [23].

5. Functioning of the system

The presented technology utilises solar energy in conjunction with conventional vapor-compression refrigeration methods to operate the air conditioning system. This hybrid strategy not only improves energy efficiency but also harnesses renewable energy sources to minimise the overall environmental footprint.

The system initiates with the solar unloading unit, which efficiently catches solar radiation and turns it into thermal energy. Water serves as the thermal transfer medium, enabling this conversion. The hot water is stored in a thermal reservoir, guaranteeing a continuous supply of thermal energy for the system's functioning.

The central component of the system is a traditional direct expansion, mechanical, vapor-compression refrigeration system. Its main purpose is to provide air cooling by extracting heat from internal areas and releasing it outside [24].

Evaporation begins at the evaporator coil, which is situated inside the cooling area. In this process, a frigid, low-pressure refrigerant assimilates thermal energy and undergoes vaporisation, transitioning from a liquid to a gaseous phase. This process of phase transition extracts thermal energy from the indoor air, resulting in its efficient cooling.

Compression: The gaseous refrigerant is then sent to the compressor, where it is pressurised to a high level, causing its temperature to increase dramatically.

Condensation: The hot, high-pressure gas is sent to the condenser coil, where it dissipates its heat to the surrounding air. As the refrigerant releases thermal energy, it undergoes condensation and returns to a liquid state.

Expansion: The heated liquid flows via an expansion device, where its temperature and pressure are decreased, to be ready to re-enter the evaporator and resume the cycle.

The schematic depicted in **Figure 7** showcases the cyclical operation of the refrigeration system, emphasising the integration of hybrid solar thermal energy to optimise the efficiency of the cooling process. By using solar energy to aid in heating

the refrigerant, the technology decreases the energy requirement of the compressor, therefore saving electricity and reducing operational expenses. This integration enhances system efficiency and promotes sustainable energy practices by decreasing reliance on non-renewable energy sources.
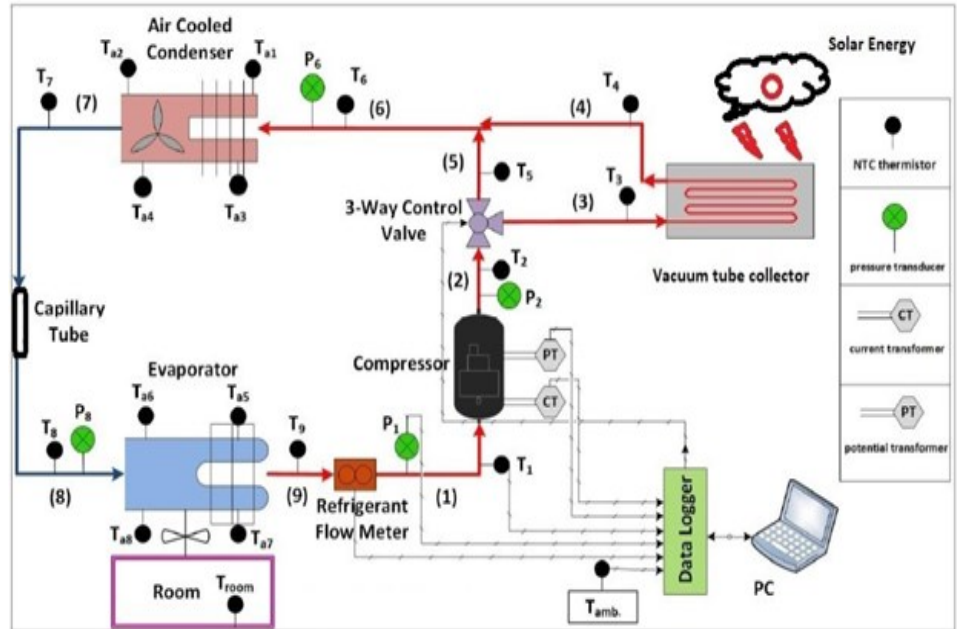

Figure 7. Control diagram of solar thermal air conditioning system.

6. Conclusion

To summarise, the introduction of a solar-thermal hybrid air conditioning system offers a hopeful resolution to tackle the issue of energy saving in residential buildings in Muscat. This system utilises renewable solar energy as a means of cooling, providing a sustainable alternative to traditional cooling methods. This not only helps to save the environment but also enhances energy efficiency.

The main goal of this study is to improve the effectiveness of split AC systems and optimise energy conservation in areas with elevated ambient temperatures.

One of the main tactics is to combine a solar collector vacuum tube with the air conditioning system to maximise performance and enhance energy efficiency.

Performing empirical and quantitative comparisons of standard and split air conditioning systems.

This study aims to improve the thermal efficiency and decrease power usage in Muscat by using a thermal-solar air conditioning system.

References

1. Ali ARI, Salam B. A review on nanofluid: preparation, stability, thermophysical properties, heat transfer characteristics and application. SN Applied Sciences. 2020; 2(10). doi: 10.1007/s42452-020-03427-1

2. Bu X, Wang L, Li H. Performance analysis and working fluid selection for geothermal energy-powered organic Rankine-vapor compression air conditioning. Geothermal Energy. 2013; 1(1). doi: 10.1186/2195-9706-1-2

3. Diaconu BM, Varga S, Oliveira AC. Numerical simulation of a solar-assisted ejector air conditioning system with cold storage. Energy. 2011; 36(2): 1280-1291. doi: 10.1016/j.energy.2010.11.015

4. Faghih S, Pourshaghaghy A. Selecting working fluids in organic Rankine cycle (ORC) for waste heat applications and optimal cycle parameters for different hot source temperatures. Journal of Thermal Analysis and Calorimetry. 2022; 147(23): 13737-13755. doi: 10.1007/s10973-022-11502-5

5. Fedele L, Lombardo G, Greselin I, et al. Thermophysical Properties of Low GWP Refrigerants: An Update. International Journal of Thermophysics. 2023; 44(5). doi: 10.1007/s10765-023-03191-5

6. Gao P, Li S, Bu X, et al. Direct conversion of CO_2 into liquid fuels with high selectivity over a bifunctional catalyst. Nature Chemistry. 2017; 9(10): 1019-1024. doi: 10.1038/nchem.2794

7. Hu B, Bu X, Ma W. Thermodynamic Analysis of a Rankine Cycle Powered Vapor Compression Ice Maker Using Solar Energy. The Scientific World Journal. 2014; 2014: 1-6. doi: 10.1155/2014/742606

8. Kaggwa A, Carson JK. Developments and future insights of using nanofluids for heat transfer enhancements in thermal systems: a review of recent literature. International Nano Letters. 2019; 9(4): 277-288. doi: 10.1007/s40089-019-00281-x

9. Lei B, Zhang C, Zhang Y, et al. A Theoretical Criterion for Evaluating the Thermodynamic Effectiveness of Regenerators in Organic Rankine Cycle Systems. Journal of Thermal Science. 2021; 30(6): 2027-2036. doi: 10.1007/s11630-021-1521-5

10. Li D, Zhang S, Wang G. Selection of organic Rankine cycle working fluids in the low-temperature waste heat utilization. Journal of Hydrodynamics. 2015; 27: 458-464. doi: 10.1016/S1001-6058(15)60504-2

11. Li JF, Guo H, Lei B, et al. Thermodynamic Performance Analysis on Various Configurations of Organic Rankine Cycle Systems. In: Okada H, Atluri S (editors). Computational and Experimental Simulations in Engineering. ICCES 2019. Mechanisms and Machine Science. Springer, Cham; 2020.

12. Mekhilef S, Safari A, Mustaffa WES, et al. Solar energy in Malaysia: Current state and prospects. Renewable and Sustainable Energy Reviews. 2012; 16(1): 386-396. doi: 10.1016/j.rser.2011.08.003

13. Okonkwo EC, Wole-Osho I, Almanassra IW, et al. An updated review of nanofluids in various heat transfer devices. Journal of Thermal Analysis and Calorimetry. 2020; 145(6): 2817-2872. doi: 10.1007/s10973-020-09760-2

14. Oyedepo SO, Fakeye AB. Electric power conversion of exhaust waste heat recovery from gas turbine power plant using organic Rankine cycle. International Journal of Energy and Water Resources. 2020; 4(2): 139-150. doi: 10.1007/s42108-019-00055-3

15. Qin Y, Li N, Zhang H, et al. Energy and exergy analysis of a modified three-stage auto-cascade refrigeration cycle using low-GWP refrigerants for sustainable development. J Therm Anal Calorim. 2023; 148: 1149-1162. doi: 10.1007/s10973-022-11721

16. Ravi G, Adhimoulame K. Thermodynamics studies on VCRS using refrigerant blends of R290, R600A, and R1234ZE. Multiscale and Multidisciplinary Modeling, Experiments and Design. Published online May 4, 2024. doi: 10.1007/s41939-024-00442-2

17. Rostamzadeh H, Ghaebi H. Parametric study and working fluid selection of modified combined power and refrigeration cycles (MCPRCs) using low-temperature heat sources. Journal of the Brazilian Society of Mechanical Sciences and Engineering. 2018; 40(1). doi: 10.1007/s40430-018-0971-5

18. Roy R, Mandal BK. Energy, exergy and economic optimization of a two-stage refrigeration system using low-GWP alternative refrigerants for high-temperature lift applications. Journal of the Brazilian Society of Mechanical Sciences and Engineering. 2023; 45(8). doi: 10.1007/s40430-023-04320-9

19. Singh KK, Kumar R. Energy, Exergy, Environmental and Economic Analyses of Natural Refrigerants for Cascade Refrigeration. Arabian Journal for Science and Engineering. 2022; 47(12): 15797-15821. doi: 10.1007/s13369-022-06804-7

20. Singh KK, Kumar R, Gupta A. Multi-objective Optimization of Thermodynamic and Economic Performances of Natural Refrigerants for Cascade Refrigeration. Arab J Sci Eng. 2021; 46: 12235-12252. doi: 10.1007/s13369-021-05924

21. Toujani N, Bouaziz N, Kairouani L. Energetic Analysis and Working Fluids Selection for a New Power and Refrigeration

Combined Ecological System. Journal of Thermal Science. 2022; 31(6): 2032-2050. doi: 10.1007/s11630-022-1645-2

22. Wu D, Peng C, Yin C, et al. Review of System Integration and Control of Proton Exchange Membrane Fuel Cells. Electrochemical Energy Reviews. 2020; 3(3): 466-505. doi: 10.1007/s41918-020-00068-1

23. Zhang N, Dai Y. Thermophysical Properties and Applications in Refrigeration System of the Low-GWP Refrigerant R1243zf and Its Blends. Int J Thermophys. 2021; 42: 152. doi: 10.1007/s10765-021-02902-0

24. Vankov YV, Al-Okbi AK, Hasanen MH. Solar hybrid air conditioning system to use in Iraq to save energy. E3S Web of Conferences. 2019; 124: 01024. doi: 10.1051/e3sconf/201912401024